THE STUDY OF NOVEL LIGHT DELIVERY

SYSTEM FOR HEAT ASSISTED MAGNETIC

RECORDING

SAJID HUSSAIN

M.Sc., Electrical Engineering, NUS, Singapore
B.Sc., University of Engineering & Technology Lahore, Pakistan

A THESIS SUBMITTED FOR THE DEGREE OF DOCTOR OF
PHILOSOPHY

DEPARTMENT OF ELECTRICAL AND

COMPUTER ENGINEERING

NATONAL UNIVERSITY OF SINGAPORE

JANUARY 2015

DECLARATION

I hereby declare that the thesis is my original work and it has been written by me in its entirety. I have duly acknowledged all the sources of information which have been used in the thesis.

This thesis has also not been submitted for any degree in any university previously.

Sajid Hussain

2015

Acknowledgements

I would like to express my deepest appreciation to my supervisor Dr. Aaron J. Danner, who has the attitude and element of a genius. He continuously conveyed an enthusiasm in regard to my experimental work. Without his guidance and persistent help this dissertation would not have been possible.

I would like to thank my co-supervisors, Prof. Charanjit Singh Bhatia and Dr. Hyunsoo Yang, who gave me great confidence by showing strong trust and faith in me. They have always encouraged me to work harder and smarter and provided me full freedom to explore my research work while focusing on the final goal. I am grateful for them for allowing me to access and use the most advanced fabrication and characterization techniques available in NUS, without which it would not have been possible to complete my experimental and characterization work for this thesis.

I would like to express my gratitude to all the past and present members in the Spin and Energy Laboratory (SEL) of the National University of Singapore for their appreciated help and friendship. Special thanks go to Dr. Deng Jun and Mr. Siew Shawn Yohanes for their help in wafer dicing, thesis editing, FIB, metal deposition and programming. I would also like to thank them for sacrificing their valuable time to accompany me in the cleanroom whenever required. It has been a real joy working with them, chatting with them and having meals together.

I would like to thank all my friends in Singapore, especially Mr. and Mrs. Ehsan Younis, Muhammad Hafeez, Fraz Ahmed, Yasir Cheema and Wakil Shehzad for their guidance, help and encouragement. A special thanks to my

best friend Ms. Nurjiha, for always being with me during all the ups and downs. I owe these people a lot for everything they did for me during all these years.

Lastly, I would like to thank my great parents and brothers who always gave me their support, no matter what. I would like to take this opportunity to tell you all that I love you all so much and I will always be in debt to everything you have done for me in my life.

Abstract

The demand for magnetic storage density increases tremendously every year. This drives the development of new techniques to increase the storage capacity in hard drives. This development is impeded by the thermal limit of magnetic media, also known as the superparamagnetic limit. This effect causes small bits to change their magnetic orientation randomly, leading to data loss. High coercivity magnetic media are required in order to overcome the superparamagnetic effect. However, this requires a higher write head magnetic field to obtain magnetic reversal of the magnetic bits.

Heat assisted magnetic recording (HAMR) is a next generation technology proposed for achieving magnetic storage densities beyond 1 Tb/in^2. The principle of HAMR is similar to the derivative of magneto-optical recording proposed by Katayama and Saga separately in 1999 [1, 2] and was first demonstrated by Seagate in 2006 [3]. HAMR makes writing high anisotropy media possible, facilitating the use of smaller thermally stable grains. In a typical HAMR process, the temperature of a high anisotropy medium is raised above its Curie temperature, lowering its coercivity to a value within the writable range of a magnetic field supplied by a conventional write head.

However, the commercialization of HAMR faces substantial technical challenges that must be resolved before widespread adoption of the technology can commence. Foremost of these challenges is the development of a precise method of delivering light to a very small, sub-wavelength bit area with sufficient power to heat a high coercivity magnetic medium above its Curie temperature. Complex fabrication processes, low power transfer efficiency and

high heat dissipation are the biggest problems faced in current HAMR light delivery systems.

In this thesis a new light delivery system consisting of the nano-aperture vertical-cavity surface emitting laser (VCSEL) as a potential candidate for an alternative light delivery system in HAMR is proposed. The transmission and focusing characteristics of differently shaped nano-apertures, including the conventional square shape and unconventional shapes such as the C-shape, H-shape, T-shape and L-shape are studied via simulation, in order to find the most suitable shape to be used as a near field transducer for HAMR applications. The C-shaped nano-aperture shows the best transmission and focusing characteristics and is the strongest candidate as a near field transducer (NFT) for HAMR. The resonant wavelength of C-shaped nano-apertures is strongly affected by the storage media, placed in the near-field of the nano-aperture.

The power density requirement has been found with successful HAMR demonstrations with control C-shaped nano-aperture near-field transducers fabricated on glass substrates. The C-apertures have shown localized focusing properties compared to square aperture which have low power transmission and cannot be used for successful HAMR demonstration, with the same incident power density as the C-apertures.

850-nm VCSELs with large arrays of differently shaped nano-apertures in the Au layer on the top facets were fabricated and statistical methods were used to obtain reliable indicators of performance of each aperture. The power density available from C-shaped nano-aperture VCSELs is comparable to the power

density required for HAMR, which makes these VCSELs a strong alternative light delivery system for HAMR, with additional advantages of easy fabrication, low cost and less thermal losses inside the system.

Table of Contents

Chapter 1

Chapter 2

Chapter 3

Chapter 4

Chapter 5

Chapter 6

Chapter 7

List of Figures

List of Tables

List of Symbols and Abbreviations

$\overrightarrow{H_d}$	**Demagnetization field**
$\left\lvert E^2 \right\rvert$	**Local field intensity.**
$\vec{B}$	**Magnetic flux density**
E_{ex}	**Exchange interaction**
$\vec{H}$	**Magnetic field strength**
$\vec{j}$	**Total angular momentum**
$\vec{j}\left(\vec{r}\right)$	**Current density at a location** r'
J_{ij}	**Exchange constant**
$\vec{M}$	**Magnetization**
S^*	**Coercivity squareness**
I_{th}	**Threshold current**
w_p	**Electron plasma frequency**
μ_0	**Permeability of the magnetic material**
$\mathring{A}$	**Angstroms**
ABC	**Absorbing boundary conditions**
AFC	**Anti-ferromagnetically coupled**
AFM	**Atomic force microscopy**
BPM	**Bit patterned magnetic media**
CW	**Continuous-wave**
CCD	**Charged-coupled device**

cm	**Centimeters**
D	**Dose (charge per unit area)**
DBR	**Distributed Bragg Reflector**
DUT	**Device under test**
EAMR	**Energy assisted magnetic recording**
EBL	**Electron beam lithography**
ECC	**Exchange coupled composite media**
FDTD	**Finite Difference Time Domain**
FePt	**Iron platinum**
FE-SEM	**Field emission-scanning electron microscopy**
FM	**Ferromagnetic**
FWHM	**Full width at half maximum**
Gb	**Gigabyte**
h	**Planck's constant**
H_c	**Coercive field**
HAMR	**Heat assisted magnetic recording**
HCP	**Close-packed structure**
HDD	**Hard disk drive**
HSQ	**Hydrogen silsesquioxane**
in	**Inch**
I.E.	**Intensity enhancement**
IPA	**Isopropyl alcohol**
Kb	**Kilobyte**
k_B	**Boltzmann constant**

kOe	**Kilo-Oersteds**
K_u	**Magnetocrystalline anisotropy constant**
L	**Orbital angular momentum**
LCP	**Left handed circular polarization**
LED	**Light emitting diode**
LMR	**Longitudinal magnetic recording**
LP	**Linear polarization**
m	**Magnetic moment**
MAMR	**Microwave assisted magnetic recording**
Mb	**Megabyte**
MFM	**Magnetic force microscopy**
MIBK	**Methyl isobutyl ketone**
MOKE	**Magneto-optical Kerr effect microscopy**
M_r	**Remanent magnetization**
M_s	**Saturation magnetization**
mW	**Milliwatts**
N	**Demagnetization tensor**
NA	**Numerical aperture**
NFT	**Near field transducer**
NIL	**Nanoimprint lithography**
nm	**Nanometers**
NP	**Nano-particle**
Oe	**Oersted**
OC	**Overcoat**
PMMA	**Polymethyl methacrylate**

PML	Perfectly matched layer
PMR	Perpendicular magnetic recording
PSTM	Photon Scanning Tunneling Microscope
PSIM	Planar solid immersion mirror
QWs	Quantum wells
RAMAC	Random access method of accounting
RCP	Right handed circular polarization
S	Spin angular momentum
COE	Center for optoelectronics
SEL	Spin and energy lab
SEM	Scanning electron microscopy
SIL	Solid immersion lens
SIM	Solid immersion mirror
SNR	Signal to noise ratio
SPs	Surface Plasmons
SUL	Soft underlayer
T	Temperature in Kelvin
Tb	Terabyte
T_C	Curie temperature
UHV	Ultra-high vacuum
V	Volume
VCSEL	Vertical Cavity Surface Emitting Laser
VSM	Vibrating sample magnetometer
μm	Micrometer
μ_B	Bohr magnetrons

μW	**Microwatt**
v	**Electron velocity**
k	**Wave vector**
p	**Momentum of each photon**
η	**Quantum efficiency**

List of Publications, Patents and Conferences

Publications in Peer-reviewed Journals

1. **<u>S. Hussain</u>**, C. S. Bhatia, H. Yang and A. J. Danner, "Effect of FePt on resonant behavior of a near field transducer for high areal density Heat Assisted Magnetic Recording (HAMR)", App. Phys. Lett., **104**, 111107, (2014)

Conferences

1. S. Hussain, S. Kundu, C.S. Bhatia, H. Yang and A.J. Danner, Heat-assisted magnetic recording (HAMR) demonstration using C-shaped nano-apertures, Photonics West, Feb 7-12, San Francisco, USA (2015)

2. S. Hussain, C. S. Bhatia, H. Yang and A. J. Danner, "Characterization of nano-apertures using Vertical-Cavity Surface-Emitting lasers", The 5th International Conference on Metamaterials, Photonic Crystals and Plasmonics (META'14), May 20-23, Nanyang Technological University (NTU), Singapore (2014) (Oral)

3. S. Hussain, C. S. Bhatia, H. Yang and A. J. Danner, "Fabrication and Characterization of Nano-Aperture VCSELs for 10 Tb/in^2 Magnetic Storage Densities", Optical MEMS & Nanophotonics 2013, Aug 18-22, Kanazawa, Japan (2013) (oral)

4. S. Hussain, S. Kundu, C. S. Bhatia, H. Yang and A. J. Danner, "Heat assisted magnetic recording (HAMR) with nano-aperture VCSELs for 10 Tb/in^2 magnetic storage density", Photonics West, Feb 2-7, San Francisco, USA (2013) (Oral)

5. S. Hussain, C. S. Bhatia, H. Yang and A. J. Danner "Characterization of near field transducer for high density heat assisted magnetic recording combined with FePt recording media", Photonics Global Conference (PGC), 13-16 Dec, Singapore (2012) (Oral)

6. S. Hussain, C. S. Bhatia, H. Yang and A. J. Danner, "Characterization of Nano-aperture VCSELs with FePt recording media for Tb/in^2 density Heat Assisted Magnetic Recording", ICYRAM 2012, 1-6 July, Matrix@Biopolis, Singapore (2012) (Poster)

Chapter 1

Introduction

The hard disk drive (HDD) is the most common choice for non-volatile secondary storage of digital data in modern computer systems [4]. The ascendance of HDDs has been driven primarily by the combination of their low cost per stored bit and high areal storage density (frequently expressed in bits per square inch). This chapter discusses the background of magnetism in magnetic materials, the history of HDD technologies, limitations of these technologies and new potential technologies available to enhance magnetic storage.

1.1. Fundamentals of Magnetism

Magnets have been known since antiquity, and one of the first widespread uses of magnets was as a navigational aid in the form of a compass. In a bar magnet, the end of magnet pointing toward North is termed the north pole, and the end pointing toward South is termed its south pole. Like poles repel one another and opposite poles attract. The following discussion on the origin of magnetism and its dependence on electric charges is adapted from [5, 6].

A magnetic pole can be formed by passing a current through a coiled wire. At the atomic level, electrons are the basis of the most important magnetic dipole moment; two types of momenta are associated with electrons, as shown in Figure 1.1. Orbital angular momentum is caused by an electron's motion around an atomic nucleus and spin is an intrinsic form of angular momentum
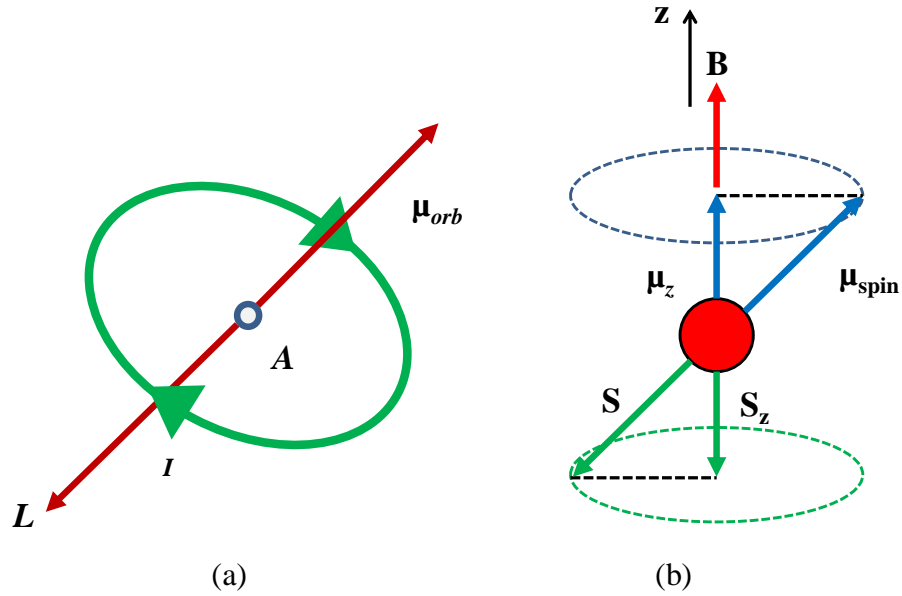
Figure 1.1: (a) A magnetic dipole produced from an orbiting electron (b) spin magnetic moment

carried by electrons and other elementary particles, composite particles (hadrons), and atomic nuclei. A magnetic moment is the overall result of orbital and spin angular momenta, due to which an atom behaves as a tiny magnet. Atomic magnetic moments are measured in units called Bohr magnetrons (μ_B).

$$\mu_o = \frac{e}{2m_e}L \qquad \text{Eq. 1.1}$$

$$\mu_{spin} = -\frac{e}{m_e}S \qquad \text{Eq. 1.2}$$

$$\mu_z = -\frac{e}{m_e}S = -\frac{e}{m_e}(m_s\hbar) = -\frac{e\hbar}{2m_e} = \beta \qquad \text{Eq. 1.3}$$

Uncompensated electron spin, instead of the orbital angular momentum, is responsible for magnetism in most materials. A free space field, B_O, inside a solenoid (Figure 1.2) depends on the current flowing in the wire, I, and the number of turns of the wire, n, is given by $B_O = \mu_O nI = \mu_O I'$.
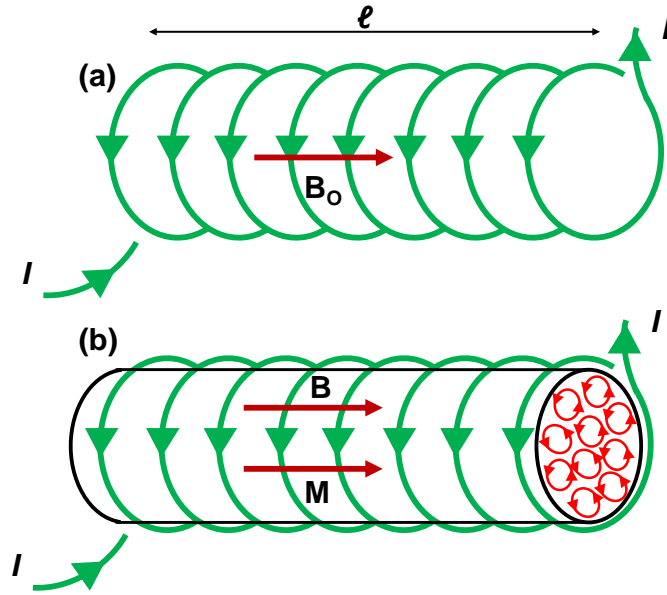
Figure 1.2: (a) A solenoid with free space as medium, the magnetic field is B_O, (b) magnetization $\vec{M}$ developed when a material medium is inserted into the solenoid

The magnetization, $\vec{M}$, within a magnetic material depends on the density of individual induced magnetic moments, $\vec{m}_I$,

$$\vec{M} = \frac{1}{V}\sum \vec{m}_I \qquad \text{Eq. 1.4}$$

This will induce a magnetic field, $\vec{B} = \vec{B_0} + \mu_O\vec{M}$ in a magnetized medium of magnetic field strength

$$\vec{H} = \frac{1}{\mu_O}\vec{B} - \vec{M} \qquad \text{Eq. 1.5}$$

where μ_O is the permeability of the magnetic material.

1.2. Types of Magnetic Materials

The orbital motion of electrons in a magnetic material is affected by an applied external magnetic field which results in a magnetic moment even if the net magnetic moment is zero in the material. There are three important types

3

of magnetic materials depending on their response to external magnetic fields. In diamagnetic materials, the direction of the induced moment is opposite to the applied external field.
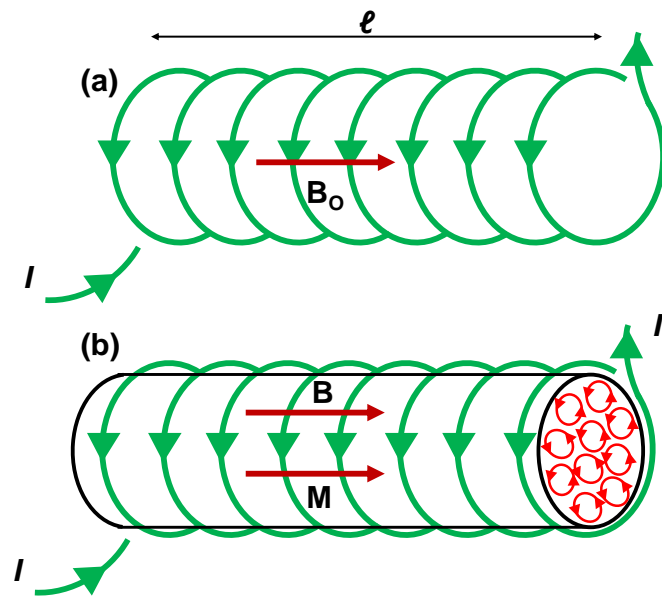
Figure 1.3: (a) A solenoid with free space as medium, the magnetic field is B_O, (b) magnetization $\vec{M}$ developed when a material medium is inserted into the solenoid

In paramagnetic materials, a small magnetic moment is induced in the same direction of the external field. Such material feels an attractive force when put between the poles of an electromagnet. The induced magnetization goes back to zero due to thermal effects after the removal of the applied field.

The last type of materials invloves significant exchange interaction between magnetic atoms which can favor both parallel and antiparallel alignment of moments depending upon the material. If the alignment due to interaction is parallel, the materials are called ferromagnets and the ordering is called ferromagnetic (FM). On the other hand; if the alignment is antiparallel, the materials are called antiferromagnets and the ordering is called antiferromagnetic (AFM). In ferromagnets, the magnetic moments remain

4

aligned even after the removal of the magnetic field, which results in a strong internal magnetic field. A stray field known as demagnetization field ($\overrightarrow{H_d}$) is produced inside a ferromagnetic material because of the magnetization ($\overrightarrow{M}$) inside a ferromagnet. The demagnetization field is given as:

$$\overrightarrow{H_d} = -N\overrightarrow{H_d} \hspace{3cm} \text{Eq. 1.6}$$

where N is known as the demagnetization tensor and depends on the shape of the ferromagnet. The magnetic moments inside an individual domain are always aligned in a preferred direction. This property is called magnetic anisotropy and it depends on the shape, crystal structure and the stress applied to a magnetic material. In materials which are not ferromagnets, the induced magnetization and the external field have a linear relationship.

Ferrimagnets behave like ferromagnets but with a smaller effective moment. Both ferromagnets and ferrimagnets show a hysteresis. In general, hysteresis is observed due to the presence of energy barriers in a magnetic system during magnetization reversal. An example of a hysteresis loop for a ferromagnetic material is shown in Figure 1.3. The material has zero net magnetization before applying an external magnetic field. The magnetization increases as the external field is increased from zero and reaches a saturation point. This relationship may not be linear. The magnetization ultimately reached at saturation with a high applied field, called the saturation magnetization (M_s). When the field is reduced to zero, the magnetization does not follow the field anymore and does not go to zero. The material instead has a residual magnetization even at zero external field, known as remnant magnetization (M_r). The ratio M_r/M_s is called squareness (S) which ranges from 0 to 1.
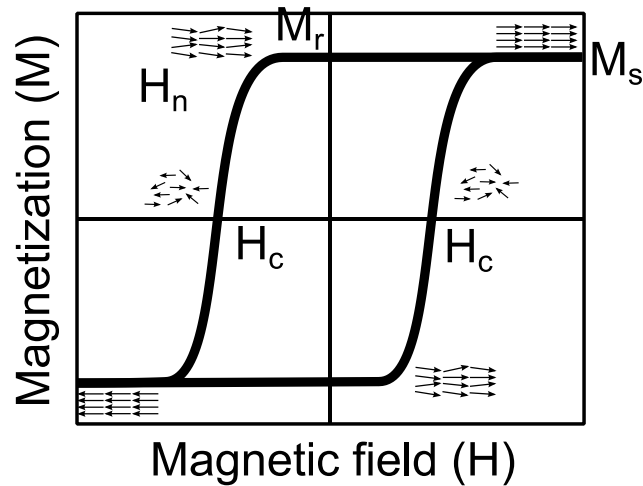
Figure 1.4: An example of a hysteresis loop of a ferromagnetic material

An S=1 value would mean that all the magnetic domains retain magnetization even after removal of the external field. When the field is changed to negative, the magnetization reduces to zero at a certain field strength, called coercive field (H_c). The value of H_c is an important parameter and depends on the magnetic material.

Based on the hysteresis loop, ferromagnets can be categorized as hard or soft materials, depending on their magnetic properties. The soft materials are those materials which can be saturated or magnetically reversed with weaker fields, usually less than 100 Oe. These materials have low coercivity, low remnant magnetization and their hysteresis loops occupy smaller areas. Common examples are Fe, steel and permalloy. On the other hand, the hard materials have high coercivity, usually higher than 500 Oe. Therefore, a higher magnetic field is required to magnetize or demagnetize these materials.

A magnetically ordered material loses its order when heated to a certain temperature. For ferromagnetic materials, this temperature is known as the Curie temperature (T_C). At this temperature, thermal energy dominates the

exchange coupling and destroys the ordering inside the magnetic material. The material behaves like a paramagnet above its Curie temperature.

1.3. History of Magnetic Recording

The history of magnetic recording dates back to early 1878, when Oberlin Smith tried to record sound on wire, inspired by Thomas Edison, who created the cylinder phonograph in 1877 [7]. Smith did not succeed, but he wrote an article about it which was published in Electrical World in September 1888. Valdemar Poulsen in Denmark successfully invented the first magnetic recorder called the Telegraphone, in 1898 and patented it in 1899 under his name [7]. It was made of a steel wire which could be magnetized and demagnetized continuously along its length. In 1905, the American Telegraphone Company attained the patent rights and prepared dictating machines. However, it could not compete with the wax cylinder phonographs of the rival Ediphone and Dictaphone companies because the signal in the Telegraphone was weak without amplification and the wires were unreliable; thus the company stopped manufacturing after 1924. Kurt Stille started selling an improved wire recorder with an electronic amplifier and in 1928 he contracted with Ferdinand Schuchard AG and its talented engineer Semi Begun and manufactured the first cassette magnetic recorder, the Dailygraph [7, 8].

The German engineer Fritz Pfleumer came up with a new idea in 1927. He tried coating paper tape with iron oxide. Although his recorder tore up the paper, he was able to demonstrate the potential of tape as a reusable medium. Hermann Bucher, Chairman of the Board of Directors of AEG, signed a

contract with Pfleumer to develop a recorder which became one of the greatest corporate research and development triumphs of the century. The team invented a ring-shaped magnetic head in 1933 which was able to focus a strong magnetic field on a small area of the tape without touching it; and a two layer magnetic tape and finally the Magnetophone K1 was introduced at the Berlin Radio Fair in August 1935. Meanwhile other kinds of magnetic recorders were being developed in Britain, the United States and Japan. Improvements were made to the German Magnetophone and the K7 model was introduced in 1943 with a tape speed of 30 ips (76 cm per second) which became the standard for future speeds. Magnetic recording was seen as a potential solution to the problems of data storage and speed in the computer industry which was emerging at that time [7, 8].

In 1937, Victor Atanasoff tried to use Poulsen's magnetic drum as a memory device for computers but he could not succeed due to the inability to perform magnetic pulse amplification.

A group of engineers led by William C. Morris was able to build the first successful magnetic drum and their work was reported at the Chicago National Electronics Conference in November 1947. The drum was 5 inches in diameter revolving at a speed of 3000 rpm and was able to achieve a recording density of 230 bits/in^2 with a rigid head that was mounted only 0.001 inch from the surface of the drum. IBM in 1952 started the Source Recording project in San Jose, to find a better method of recording information than the use of punched cards, drums or tape. Following an article by Jacob Rabinow, the IBM team started working on a 50 disk system with a capacity of 50,000 punched cards [7]. In June 1953, a successful test was completed with an "air

head", reading and writing digital data on the surface of a 16-inch aluminum disk sprayed with iron oxide paint. Later on, an improved model with a 50-disk array mounted in a vertical shaft was designed and built. The first demonstration of this memory system was given in February 1956 and was named as the Random Access Memory Accounting Machine, or RAMAC. It contained 50 disks, each disk 24-inches in diameter, 0.1 inch thick and separated by 0.3 inch spacers rotating at a speed of 1200 rpm and accessed by a single read/write head. It was able to store 5 Mb of data with an areal density of 2 Kb/in^2 [8, 9].

Before the discovery of thin film technology, the storage media used in hard drives were similar to those used in tape recording. They contained roughly 0.5 μm large magnetic particles of barium ferrite ($BaFe_2O_4$) and iron oxide (Fe_2O_3). Thin film technology made it possible to use thin magnetic films as storage media coated on the disk platters rotating at very high speed. These films are composed of magnetic grains coupled by exchange coupling and have high coercivity.

In order to reduce power consumption and per-byte cost of hard disks, areal density has increased more than 20 million- fold in the modern era and recent growth is 30-50% per year [10] (shown in Figure 1.4). Hard disk drives have become widely available for use in personal computers, game consoles, video recorders and other consumer products because of their portability, high storage capability, comparable access times and low cost per byte compared to other memory devices. As a result of this, hard disks are getting smaller, lighter, and faster; gigabits of memory can be bought today at a tiny fraction of the initial cost of IBM's first hard disk. The demand in magnetic storage

9
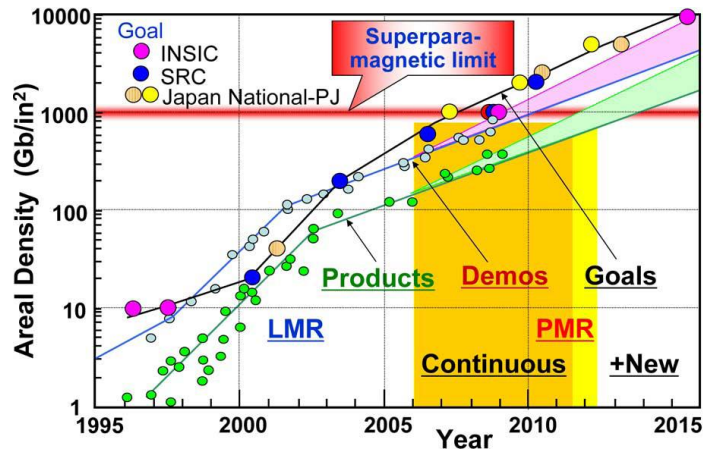
Figure 1.5: Areal density growth trend [10]. Used with permission.

density is increasing tremendously every year which requires new techniques to be developed for storage media and the write heads used in hard disk drive systems. The following sections discuss conventional magnetic recording techniques, their limits and the new alternative techniques in order to enhance magnetic recording.

1.4. Conventional Recording Schemes

1.4.1. Longitudinal Magnetic Recording (LMR)

In LMR, the information is written along the surface of the magnetic media. The media is based on the Co-based alloys and other elements like Pt. Additive elements such as Cr, Bo and Ta [11-15] are also used to improve segregation of the magnetic grains and reduce exchange coupling between the grains. The Pt atoms help in growing a hexagonal close-packed structure (hcp) which has strong anisotropy along its c-axis and helps to achieve high coercivity of the media. A Cr-based underlayer, deposited at 250 $^{\circ}$C, helps to achieve such a c-axis orientation of the Co-alloy along the substrate surface. Figure 1.5 shows the schematic diagram of longitudinal magnetic recording.

10
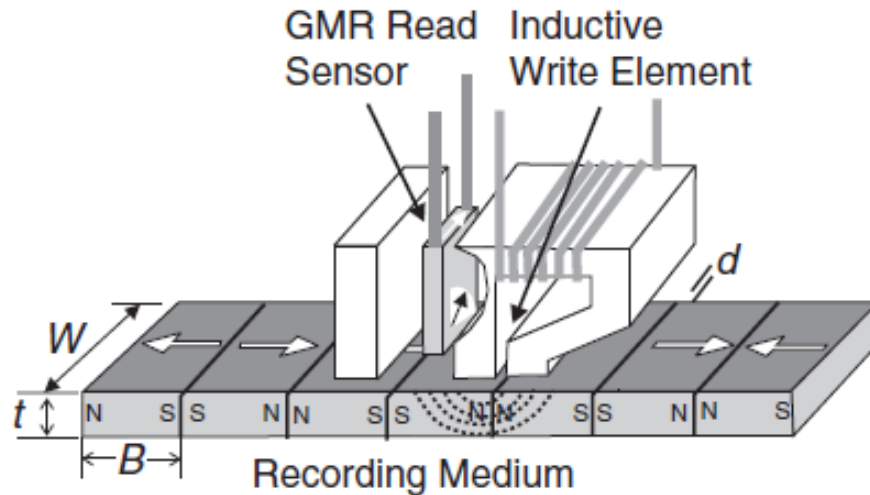
Figure 1.6: Schematic of LMR [9]. Used with permission.

An inductive write head is used to write magnetic bits in the recording media. The fringing field produced in the air-gap between the two magnetic poles, aligned directly over a magnetic bit, is used to change the magnetic orientation of the bit. A maximum areal density of 100 Gb/in^2 was achieved with LMR [16].

1.5. Superparamagnetism and Magnetic Trilemma

The signal-to-noise ratio (SNR) from an LMR media is dependent on the number of grains in a magnetic bit. To achieve sufficient SNR and maintain high recording density, grains must be small in size. However, grain size is ultimately restricted by the superparamagnetic limit [17]. Superparamagnetism is a phenomenon in which thermal energy in a grain becomes comparable or higher than its magnetic anisotropy energy which leads to thermal fluctuations in the grain which can force the magnetic bits to flip their orientation randomly, resulting in data corruption. At high temperatures, magnetization is prone to be flipped by thermal fluctuations but is prevented by an energy

11

barrier given by the product of the magneto crystalline energy and the volume of the magnetic grain. The magnetic orientation of a magnetic grain can be flipped randomly if the thermal energy product k_BT, where k_B is the Boltzmann constant and T is the absolute temperature, is comparable to or higher than the anisotropy energy product K_uV, where K_u is the magnetocrystalline anisotropy constant and V is the volume of the magnetic grain. This will eventually result in data corruption [18]. The ratio of these two products is used as a figure of merit in industry for stability; this ratio is given in Equation 1.7 [19]. Values between 40 and 60 conform to industry requirements.

$$\frac{K_uV}{k_BT} \geq 40 - 60 \qquad \text{Eq. 1.7}$$

Media SNR

SNR~10log(N)
*N is number of grains

Thermal Stability   **Writability**

$$E_B \cong K_uV. \left[1-\frac{H_d}{H_0}\right]^{-3/2} \qquad H_0 = \alpha.\frac{2.K_u}{M_S} - N_{eff}.M_S$$
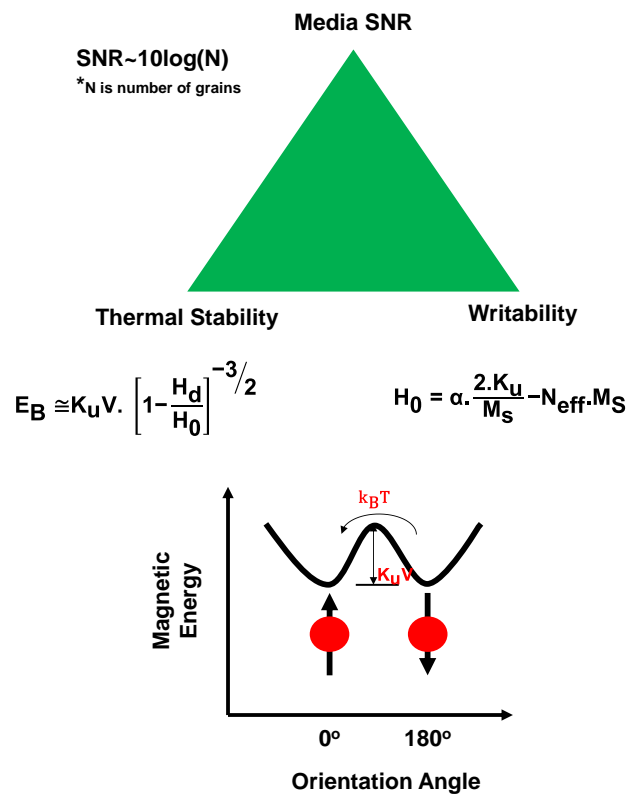
Figure 1.7: Illustration of magnetic recording trilemma

The signal-to-noise ratio (SNR) of the readback signal depends on the number of grains per bit and it is necessary to have high number of grains in a magnetic bit in order to maintain a sufficient SNR [20]. The relationship is given as:

$$SNR = 10 \log N \qquad \text{Eq. 1.8}$$

where N is the number of grains in a bit. In order to maintain the SNR value with increasing areal densities, smaller grain sizes are necessary. A smaller grain size, however, may not satisfy thermal stability requirements and therefore can be flipped randomly due to thermal fluctuations. In this case, magnetic materials with high anisotropy (K_u) are needed as alternatives to current magnetic media. High anisotropy materials have high coercivity; thus higher magnetic fields are required in order to switch a magnetic bit, which results in writability issues. The current maximum value of the available write magnetic field is ~ 2.4 T [21]. This situation is called the magnetic trilemma as shown in Figure 1.6. New technologies are being developed in order to overcome the magnetic trilemma. These technologies will be discussed in the following sections.

1.6. Advanced Recording Schemes

1.6.1. Perpendicular Magnetic Recording (PMR)

Iwasaki and Takemura [22-24], in the 1970s, introduced a number of new recording technologies including PMR which includes a recording media having perpendicular anisotropy, but it was possible only in 2005 to incorporate PMR in HDDs after extensive research efforts. Iwasaki and
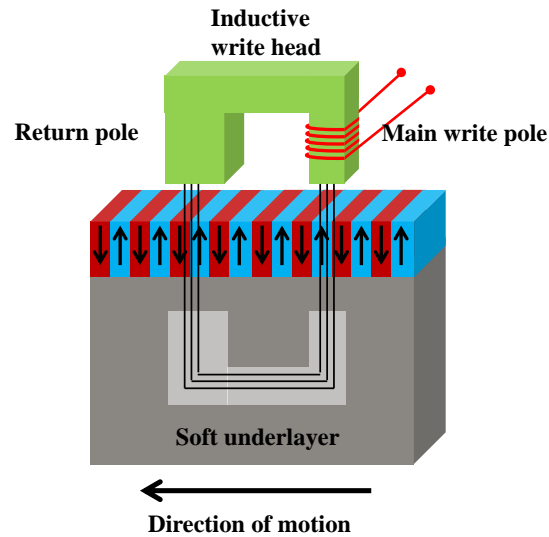
Figure 1.8: Schematic of PMR

Takemura discovered that the demagnetization field increases in LMR as the bit size decreases which affects the output voltage of the reader. PMR was introduced as a better solution to superparamagnetism in order to achieve high areal densities. PMR is shown in Figure 1.7. The main feature of this technology is the use of a soft underlayer which has high saturation magnetization and high magnetic permeability in the circumferential direction and low permeability in radial direction which supports the magnetic lines flow from the main write pole to the return pole. In PMR, the air-gap field between the head pole and the media is used to write a magnetic bit unlike the fringing field in LMR. The soft underlayer produces an image of the write head which results in high effective magnetic field compared to LMR. Hence, high magnetic anisotropy media can be used as storage media which are more stable thermally and can suppress the superparamagnetic effect in order to achieve high areal densities [20, 25].

Magnetic media which can be used in PMR include Co/Pd multilayers [26], CoCrPt alloys [27] and CoCrPt-oxide alloys [28], with CoCrPt-oxide being used currently in PMR. The oxides in CoCrPt-oxide based magnetic layers are used for grain segregation; the most commonly-used oxides are SiO_2, TiO_2 or Ta_2O_5 [29-31]. Perpendicular anisotropy in the magnetic medium is promoted by using a (002) textured hcp Ru underlayer. Amorphous materials such as CoTaZr or FeCoB are the best materials for SULs in PMR. There have been many improvements in PMR technology since its introduction in terms of magnetic layers, SUL, spacer layer and underlayers, which has made it possible to push back the onset of the superparamagnetic limit and achieve an areal density of 600 Gb/in^2 [32].

1.6.2. Exchange Coupled Composite Media (ECC)

Victora et al. [33] proposed ECC media as a new technique to solve the problem of the magnetic trilemma. ECC media is composed of two magnetic regions having different coercivities in a single grain. The upper layer has low coercivity (magnetically soft media) and the lower layer has high coercivity (magnetically hard media) with the magnetic easy axis oriented perpendicular to the surface. An intermediate layer is used in order to induce exchange coupling between these two layers. A schematic diagram of ECC media is shown in Figure 1.8. The switching is performed by applying a low magnetic field on the soft layer which exerts a torque on the hard layer and initiates magnetic reversal through exchange coupling. Hence ECC allows the use of high coercivity media without compromising writability and thermal stability problems [34]. The applied magnetic field rotates the easy axis of magnetization in the soft layer by 45° and hence the field acting on the hard
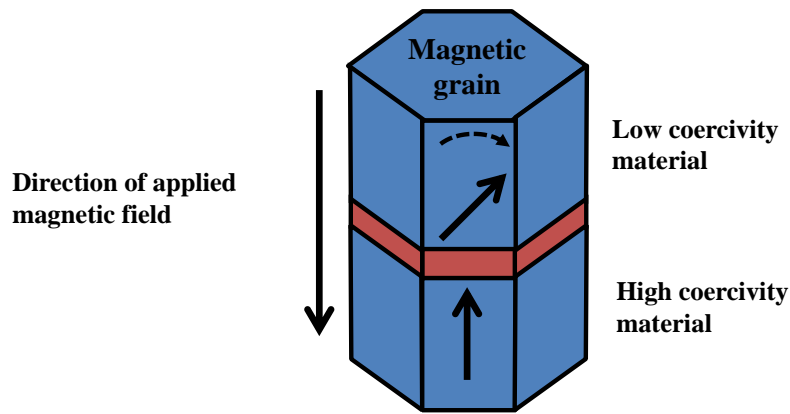
Figure 1.9: ECC media grain, with hard and soft magnetic regions

media is at 45°, which eventually results in magnetic reversal in hard media at a reduced field. The intermediate non-magnetic layer is introduced in order to control the magnitude of exchange coupling between soft and hard layers and thus to control the switching process [35]. Thus ECC has the ability to achieve areal densities beyond 1 Tb/in^2 without introducing major changes in storage media and the write/read head, compared to other techniques.

1.6.3. Bit Patterned Media (BPM)

Bit-patterned media (BPM) is another technique to delay the onset of superparamagnetism. It is a continuous media patterned in form of isolated magnetic islands. Unlike in conventional media, one magnetic island represents one isolated magnetic grain. Hence, the magnetic volume of a bit is much larger than a single grain in conventional media [36-39]. A comparison of conventional media and the BPM is shown in Figure 1.9. The SNR equation used for conventional media cannot be applied to BPM. The magnetic volume in BPM is much larger than the volume of the magnetic grain in conventional media which helps to achieve high areal densities (small bit size) without compromising the thermal stability and writability issues. The magnetic bits
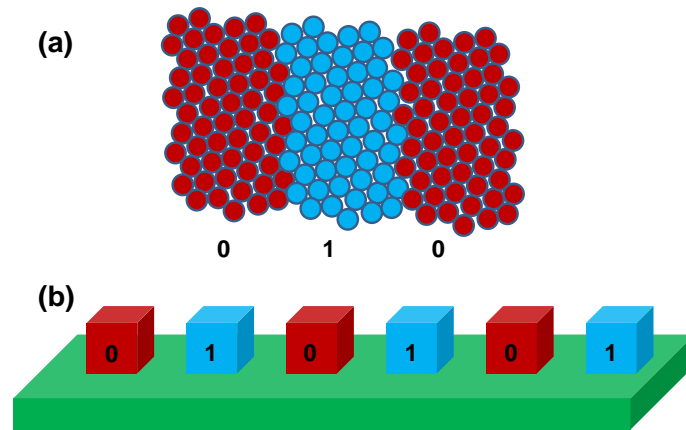
Figure 1.10: (a) Conventional media and (b) BPM

are physically isolated entities, thus there is no transition noise as is present in conventional media due to zigzag boundaries between the magnetic bits. Since the magnetic bits are physically and magnetically isolated in BPM, there is no exchange coupling when the ECC concept is applied in BPM. The combination of ECC and BPM can achieve areal densities beyond 4 Tb/in^2 [40].

1.6.4. Microwave-Assisted Magnetic Recording

Microwave-assisted magnetic recording (MAMR) uses the ferromagnetic resonance effect in order to assist magnetization reversal. An additional microwave ac field is applied to the media during the writing process. A schematic diagram is shown in Figure 1.10. An ac field generator is incorporated with the slider (the slider is the body of material that supports the actual drive head) in order to produce a localized magnetic field with a frequency in the microwave regime. The magnitude of the magnetic field is on the order of few kilo-Oersteds (kOe) and the frequency is in the GHz range. This field is applied at an angle to the existing write magnetic field. Maximum energy is transferred to the magnetic field when the frequency matches the
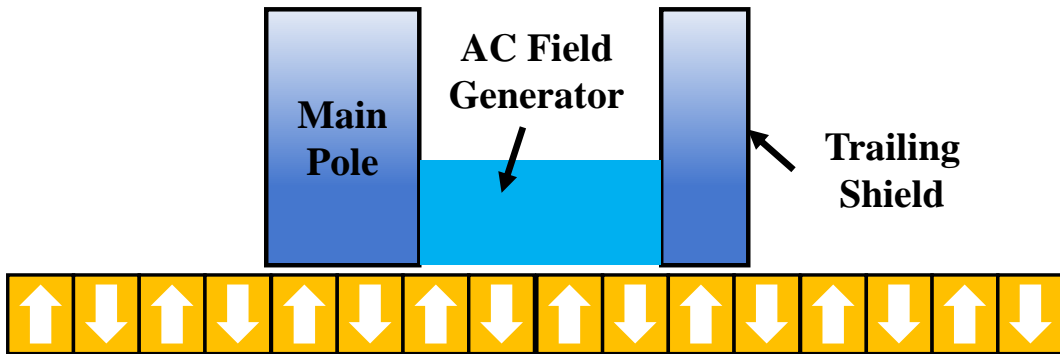
Figure 1.11: Microwave-assisted magnetic recording using a high frequency microwave signal

ferromagnetic resonance frequency of the medium. At this stage, the magnetic reversal can be achieved by using a magnetic field much lower than the coercivity of the magnetic media [41]. Areal densities of up to 700 Gb/in^2 have been demonstrated on commercial media like $CoCrPt\text{-}SiO_2$ using MAMR, with a microwave power of 25 dBm [42]. MAMR is a promising technique to achieve areal densities up to 3.5 Tb/in^2 [43].

1.7. Heat-Assisted Magnetic Recording

The concept of heat-assisted magnetic recording (HAMR) is similar to the concept of magneto-optical recording proposed by Katayama and Saga independently in 1999 [1, 44]. It uses the inverse relationship between the coercivity and temperature of the media, i.e., the coercivity decreases as temperature of a medium increases. In HAMR, a magnetic medium is heated locally above its Curie temperature. This causes the coercivity of the magnetic medium to temporarily drop to zero which allows magnetic switching at a magnetic field much lower than the coercivity of the medium. The medium is then left for fast cooling in the presence of the applied field, which thus results in retention of magnetic information. A schematic diagram of the HAMR

18

writing process and the HAMR principle is shown in Figures 1.11(a) and (b) respectively. A high power laser focused locally on the magnetic media heats it above the Curie temperature; a writing magnetic pole close to the laser spot applies a magnetic field on the heated region before it comes back to the ambient temperature. HAMR thus provides a new degree of freedom by allowing the use of high coercivity media, allowing higher areal densities without compromising the writability issues.

The media should be designed such that its large coercivity is reduced to a level which can be written using a conventionally available magnetic field strength, at a temperature obtainable by the laser source. As shown in Figure 1.11, a HAMR system requires the development of various components such as a light delivery system, a thermomagnetic writer, a robust head-disk interface, and high anisotropy media with a proper thermal design. The use of high anisotropy magnetic media in HAMR promises to achieve order of magnitude higher areal densities than perpendicular recording.

(a)   **(b)**
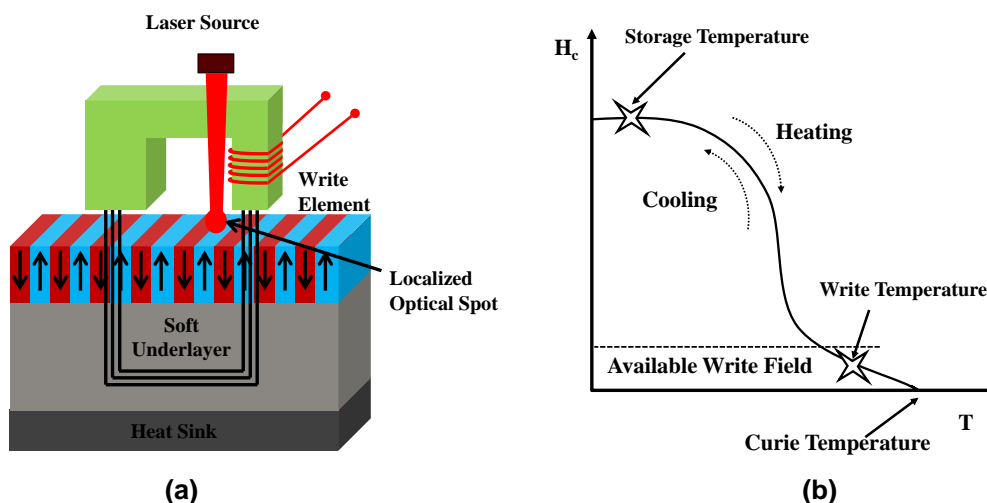
Figure 1.12: (a) Schematic diagram of HAMR (b) HAMR recording principle

1.7.1. The HAMR Recording Process

In HAMR, the temperature of a high coercivity media is elevated, facilitating magnetization switching at reduced magnetic fields and is then abruptly reduced to "freeze in" the information. The magnetic grains have a small volume V and a high magnetocrystalline anisotropy K_u such that the ambient thermal stability factor $\frac{K_u V}{k_B T} \geq 60$ [19]. This value is sufficient to ensure that the magnetic grains remain stable for ~ 10 years. The heating and cooling process is executed within ~ 1 ns which is on the same time scale used in conventional magnetic recording. Another main advantage of HAMR is that it can achieve a high effective magnetic gradient. The following relation explains it in more detail:

$$\frac{dH_{write}}{dx} = \frac{dH_k}{dT} . \frac{dT}{dx} \qquad \text{Eq. 1.9}$$

where H_{write} is the applied magnetic field and H_k is the anisotropy field. The equation shows that the write field gradient depends on two factors: (1) the temperature dependent anisotropy field $dH_k(T)$ gradient and (2) the temperature gradient of the medium at the freezing temperature (down-track or cross-track). A high anisotropy media such as FePt shows a high $\frac{dH_k}{dT}$ slope, which can reach a value of 900 Oe/K [45], which is much higher than the gradient of low anisotropy materials such as CoCrPt alloy. The expected value of the temperature gradient is 5–10 K/nm [6]. With these typical values, a write field gradient (3 to 20) $\times$ larger than the direct write field gradient from inductive head designs is achieved.

1.7.2. HAMR Media

The HAMR system requires fabrication of storage media which can support high storage density with high anisotropy, are thermally stable and have a small grain size. In addition to this, a proper thermal design is required for heat confinement within the media. A schematic of a typical HAMR medium design is shown in Figure 1.12. It has some components in common with PMR, such as an overcoat (OC), a lubricant, a recording layer, a soft underlayer (SUL), and a properly designed interlayer. However, there are some unique aspects of HAMR media. Since HAMR uses heat during the recording process, the media OC and lubricant must be thermally stable. Moreover, a heat sink is required in order to optimize the thermal response of the storage media. Potential candidates for storage media include $L1_0$ FePt, FePd, CoPt, and MnAl, all of which offer high magnetic anisotropy [46-48]. The $L1_0$ order demonstrates high anisotropy in these alloys, and is the Strukturbericht designation for the crystallographic structure.
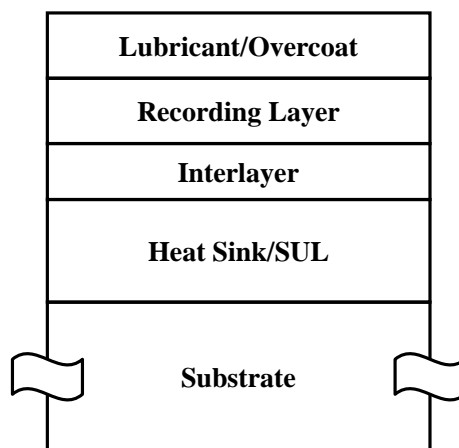
Figure 1.13: Media stack for HAMR recording

A high processing temperature during medium fabrication is required in order to induce the ordering needed to achieve high anisotropy; this results in high media noise, as the high processing temperature can cause the grain growth to adversely affect the microstructure [49]. $L1_0$ FePt shows a modest T_C equal to 750 K and coercivity as high as 14.4 kOe and well isolated grains with diameter of 7.5 nm [50, 51].

1.7.3. HAMR Optics and Head

In order to achieve Tb/in^2 areal densities, it is required to focus laser light to a spot no wider than $\sim (25 \text{ nm})^2$. The optical spot size in this thesis is defined as the full width half maximum (FWHM) of the distributed intensity in the optical spot. A sub-50 nm spot is well below the diffraction limit at optical wavelengths. The diffraction limit is the smallest optical spot size to which light can be focused by standard far-field optics like lenses and mirrors. According to the scalar diffraction theory, the optical spot d is

$$d = \frac{0.61\lambda}{NA} \qquad \text{Eq. 1.10}$$

where λ is the wavelength, and NA is the numerical aperture of the focusing element. Current short wavelength semiconductor lasers are not capable of producing a focused optical spot required for high areal densities due to the diffraction limit. Near-field optics must be used in order to achieve an optical spot beyond the diffraction limit. Near-field optics makes use of nano-apertures or nano-antennas as near-field transducers (NFTs) in order to produce a small sized optical spot on the magnetic media. Different designs for NFTs have been described and developed over the past 15 years to address the problem of obtaining a confined optical spot below the diffraction limit.

1.7.4. Near-Field Transducers

In HAMR, the spacing between the recording head and the magnetic medium is required to be sub-10 nm, to have sufficient resolution at Tb/in^2 areal densities [52]. Thus, near-field optics are the only choice in a HAMR system to achieve optical spot sizes much smaller than the diffraction limit. One of the most challenging problems faced in a HAMR system is to deliver sufficient laser power into a recording medium within a spot well below the diffraction limit.

A nano-aperture is a type of NFT which can be used to get an optical spot size much below the diffraction limit while having sufficiently high transmission. These apertures confine light by virtue of their small size, and transmitted optical power decreases quartically with the diameter of the aperture. The simplest design, a circular nano-aperture, has extremely low transmission efficiency (transmission efficiency is defined as the ratio of the transmitted to the incident power) in the far-field [53].

Therefore it cannot be used for high power applications; a 50-nm circular aperture has a transmission efficiency less than 10^{-5} for visible light [54]. Betzig et al. [55] studied a circular aperture experimentally and obtained an optical imaging resolution of ~12 nm (~λ/43). Nevertheless, near-field intensity distribution and efficiency of an NFT are more important compared to the far-field power efficiency. NFT performance is critical in HAMR systems. Differently shaped nano-apertures have been developed to enhance the transmission while keeping the spot size small. These apertures make use
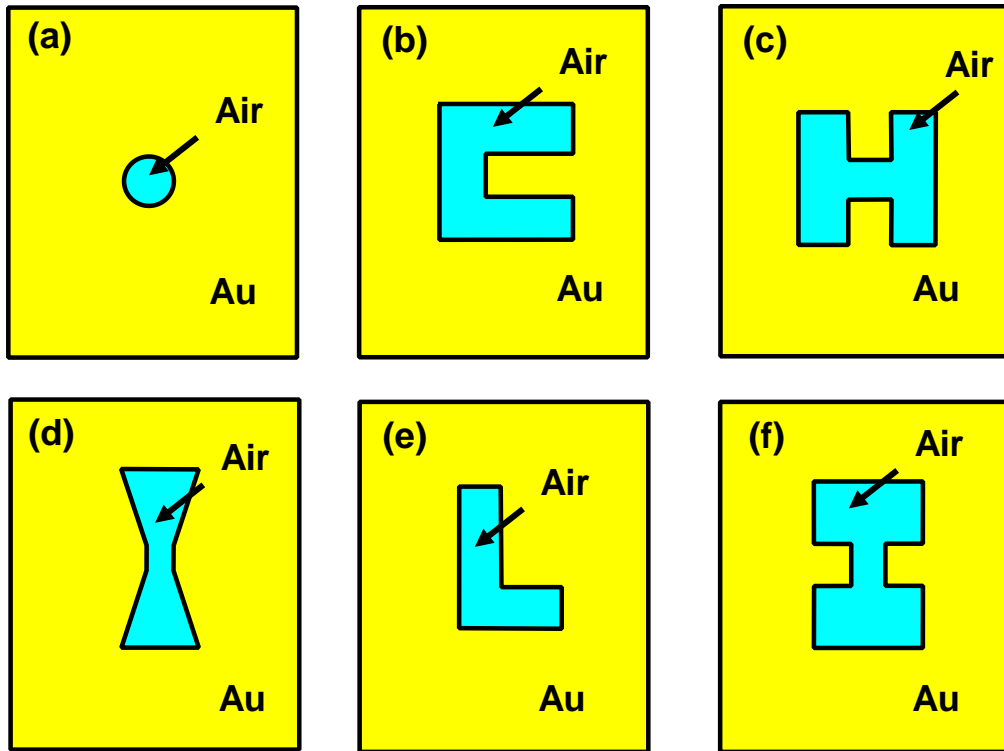
Figure 1.14: Different nano-aperture designs for NFT: (a) Circular aperture,
(b) C aperture, (c) H aperture, (d) Bowtie aperture, (e) L aperture, and
(f) I aperture

of propagating surface plasmons (SPs) on the surface of the aperture and
localized SPs around the metal ridge. By carefully optimizing the aperture
design, the incident area of the aperture for optical power collection can be
wider and the collected power can be funneled through a much narrower hole
which produces a localized optical spot with much high near field intensity.
These include the I shape, H shape [56], Bow-tie [57], L shape [58], half Bow-
tie [59], C shape [60], cross aperture [61] and rectangular slit aperture [62].
Some of these are shown in Figure 1.13. The light propagation through these
apertures is dependent both upon wavelength and polarization. The light is
concentrated at the ridge in the center; by both the lightning rod effect and a
localized SP resonance. Nano-antenna-based NFTs are just as important as the
apertures. Some of the well-known antenna shapes are the Bowtie antenna

24

[63], elliptical particles [64] or nano-wires [65, 66] and the beaked antenna [67-70].

1.8. Conventional HAMR Head

A conventional HAMR system consists of two parts: an optical light path and an NFT device. The optical light path guides the light to an NFT and the NFT device is used to focus the light locally on the magnetic medium. The NFT device is a nano-antenna or nano-aperture. Semiconductor lasers are ideal candidates for HAMR light sources because these lasers can be easily fabricated and integrated in HAMR systems. Figure 1.14 shows the schematic diagram of a conventional HAMR system. A beam from a laser diode is directed towards a waveguide through a grating coupling and is passed to a near-field transducer.
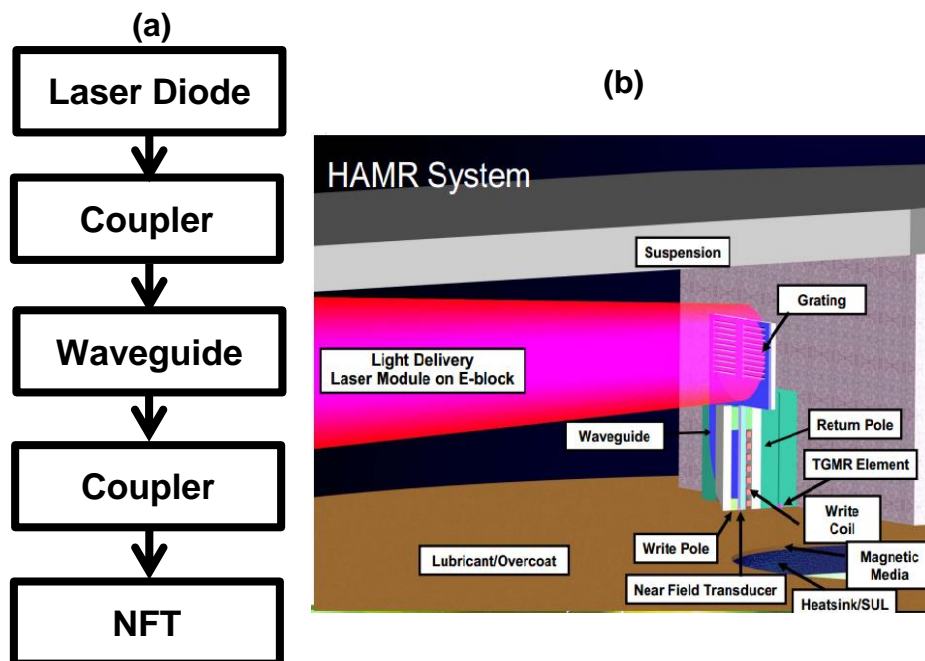
Figure 1.15: A conventional HAMR system [71]. Used with permission.

The near-field transducer then produces a localized optical spot on the magnetic media by focusing the laser light using near-field focusing. There are a few parameters which are required for an efficient and reliable HAMR light delivery system. A HAMR system must:

(1) Be compact in size as current read/write heads are very small in size and the optical system is required to be sufficiently small for easy integration.

(2) Be compatible with the current head fabrication technology. This is necessary to facilitate mass production of HAMR read/write heads without substantial investment in new fabrication facilities.

(3) Have high coupling efficiency. The laser light from the external laser should be coupled to the waveguide efficiently and should be delivered to the NFT with low loss to reduce power requirements.

1.8.1. Previous Work

The first plasmonic HAMR prototype was demonstrated in 2009 by Seagate Technology [72]. A high coercivity FePt medium was used. Figure 1.15 shows a detailed schematic diagram of an NFT, magnetic medium and a full light delivery system. Optical power from a semiconductor laser at a wavelength of 830 nm was focused onto a "lollipop" NFT through gratings and a planar solid immersion mirror (PSIM) waveguide. The NFT design had two parts; a ball-shaped part of the NFT collects the optical field from the gratings and generates an SP mode while the needle part utilizes the same SP to form a localized optical spot on the magnetic medium, thus heating the magnetic medium above its Curie temperature. An areal density of ~ 375 Tb/m^2 was
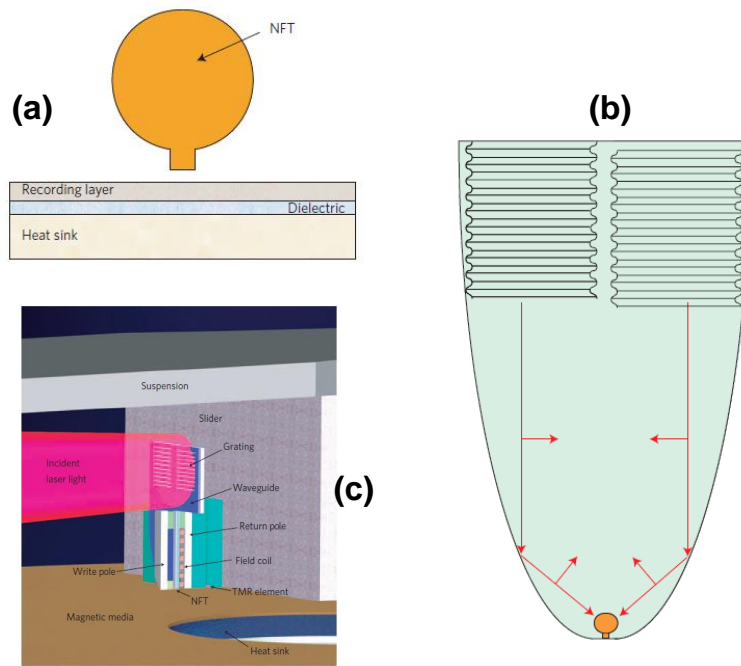
Figure 1.16: HAMR device structure, developed by Seagate Technology, showing (a) the lollipop antenna, (b) PSIM and coupling antenna, and (c) a summarized HAMR system [72]. Used with permission.

successfully demonstrated with the design shown in Figure 1.15.

Another well-known HAMR prototype was introduced by Hitachi Global Storage Technologies (HGST) in 2010 [73]. A detailed description of the system is shown in Figure 1.16. The system contained an 830 nm laser, an objective lens, a waveguide structure and an NFT. The laser light was guided to the NFT through gratings and a waveguide structure. Figure 1.16(a) shows the detailed light delivery system and (b) shows the NFT design and the simulated optical spot produced inside the magnetic medium. An areal density of ~1 Tb/in^2 was demonstrated using high coercivity bit patterned media in this design [73].
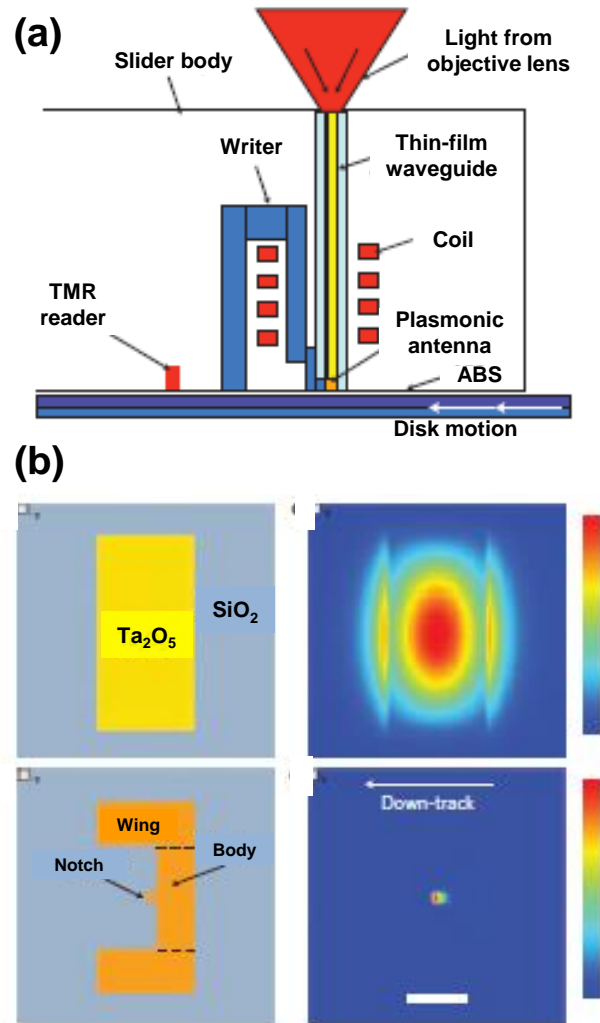
Figure 1.17: HAMR device developed by HGST: (a) HAMR structures, and (b) simulation results for the E-antenna. The scale bar is 200 nm [73]. Used with permission.

1.9. Obstacles in HAMR

1.9.1. Thermal Loading of Slider

The recording head is a magnetic device fabricated on the trailing edge of the slider body to generate magnetic write fields. It is a rectangular block made of a ceramic substrate material, usually a composition of AlTiC. The slider is required to maintain a physical separation from the media, known as the flying height. The flying height is an important parameter in order to maintain a

28

continuous and constant magnitude the magnetic field delivered to the magnetic medium from the writing head. The optical components are integrated close to the head components and the heat losses from the light delivery system can cause the thermal loading on the slider. Thermal loading of the slider can affect the flying height, age of the magnetic device, read-back performance and write efficiency.

1.9.2. Optical Path Integration

The thermal load also includes the losses from the optical path integrated into the trailing edge of the slider. These losses in the optical path are mainly due to the power losses in the optical components such as gratings, optical waveguide and any optical lens used. These heat losses will result in greater power consumption by the laser source which in result will make the HDD more power-consuming.

1.9.3. Sub-Diffraction Limited Optical Spots

The optical spot inside the magnetic medium is controlled by the lateral heat diffusion. In order to achieve an areal density of 10 Tb/in^2, the thermal profile in the recording medium must be less than 10 nm wide. The thermal engineering of the media will not be able to reduce the heat spot size to less than the optical spot because the heat transport is a diffusive process. This implies that the optical spot must be even less than 10 nm. An optical spot of this size can only be achieved using near-field focusing and efficient NFTs must be developed to produce an optical spot much smaller than the diffraction limits.

1.9.4. The NFT Failure

The conventional light delivery system uses a high power laser diode as a light source and the power from the laser source is delivered to the NFT which then confines the light in the magnetic medium. A large fraction of this power is absorbed and dissipated around the NFT which causes overheating of the NFT. The extreme cyclic thermal load can lead to NFT failure after only several tens of recording tracks [72]. The NFT is required to be functional for the full period of a typical product warranty which is usually 5 years. Thus it is necessary to reduce the thermal loading on the NFT.

1.9.5. HAMR Testing

The complex fabrication process has made HAMR testing, using the optical paths integrated with the sliders, challenging even for commercial drive companies. Only a few research institutions and universities are able to manufacture their own test drive setups internally.

1.10. Direct Light Delivery System

This thesis proposes an alternative direct light delivery system for HAMR. The system contains a high power laser placed directly over the magnetic media at flying height, and the laser light is focused on the magnetic medium through a nano-aperture, fabricated onto the front facet of the laser. Nano-aperture VCSELs are potential candidates as a light delivery system in HAMR, with C-shaped nano-apertures on their facets to be used as NFTs in order to produce small localized optical spot, replacing the conventional complex and less efficient light delivery system. Figure 1.17 shows the
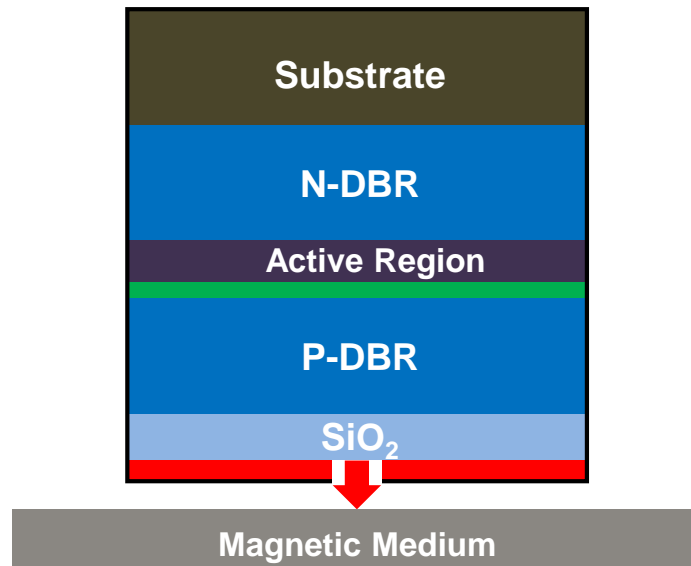
Figure 1.18: Schematic diagram of the direct light delivery system using a nano-aperture VCSEL. The light from the VCSEL is focused on the magnetic medium through a nano-aperture.

schematic of the HAMR light delivery system based on a nano-aperture VCSEL. Laser light emitted from an 850-nm VCSEL is focused on a magnetic medium through a C-shaped nano-aperture. These nano-aperture VCSELs are easy to fabricate and have less power consumption as compared to the conventional HAMR light delivery system. Figure 1.18 shows the side view of a nano-aperture VCSEL. The light emitted from a VCSEL is focused through a nano-aperture fabricated in a Au layer on its facet. The output power depends strongly on the diameter of the nano-aperture.

1.11. Possibilities and Challenges

The main advantage of this light delivery system is the simplicity and easy fabrication process. The optics is highly compact and simplified, contains only one laser and near-field transducer which need no additional optical components. The 850-nm VCSEL is a low cost laser which can be easily fabricated and on-chip testing can be performed also. The laser and the

31
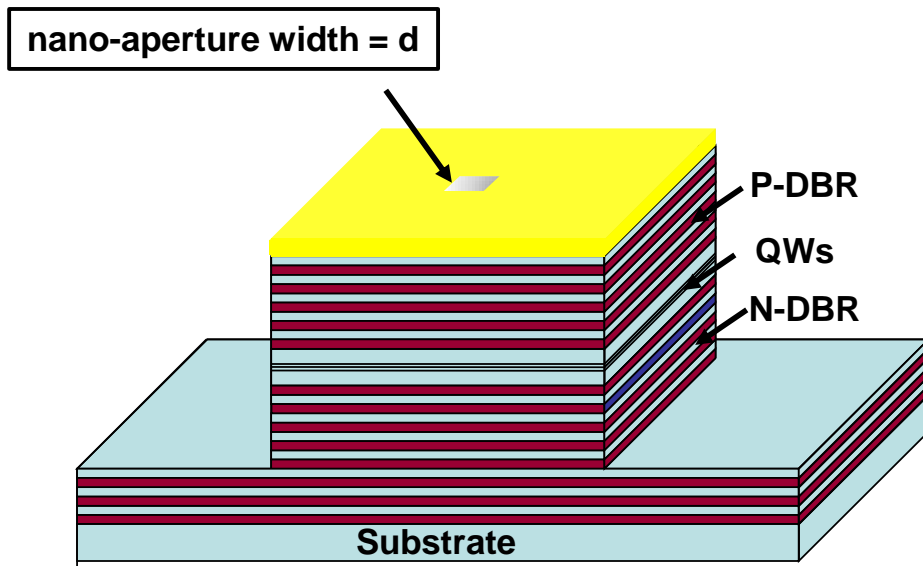
Figure 1.19: Side view of a nano-aperture VCSEL (with emission facet at the top, opposite to that shown in Figure 1.17). The output power changes quadrically as the diameter of the aperture is changed.

near-field transducer can both be fabricated on a single wafer with simple fabrication processes. The conventional light delivery system uses a high power laser as a light source; Seagate used an 80-mW laser source [72]. The laser diode has less than 50% efficiency, therefore there was much more electrical power required to operate their system. VCSELs, however, can be operated at 10-15 mW, thus requiring less electrical power. The main challenge with this system is the complete integration with existing write head designs. The head needs to be modified in order to be integrated with the VCSEL. This challenge is actually a very serious one, and it is beyond the scope of this thesis to fully address this problem. The feasibility of VCSELs in terms of power requirements can, however be demonstrated.

1.12. Outline of Thesis

This thesis has been organized into eight chapters.

Chapter 1 has given an introduction about the history of magnetic storage and the development of hard disk technologies. It provided a brief description of the challenges faced by the magnetic storage industry today and discusses briefly new and evolving technologies. The chapter described the concept of magnetism, magnetization dynamics and HDD history. The conventional magnetic storage techniques, their short comings and the potential future technologies were discussed.

Chapter 2 discusses the fabrication and characterization techniques used to perform the experiments in this thesis. The conventional techniques and the techniques developed for this thesis are discussed in detail.

Chapter 3 investigates the transmission and focusing characteristics of differently shaped nano-apertures using FDTD simulations.

Chapter 4 presents the effect of the magnetic medium on the transmission and focusing characteristics of a C-shaped nano-aperture. The fabrication process for the sample used is discussed and the characterization techniques are explained.

Chapter 5 explains the basics of HAMR, fabrication of the magnetic material, and HAMR writing is demonstrated using a pump-probe optical setup. This chapter discusses the use of C-shaped nano-apertures for HAMR application, for high areal density storage.

Chapter 6 includes an introduction to nano-aperture VCSELs, their fabrication, and their characterization. Differently shaped nano-aperture 850-nm VCSELs are fabricated and the results are presented in this chapter.

Chapter 7 summarizes the thesis and provides the recommendations for future work.

Chapter 2

Experimental Techniques

This chapter discusses various fabrication and characterization techniques used for experiments in this thesis. It includes lithography techniques, magnetic characterization and imaging techniques. Working principles of different instruments have been briefly described. In addition, one of the characterization setups, designed in-house, is discussed and explained in detail.

2.1. Patterning Techniques

2.1.1. Electron Beam Lithography (EBL)

EBL circumvents the diffraction limited performance of traditional photolithography, allowing nanometer scale patterning. EBL uses short wavelength electrons in order to pattern different shapes and patterns on different substrates coated with electron-sensitive resist. A beam of electrons is focused on the resist which reacts depending on its nature, i.e., positive or negative resist. The resolution of patterning depends on the wavelength of the electrons, beam size, focusing, and resist properties. The wavelength of the electrons is calculated by,

$$\lambda = \frac{h}{\sqrt{2 \times E \times m}} \qquad \text{Eq. 2.1}$$

where h is Planck's constant and m, E, and λ are mass, energy and wavelength of the electron, respectively. The wavelength of an electron for an energy of 100 keV is 4×10^{-3} nm. With this wavelength, it is possible to

achieve a sub-10 nm resolution with EBL. In EBL, it is required to scan all the patterns in a serial manner, which makes it time consuming compared to light exposure techniques. An EBL system consists of an electron source (gun), a column with a set of electromagnetic lenses, a mechanical stage and a computer. The gun emits electrons which are scattered in random directions. These scattered electrons enter the column through a mechanical aperture and are focused by electromagnetic lenses into a beam. The stage controls the mechanical motion of a sample under the beam during the scanning process and the computer controls various functions of the system [74]. There are two types of resist used in EBL patterning – positive and negative resist. In a positive resist, the exposed region becomes more soluble in an appropriate solvent termed the developer; whereas in a negative resist, the exposed region becomes less soluble and the unexposed resist is removed by the developer. The patterning quality depends on the solubility of the resist which can be controlled by the electron dose, defined by:

$$D = \frac{t \times I}{A}$$

Eq. 2.2

where D is the dose, defined by the number of electrons per unit area, I is the electron current, t is the exposure time and A is the exposed area [75]. The EBL patterning process is shown in Figure 2.1.

In this project, an E-Line Plus EBL system operating at 20 kV was used to pattern differently shaped nano-apertures in a sub-100 nm regime; with a 40 nm thick poly methyl methacrylate (PMMA) positive resist. The EBL system was used to fabricate nano-aperture VCSELs and HAMR devices to execute experiments for this thesis.
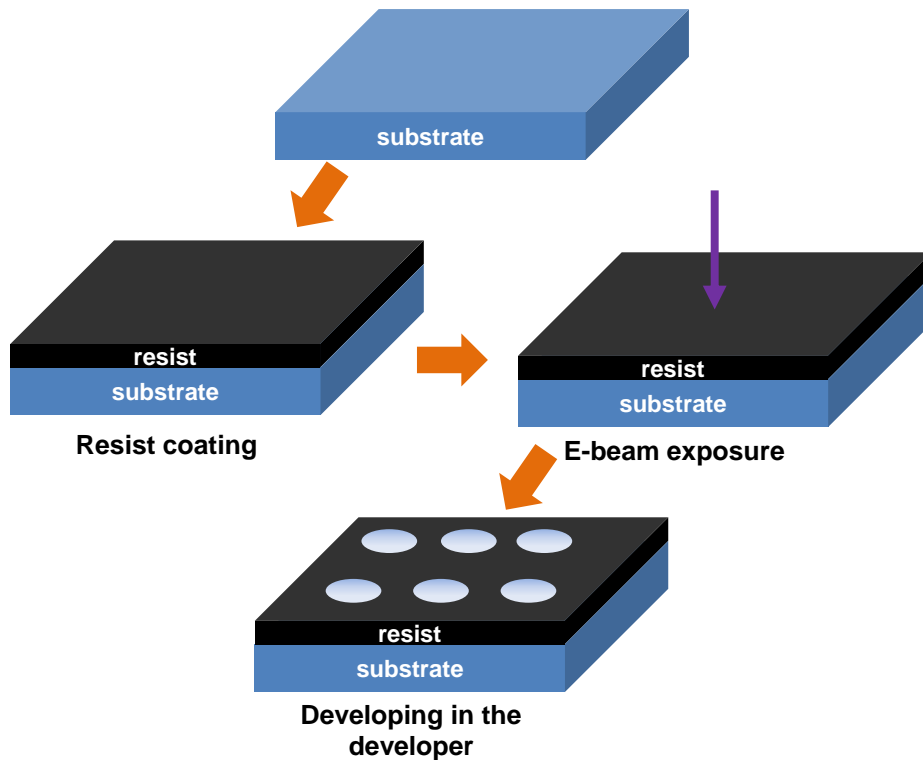
Figure 2.1: A normal EBL process using positive resist

2.2. Characterization Methods

2.2.1. Scanning Electron Microscopy (SEM)

The SEM uses high energy electrons instead of light to form an image. SEM has gained recognition in many fields in the medical and physical science communities. The SEM has a large depth of field. The SEM has high degree of magnification, which makes it possible to examine a specimen at high resolution and the degree of magnification can be controlled by electromagnets.

High energy electrons are generated by an electron gun, at the top of the microscope and an aperture, as in EBL. Electrons and X-rays are ejected from the sample after the beam hits it. The emitted X-rays, backscattered electrons

and secondary electrons are collected by the detectors and are converted into signals. These signals are used for reconstructing the morphology and topography of the sample. This produces the final image [76].

The SEM system used in this work was an FEI NOVA NanoSEM 230 system. The SEM was used to image fabricated devices at different fabrication steps. The system was capable of imaging features as small as 10 nm, and was used to image the differently shaped nano-apertures patterned by EBL. Since the nano-apertures were fabricated in a Au layer deposited on a glass substrate, the imaging was affected by charging. A conducting tape was thus used to avoid charging during the imaging process. An optimization of the controlled mesa etching of the fabricated VCSEL was also performed using SEM imaging. This will be shown later in this thesis.

2.2.2. Vibrating Sample Magnetometer (VSM)

VSM was invented by Simon Foner in 1955. It is used to measure the magnetic properties of materials as a function of applied magnetic field [77]. A schematic diagram of a VSM system is shown in Figure 2.2. The VSM operates on Faraday's Law of Induction, which states that a changing magnetic field will produce an electromagnetic force in a coil. The sample under test is held in a holder between two electromagnets. The magnetic field provided by the electromagnets will align all the magnetic domains in the sample in one direction and the sample will be magnetized. A magnetic stray field around the sample is produced because of the alignment of the magnetic dipoles. The sample is made to vibrate using a mechanical control unit. The
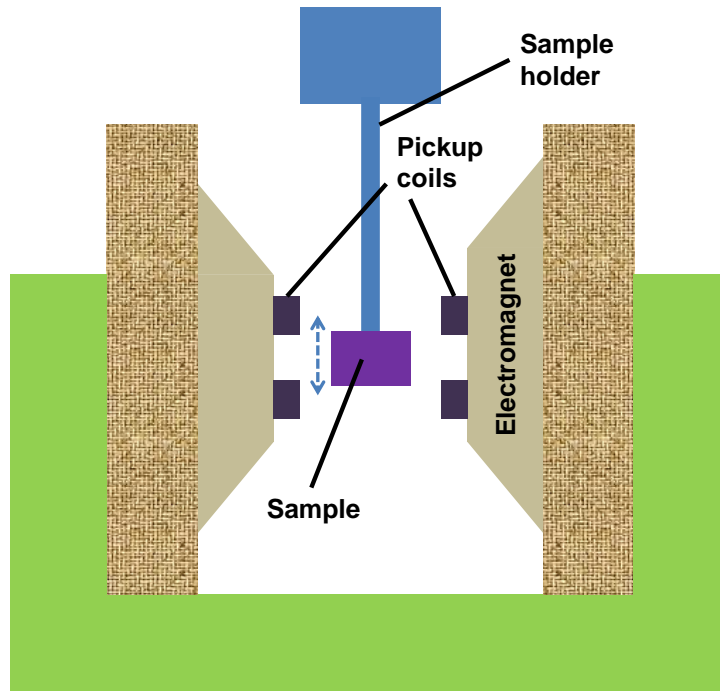
Figure 2.2: Schematic of a VSM; sample holder and detection mechanism

changing stray magnetic field produces a signal voltage in the detecting coils (also called pickup coils). The induction current produced in the coils is amplified by a trans-impedance amplifier and lock-in amplifier. This signal is proportional to a number of factors: the vibration frequency and its amplitude, the magnetic moment of the sample and the sensitivity factor of the coils used. Using the controlling and monitoring software, the system is able to measure the relationship between the sample magnetization and the applied magnetic field [78]. The VSM system used in this project is equipped with a sample holder that can heat a sample to elevated temperatures.

The VSM system was used to measure hysteresis loops of magnetic films. In this thesis this utility was used to measure hysteresis loops of FePt at elevated temperatures by using a sample holder which was equipped with a heater. The instrument was able to apply external fields extending up to 9 T.

2.2.3. Magnetic Force Microscopy (MFM)

MFM is a special type of scanning probe microscopy, and is the best way to characterize magnetic media for different magnetic storage applications. For example, a magnetic layer on a computer HDD can be characterized using MFM. A magnetic medium produces stray magnetic fields on the surface which are scanned by a tiny ferromagnetic probe, yielding a magnetic map of the surface. MFM was introduced following atomic microscopy [79] and gained importance in early 1990s as a vital technique that offers high imaging resolution without the need for special sample preparation or environmental conditions. The diagram of a typical MFM system is shown in Figure 2.3. This technique uses a ferromagnetic sharp tip which is attached to a flexible cantilever. The tip is closely scanned over the magnetic surface (at a height of 10–100 nm) and interacts with the stray fields emanating from the sample. The tip is scanned laterally with respect to the sample and an image is formed by measuring the force gradient as a function of position. An image taken with an MFM tip contains information about both the surface topography and the
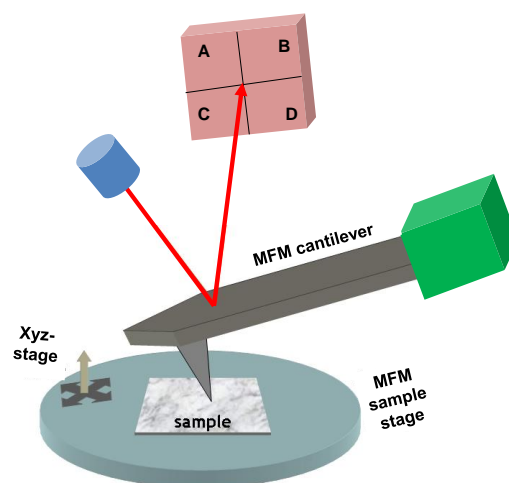
Figure 2.3: Magnetic force microscopy setup, showing the tapping needle and the detection laser

magnetic properties of the surface [80]. In MFM, the tip is scanned in lift mode. In the lift mode, the resonant frequency is affected by the variation in the magnetic field strength arising from the sample. The change in oscillation frequency of the cantilever is detected by measuring its phase of oscillation with respect to the drive frequency of a piezo actuator [81].

A Veeco® scanning probe microscope in MFM mode was used to study magnetic devices after HAMR in this thesis. The silicon tips were provided from VEECO; they were doped with antimony and were coated with cobalt. The resonant frequency lies between 60 and 90 kHz. The samples were DC magnetized before each HAMR experiment. MFM resolution was limited to ~ 30 nm because of the tip size [82].

2.2.4. Magneto-Optical Kerr Effect Microscopy (MOKE)

MOKE is a traditional method for magnetic imaging using conventional imaging optics. It is one of the most useful techniques in image domain and magnetization processes. This method makes use of the magneto-optical Faraday or Kerr effect which arises from an interaction between an incident electromagnetic signal and magnetic domains in a sample. The Kerr effect is the rotation in polarization of incident light upon reflection from a non-transparent magnetic sample. This polarization rotation depends upon the orientation of the magnetic domains in the magnetic sample. This rotation is converted into a domain contrast by using an analyzer in the reflected beam path of the light. The weak domain contrast can be enhanced by digital image processing. Kerr microscopy can virtually extract domain contrast from any

ferromagnetic or ferrimagnetic sample. No specific surface treatment or sample preparation is required for this process.

The optical design of the Kerr microscope built for this thesis is shown in Figure 2.4. It contained simple optical components such as a Glan-Thomson linear polarizer, beam splitter, lens, charged-coupled device (CCD) camera, laser light source and a high magnification objective lens. The sample is placed on a three dimensional translation stage in order to move a sample in any required direction. The light source is a green light emitting diode (LED) which is coupled with a multimode optical fiber. The light is passed through a collimating lens, a polarizer, a beam splitter and is then focused on the sample by an objective lens. After illumination on the sample, the light is reflected with a change in polarization, amplitude and phase due to the MOKE. Changes in polarization are dependent on the magnetization orientation inside the sample.
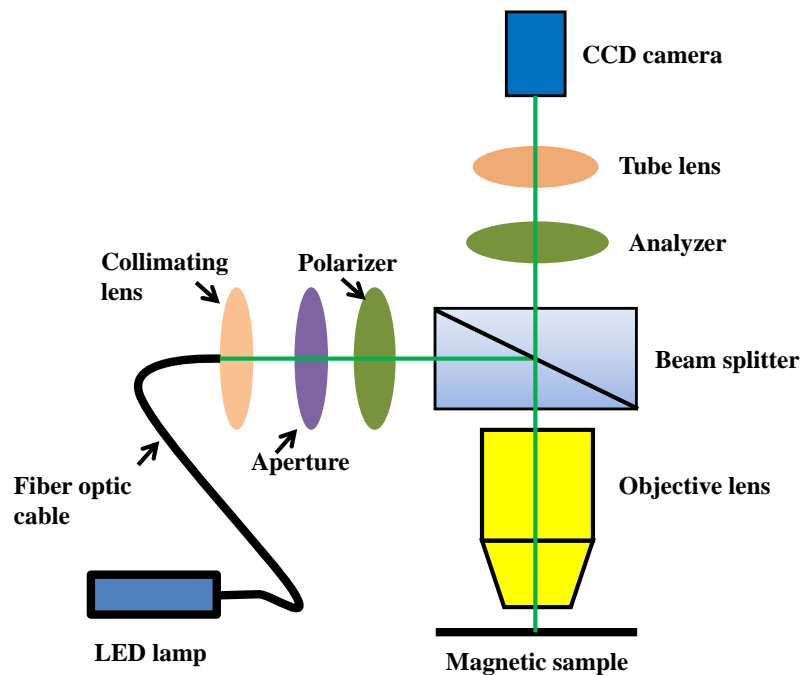
Figure 2.4: Schematic of a Kerr microscope with all the optical components

41

The reflected light passes through an objective lens, a beam splitter and analyzer, and is then focused on a CCD camera by the tube lens. The analyzer is perpendicularly crossed with the polarizer and functions as a filter for the light which reflects off the sample without a change in polarization. Only the light with a change in polarization can pass through the analyzer and was detected on the CCD camera. The signal collected at the CCD is processed using digital image processing and produces a magnetic image showing the magnetic domains. Kerr microscopy is used to obtain a large scan range, but lower resolution images of samples prior to MFM imaging.

2.3. Summary and Conclusions

Multiple fabrication and characterization techniques used for this thesis were described in this chapter. Some of these techniques are commonly known and are used on a large scale, whereas MOKE was developed for this thesis. These techniques were very helpful for device fabrication and are used to achieve fully functional devices for HAMR experiments. Fabricated devices are characterized by SEM and MFM, and the Kerr microscope is used for magnetic imaging. Different NFTs are designed and characterized using finite-difference time-domain (FDTD) simulations in the next chapter.

Chapter 3

Near Field Transducer for HAMR

An NFT's primarily function is to produce a localized optical spot on a magnetic medium to heat it above its Curie temperature. Localized SPs, high transmission efficiency and easy integration are important parameters for an NFT. FDTD simulations are a helpful tool for NFT design and to analyze its characteristics. The diffraction limit, near-field focusing, and operation of different NFTs is described in the following sections.

3.1. An NFT Figure of Merit

For different types of transducers, different parameters or figures of merit are important. In case of nano-apertures, "throughput" is used as a characterization parameter; "peak field intensity" is used in case of nano-antennas. These two parameters are used to characterize transducers operating in isolation. However, in a real application, a transducer is placed in close proximity to a recording medium. The storage medium is composed of magnetic layers with other metallic layers underneath. Therefore, a medium is expected to interact with an NFT, affecting its transmission and focusing characteristics. Moreover, the substrate used underneath the magnetic medium can also modify the near-field intensity distribution of an NFT. Therefore, any figure of merit used to characterize an NFT must include the effect of the magnetic medium and the substrate. The near-field intensity from an NFT in free space does not provide precise performance information for HAMR.

The effect of the magnetic medium on the near-field intensity distribution from a bow-tie antenna has been previously studied [83]. When a bow-tie antenna is placed in close proximity to a magnetic medium, it produces two large optical spots directly underneath each triangle instead of generating one optical spot in the gap between the triangles. This effect makes the bow-tie antenna unsuitable for HAMR. In case of nano-apertures, throughput of light into free space is often quoted as a characterization parameter. However, this also does not include the effect of the recording medium and is also not useful as a HAMR figure of merit. For example, a circular aperture produces a confined optical spot in isolation on the opposite side of the aperture. However, in the presence of a magnetic medium, a waveguide is formed between the metal film of the aperture and the recording medium, which forces the optical spot to extend away from the aperture and therefore the resulting spot is much larger than the aperture itself [6].

In HAMR, two parameters are important: (1) the size of the optical spot within a medium and (2) the amount of the optical power absorbed by a recording medium within this spot. It is difficult to cover both parameters in a single figure of merit. Different NFTs can be compared for a specific optical spot size by measuring the optical efficiency of the NFTs inside the recording medium within that spot. The optical efficiency is defined as the ratio of the power dissipated within the medium to the power incident upon the NFT. The power dissipated within the magnetic medium is calculated by integrating the whole volume as shown in Equation 3.1.

$$P_{diss} = \frac{1}{2} \int_{medium} Re(\sigma)|E^2|dV \qquad \text{Eq. 3.1}$$

where $Re(\sigma)$ is the real part of the conductivity of the recording medium at the frequency of the incident light and $|E^2|$ is the magnitude of the local field intensity [6].

3.2. NFT Design Principles

There are a few design principles that can be used to optimize the HAMR NFT, and they are as follows:

(1) The localized SP resonance effect is highly important for an NFT, which can enhance the near-field intensity by a factor of five or more [6]. The NFT should be able to make use of the SP resonance. This enhanced intensity is directly translated into greater power dissipation in the magnetic medium. The NFT must be composed of a metal which has a large SP effect and can therefore generate a high SP spot intensity. HAMR takes place at a very high temperature; the Curie temperature for a recording medium is around 700 K. This requires the NFT material to have a very high melting point. There are a few options suitable as an NFT material depending upon the wavelength. Metals such as Au, Ag, Cu, and Al are considered as low loss metals which can generate SP resonances at visible wavelengths. However, both aluminum and silver are not suitable because of their low melting points. Melting point of Au is 1064.43 °C. Considering the metals' corrosion resistance, Au is regarded to be the best choice as an NFT material.

(2) The excitation wavelength is also very important for SP effects. Au NFTs can be used over a wide range of wavelengths; stronger SP effects are generated at wavelengths longer than 700 nm [6].

(3) The shape of an NFT is very important in order to deliver enough power to a very small spot size to achieve areal densities beyond 10 Tb/in^2. At such an areal density, the FWHM optical spot size is less than 50 nm (less than $\lambda/10$).

(4) The coupling efficiency between the focusing element and the NFT is very important in order to transfer maximum power to a magnetic medium. The intensity distribution at the NFT is a function of the focusing element design and the method of focusing light onto the NFT. Different focusing elements will couple light differently to an NFT.

(5) The cost and fabrication process is important for mass production of an NFT. Therefore, the manufacturing process for the NFT should be compatible with standard thin-film and lithography-based fabrication processes.

3.3. Near Field Transducer and Surface Plasmons

It is necessary to understand the mechanism through which NFTs overcome the diffraction limit. The explanation can be adapted from [84, 85]. Let us consider a monochromatic light with a wavelength λ, propagating in a Cartesian coordinate system. The associated wave vector is $k = \frac{2\pi}{\lambda}$, and the momentum of each photon is $p = \hbar k$, where $\hbar$ is the reduced Planck constant. The uncertainty principle states that $\Delta p_x . \Delta x \geq \frac{\hbar}{2}$. In this case,

$$\max\{\Delta\,p_x\} = p_x = \frac{2\pi\hbar}{\lambda} \qquad\qquad \text{Eq. 3.2}$$

and

$$\min\{\Delta x\} = \frac{\left(\frac{\hbar}{2}\right)}{\max(\Delta\,p_x)} = \frac{\lambda}{4\pi}. \qquad\qquad \text{Eq. 3.3}$$

The term $\frac{\lambda}{4\pi}$ is the possible smallest spot size which can be achieved by using any kind of focusing optics, which is on the order of $\sim\lambda$. This shows that shorter wavelengths can achieve smaller optical spots.

There are several methods to shorten the wavelength of light. One of the most well-known of these methods is the use of an oil immersion lens such as solid immersion lens (SIL) or a solid immersion mirror (SIM). A purely imaginary wave vector leads to a wave which does not propagate and instead decays exponentially in the direction of the vector. However, if the light wave is travelling along an interface of two different materials, an imaginary wave vector can be realized on one side of the interface. It is necessary to understand the optical properties of noble metals in order to understand the formation of an imaginary wave vector.

Most NFTs are designed using noble metals such as Au or Ag. The calculated permittivity for Au according to the Drude-Sommerfeld model (i.e., the free electron model), at optical wavelengths is shown in [84]. The obvious difference between Au properties and that of dielectrics is that the real part of the permittivity has negative values and the imaginary part is not negligible. Detailed calculations show that the values differ significantly from the free electron model at wavelengths below ~700 nm.

The complex permittivity ε of Au, at a red wavelength is about $-10 + 2i$, and the permeability μ is 1 at optical frequencies for Au [84]. The index of refraction n for Au at optical frequencies, calculated from $n = \sqrt{\mu\epsilon}$, is almost purely imaginary. A purely imaginary n leads to a purely imaginary propagation constant k_{medium} , calculated by

$$k_{medium} = \frac{2\pi}{\left(\frac{\lambda}{n}\right)} \qquad \text{Eq. 3.4}$$

A wave incident along an Au layer decays exponentially inside the Au due to the purely imaginary k_{medium} . The main advantage of this special property is its ability to focus beyond the diffraction limit at a metal/dielectric interface. In Figure 3.1, an interface of Au and a dielectric material is shown. The free electrons inside the Au are affected by electromagnetic waves and in its response, collective oscillations are produced, which are SPs [86]. Let us consider an electromagnetic wave travelling along the interface in the positive x direction. There can be two possible conditions 1) the problem can be viewed as a time-dependent surface charge distribution, illustrated in Figure 3.2(a); or 2) it can be viewed as a propagating electromagnetic wave travelling along the interface, illustrated in Figure 3.2(b). The following discussion is adapted from [86]. E_z^d and E_z^m represent the electric field in the dielectric and in the metal, respectively. These quantities can be written as

$$E_z^d = E_0^d e^{ik_z^d z} e^{ik_{sp} x} \qquad \text{Eq. 3.5}$$

$$E_z^m = E_0^m e^{-ik_z^m z} e^{ik_{sp} x}. \qquad \text{Eq. 3.6}$$
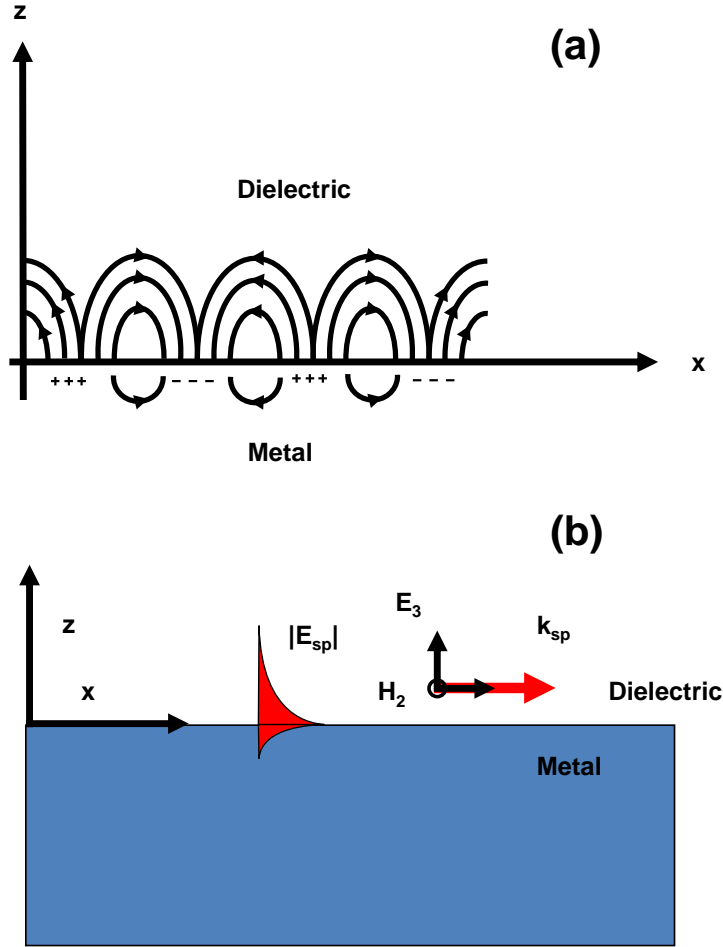
Figure 3.1: An electromagnetic wave travelling along the interface. It can be viewed as (a) a time-dependent surface charge distribution and, (b) propagating electromagnetic wave. Adapted from [86, 87].

The dispersion relationship of the SPs can be found by applying E and H continuity conditions at $z = 0$,

$$k_{sp} = k \sqrt{\frac{\varepsilon_1 \varepsilon(\omega)}{\varepsilon_1 + \varepsilon(\omega)}}, \qquad \text{Eq. 3.7}$$

where k is the free space wave vector and $k = \frac{2\pi}{\lambda}$. k_{sp} is a complex number due to the complex $\varepsilon(\omega)$. The real part of k_{sp} indicates a propagating SP mode and its imaginary part indicates the decay of the SP mode.

3.4. Introduction to Finite Difference Time Domain simulations (FDTD)

The FDTD method is used to solve Maxwell's equations numerically on a fine orthogonal mesh [88]. FDTD has been used extensively in the design of nano-photonics, wireless communication, photonic crystals, nano-apertures and nano-antennas, due to its simplicity, accuracy and efficiency. The following are advantages of the FDTD method:

(1) This method can be used to simulate various complex geometries for an object under analysis.

(2) It can be used to simulate different types of incident signal waves such as short pulses, continuous waves, plane waves and waveguide modes. The transmission spectrum of a system can be simulated in a single run which is useful for investigating resonant behavior of a system.

(3) Various types of media can be successfully simulated. These include anisotropic, dispersive, non-linear, conductive, active, passive media and periodic media.

(4) It is accurate and robust. The sources of numerical error are well known and can be taken into account to achieve necessary accuracy.

(5) The information about every electrical and magnetic signal can be acquired at every location and time point in the simulation space.

Despite these advantages, there are a few drawbacks associated with FDTD simulations, the main disadvantage being the requirement of large computational memory and speed. The FDTD method was developed by Kane Yee in 1966 [87]. Yee developed a set of finite-difference equations for the
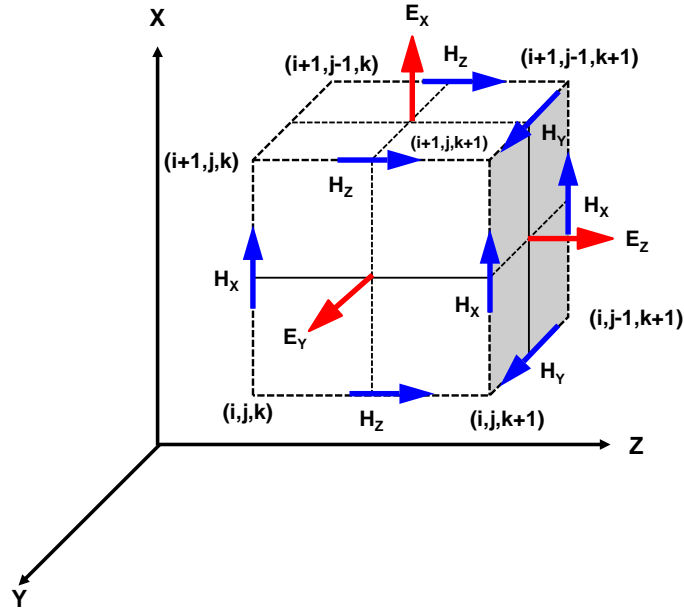
Figure 3.2: The Yee Cell and the field locations. Adapted from [89].

time-dependent Maxwell equations. In this scheme, a simulation space is first defined and then further divided into grid of spacing Δx, Δy and Δz in the spatial domain and Δt in the time domain. The E and H fields are offset from each other by a half grid point in space. This is illustrated in Figure 3.2. Each E-field component is surrounded by four H-field components, and each H-field component is surrounded by four E-field components. In the time domain, the E and H fields follow a leapfrog arrangement. The resultant cell is referred to as a Yee Cell [88].

3.5. Simulation Setup

Figure 3.3 shows a side view of a 3D FDTD simulation model used in this thesis. It contains a plane wave source which radiates a propagating signal. The plane wave is incident on the device under test (DUT) which is usually a nano-aperture in this thesis. The transmitted and reflected signals through and from the DUT are detected by a virtual detector, which can measure several

51

optical quantities. The simulation space is surrounded by an absorbing boundary condition (ABC). These absorbing boundaries were used so that there would be minimal non-physical backward reflections. A perfectly matched layer (PML) is the most common type of ABC. It has been shown that it can successfully suppress noise power due to reflections, to as low as - 80 dB of the incident power [90]. The size of the simulation space depends upon the required resolution in order to accurately represent the scattering structure. In general, for large structures, a resolution of at least $\lambda/(10n)$ is required where n is the highest refractive index used in the simulation space. The simulation space is 2 µm $\times$ 2 µm $\times$ 1 µm in X, Y and Z directions. The simulation mesh is 0.1 µm $\times$ 0.15 µm $\times$ 0.5 µm. The simulation mesh was required to cover the DUT only. The simulations are performed at a 0.02 µm grid size. The monitor is used to measure the near-field intensity. The simulation results are presented in chapter 3.
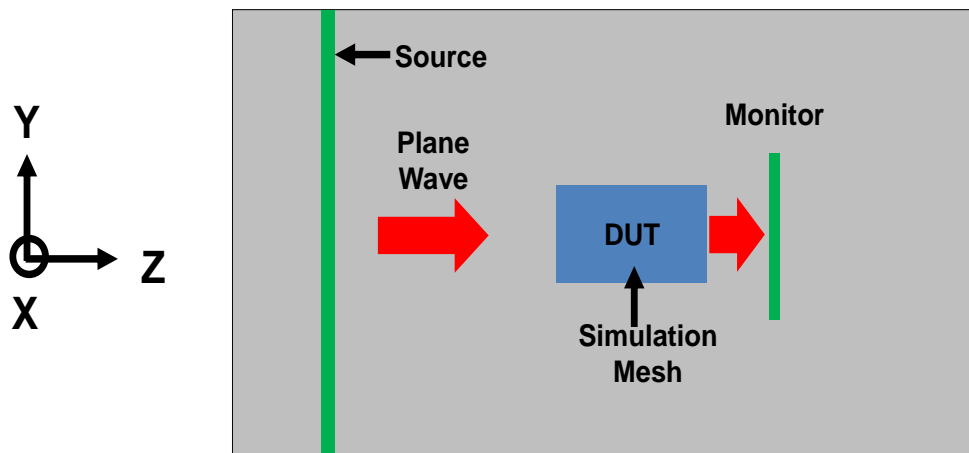
Figure 3.3: Layout of the simulation setup

3.6. Simulations of Differently Shaped Nano-apertures

As discussed before, far-field optical systems suffer from the diffraction limit, which limits their resolution. The optical spot size obtained from a focusing object in a far-field optical system is given as:

$$R = \frac{0.61\lambda}{NA} \qquad \text{Eq. 3.8}$$

where λ is the wavelength of the light and NA is the numerical aperture of the lens system. The numerical aperture is calculated as:

$$NA = n \sin \theta_c \qquad \text{Eq. 3.9}$$

where n is the refractive index of the medium and θ_c is the half angle of the collection cone of the objective lens. As discussed in previous chapters, near-field optics is the only solution in order to achieve resolution beyond the diffraction limit. A circular aperture is the simplest example for near-field focusing. The power throughput of a circular aperture is defined as the ratio of the power transmitted through the aperture over the power incident onto the aperture. It was predicted by Bethe [91] that the throughput of a circular aperture scales as the fourth power of the aperture size when the aperture size is much smaller than the incident light wavelength. Figure 3.4 shows a schematic illustration of the situation. When $w < \lambda$, the power throughput is defined by the following relation:

$$\text{Power Throughput (PT)} = \frac{\text{Power}_{\text{transmitted}}}{\text{Power}_{\text{incident}}} \propto \left(\frac{w}{\lambda}\right)^4 \qquad \text{Eq. 3.10}$$
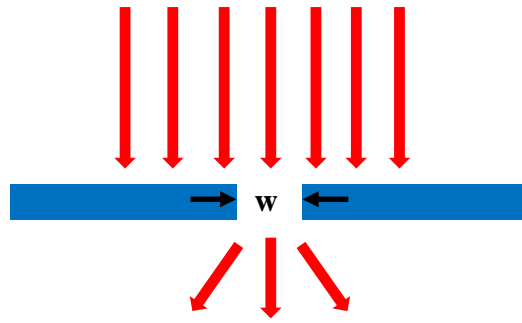
Figure 3.4: Transmission of a plane wave through a nano-aperture

To design an NFT at the required wavelength of 850 nm, FDTD simulations were performed to compare the transmission and focusing characteristics of different nano-aperture designs. The simulation setup is shown in Figure 3.5. A plane wave with a wavelength of 850 nm and linearly polarized in the X direction (shown with red arrows in the Figure 3.5) was incident on the nano-aperture in an Au layer, from a SiO$_2$ substrate. To avoid reflections from the boundaries, absorbing boundary conditions (ABC) were utilized.
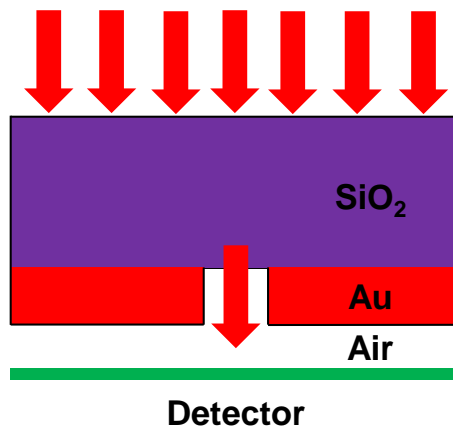
Figure 3.5: Schematic of the simulation setup

Table 3.1: Properties of the materials used in simulation setup

Material	Thickness (nm)	n	k
SiO$_2$	340	1.453	0
Au	100	0.154	4.908

54

The objective of the simulation study was to investigate the near-field intensity distribution through nano-apertures. The materials, thicknesses and the optical properties [92] materials at a 850-nm wavelength are summarized in Table 3.1. The near-field intensity was measured at 10 nm from the nano-aperture. A square aperture was simulated first. The dimensions and near field intensity through a square nano-aperture is shown in Figure 3.6. The intensity was normalized by the incident intensity. These results showed that the transmission through the square aperture was extremely small and the transmitted intensity was much lower compared to the incident intensity. The transmission dependence on the size through a square aperture has already been reported and discussed. This thesis investigated the application of a
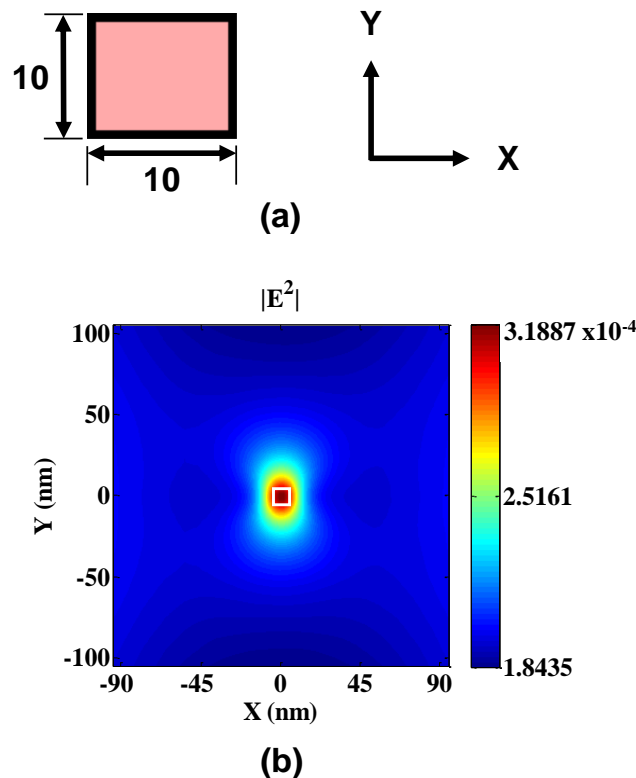
Figure 3.6: (a) the square aperture geometry (b) the near-field intensity distribution through the square aperture (simulated)

square aperture as a near-field transducer in HAMR for 10Tb/in^2 areal densities and results showed that the power through the square aperture was extremely small. This raised the importance of developing new geometrical shapes for nano-apertures with high transmission and strong localized plasmonics effects. Differently shaped nano-apertures have been developed to enhance the transmission while keeping the spot size low. These include the I-shape [56], H-shape [93], Bow-tie [94], L-shape [95], half Bow-tie [96], C-shape [97], cross-aperture [98] and rectangular slit aperture [99].
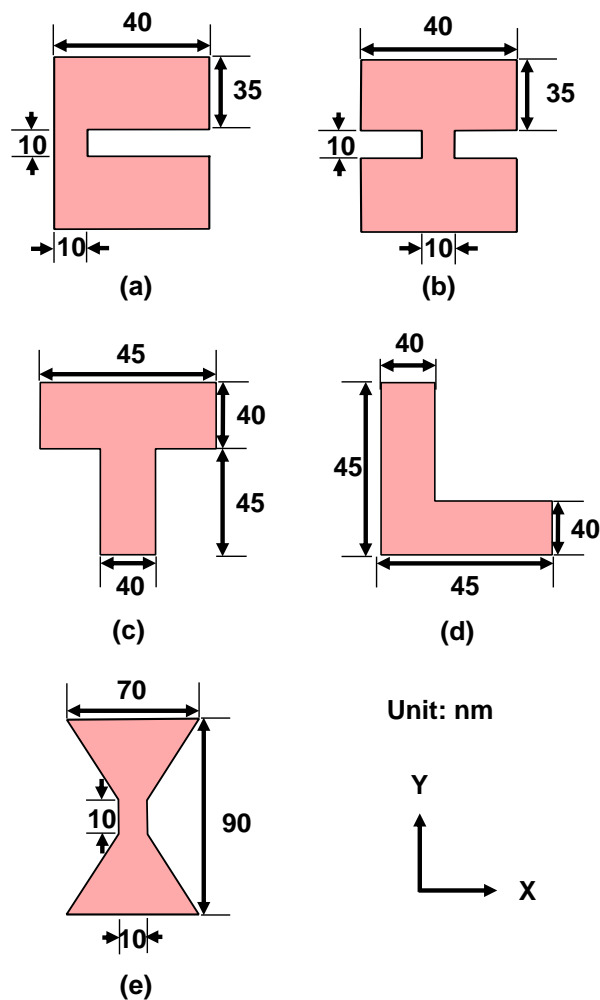
Figure 3.7: Schematic structure of the nano-apertures. a) C-aperture; b) I-aperture; c) T-aperture; d) L-aperture; e) Bowtie aperture

In this thesis, FDTD simulations were performed to compare the transmission characteristics of these nano-apertures. The apertures were optimized to achieve an optical spot close to 10 nm in diameter, and maximum near-field intensity. The detailed structures of the nano-apertures are shown in Figure 3.7.
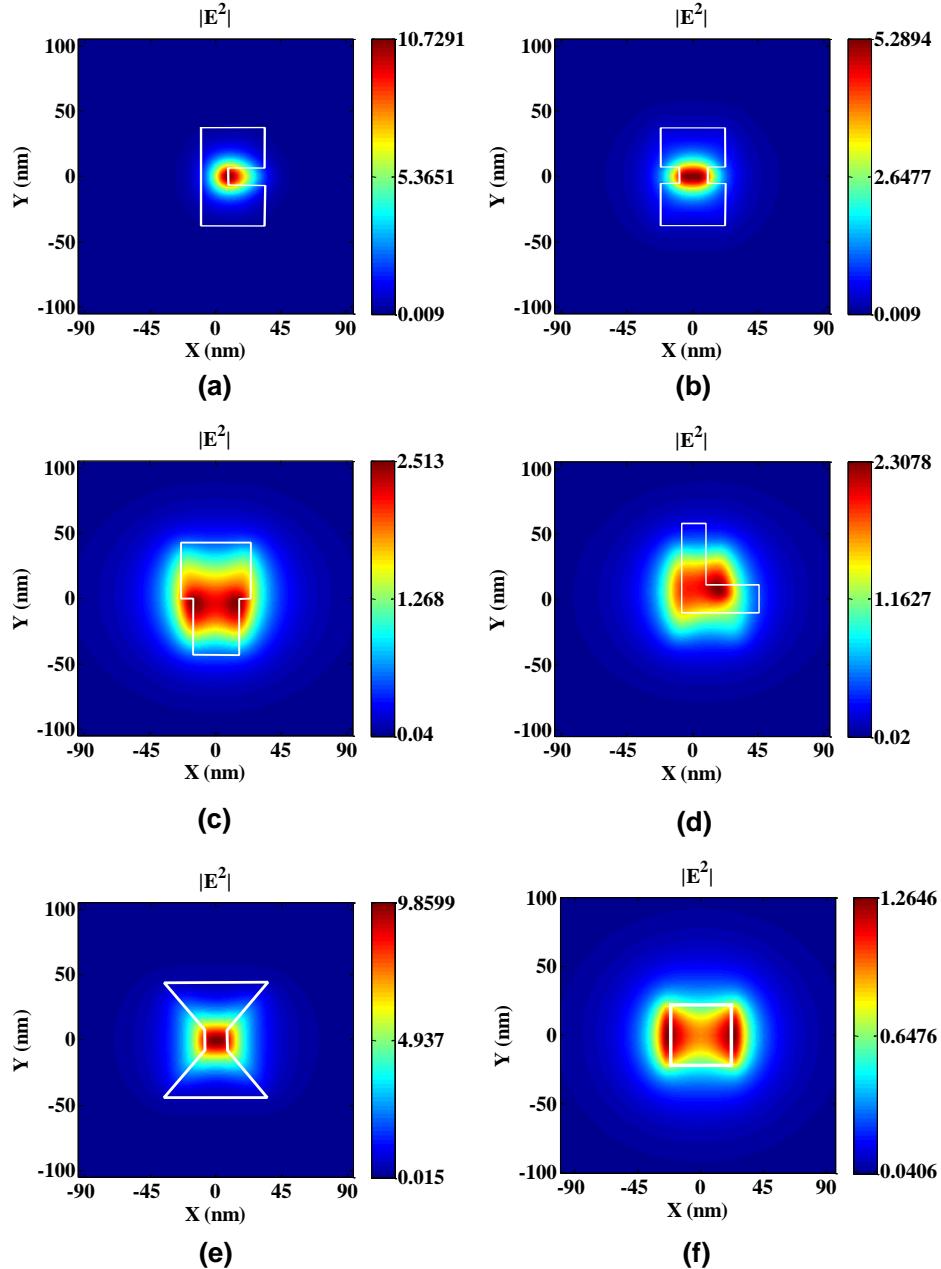
Figure 3.8: Simulated near-field intensity distribution 10 nm away; a) from the C- aperture; b) from the H-aperture; c) from the T-aperture; d) from the L-aperture; e) from the bowtie aperture; e) from the square aperture. The incident light is polarized in X direction.

All dimensions are in nm. The transmission area for all apertures was the same, equal to ~ 2900 nm^2. The results are shown in Figure 3.8. All the results were normalized by the peak intensity through a 10 nm square aperture measured at 10 nm away from the square aperture (shown earlier). The normalized results help to understand the intensity enhancement through differently shaped nano-apertures compared to a square aperture. It can be seen from the results that these nano-apertures produced near-field intensities much larger than the square aperture with a comparable optical spot size. Table 3.2 shows a summary of the transmission and focusing characteristics of the nano-apertures simulated above. The optical spot size and the near field intensity can be optimized by changing the geometrical parameters in order to meet the requirements. From the results, it can be seen that the C-shaped nano-aperture showed the maximum intensity with having the smallest optical spot, compared to the other non-conventional shapes. These characteristics make the C-shaped nano-aperture the best candidate as an NFT for HAMR applications.

Table 3.2: Transmission and focusing characteristics of differently shaped nano-apertures. The incident light is polarized in X direction.

	$\dfrac{|E^2|_{max}}{|E^2|_{max\,(sq)}}$	FWHM (nm)	
		X	Y
C	14.5325	25	18
H	2.4119	34	20
L	3.1638	53	42
T	7.7364	62	51
Bowtie	6.1005	35	27
Square	1	20	15

William A. Challener [100] performed similar simulations to compare use of nano-apertures and nano-antennas as near-field optics in HAMR and reported similar results. In this thesis the simulations have been performed by keeping the transmission area same for all nano-apertures to have more accurate comparison of the transmission characteristics.

3.7. Plasmonic Enhancement Through C-aperture

The intensity through the nano-apertures can further be enhanced by using a plasmonic enhancement method. A Au nano-particle (NP) can be inserted in a C-aperture to enhance the plasmonic effect in a C-aperture. A schematic used for these simulations is shown in Figure 3.9. A C-shaped nano-aperture is shown with an Au particle in the center. The height of the NP was equal to the thickness of Au layer. A 850-nm wavelength plane wave was incident on the nano-aperture through a SiO_2 substrate. The thickness of the Au and SiO_2 layer were 340 nm and 100 nm, respectively. The results were measured in the form of intensity enhancement (I.E.) which is defined as the ratio of the near-field intensity with and without the Au nano-particle.

$$I.E. = \frac{\text{peak near field intensity with the Au NP}}{\text{peak near field intensity without the Au NP}} \qquad \text{Eq. 3.11}$$

The diameter of the NP was varied from 10 nm to 100 nm and the peak near field intensity was measured. The results are shown in Figure 3.10. It can be seen from the results that near-field intensity increased as the diameter of the Au NP was increased, reached a maximum value when the diameter was 60 nm, and started decreasing beyond that. The increase in the near-field intensity is due to constructive interference between the local surface plasmons excited by the Au particle and the ridge of the C-aperture.
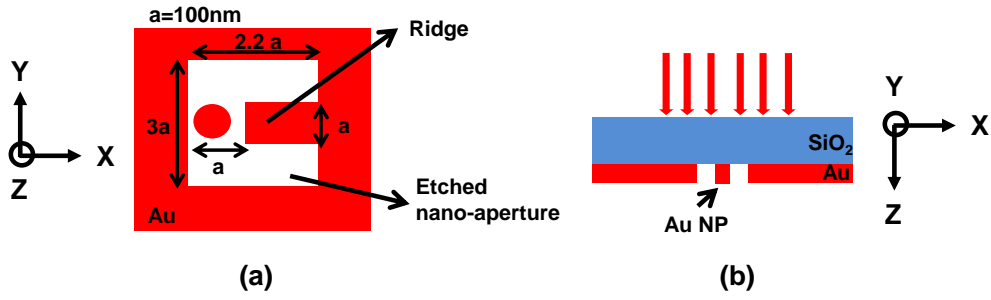
Figure 3.9: Schematic diagram showing a C-aperture with a Au NP in the center, (a) the top view and, (b) cross-sectional view
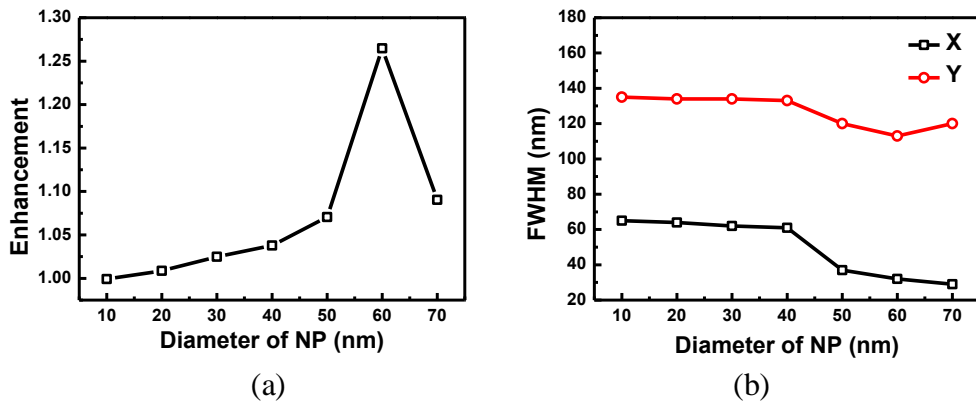
Figure 3.10: Simulated near-field intensity from a C-shaped nano-aperture is enhanced as a function of diameter of a NP placed inside the C-aperture. Intensity enhancement is maximum for a NP with a diameter of 60 nm (a). Similarly the optical spot produced by C-aperture varies as the dimater of the NP is varied, shown in (b)

The optical spot remained unchanged for smaller NPs and was reduced for larger NPs, which is also an advantage for high resolution focusing applications. The maximum intensity enhancement was achieved when the NP diameter reached 60 nm. The near field intensity was further enhanced by increasing the number of Au NPs and optimizing the distance between these NPs. Table 3.3 shows a summary of results achieved by using different number of Au NPs with a fixed diameter of 60 nm. The results show that it is possible to achieve a single optical spot using multiple NPs. The results also

Table 3.3: The summary of transmission characteristics of a C-aperture with using multiple NPs

No. of Au Particles	Intensity Enhancement	FWHM (nm)	
		X	Y
No-particle	1	49	83
1 particle	2.85	37	80
2 particles	4.62	36	79
3 particles	5.87	36	77

show that an intensity enhancement almost equal to 6 is possible to achieve without any significant change in the optical spot size.

3.8. Summary and Conclusions

A detailed description of diffraction limits and advantages of near-field focusing were provided. FDTD simulations were performed to study transmission characteristics of conventional square aperture and unconventional apertures such as C, I, L, T and Bowtie apertures. Unconventional nano-aperture shapes showed enhanced transmission over a square aperture which shows their importance as a near-field transducer in near field applications such as HAMR. Differently shaped nano-apertures showed near-field intensity much higher than that of the square aperture, with a localized optical spot. The C-aperture showed the maximum near-field intensity and the smallest optical spot size in comparison to other apertures. Geometric parameters were optimized in order to achieve the maximum near-field intensity for a 10-nm aperture. The optimization process shows that the intensity and optical spot size depend strongly on the geometrical parameters of the aperture.

The C-shaped nano-aperture is the best candidate as a near-field transducer for HAMR applications because of its superior transmission and focusing characteristics and is considerably easier to fabricate compared to the other shapes. All simulations were performed in free space whereas in a practical HAMR system, a storage medium is included and therefore it is required to include any effect of magnetic media during characterization of NFTs. This will be explained in the next chapter in laboratory tests with fabricated samples.

Chapter 4

Effect of Magnetic Medium on NFT Performance

In actual HDD systems, a storage medium is included in the near field of an NFT, and can strongly influence the performance of the NFT. Therefore, it is important to study the transmission characteristics of an NFT in presence of the magnetic material in the near field. Because a magnetic medium is a metal, it is expected to affect a nano-aperture's performance by changing its interaction with the incident light beam [101]. The simulations and experiments described in this chapter are used to study the change in the transmission and focusing characteristics of a C-aperture in the presence of a nearby magnetic medium.

4.1. Absorption Characteristics of FePt

High anisotropy materials are required to overcome the superparamagnetic effect in order to obtain an areal density of 10 Tb/in^2 and beyond. FePt is a strong candidate for storage media in HAMR applications due to its high anisotropy and moderate Curie temperature. In HAMR, the absorption characteristics of the magnetic medium are very important. It is the percentage of incident power, absorbed inside a magnetic medium, which is important at a certain wavelength and polarization. The absorption characteristics of FePt depend on its thickness and the polarization of the light wave focused on the medium and, of course the nano-aperture dimension and the metal used. Figure 4.1 shows a schematic diagram of the optical setup used to measure the absorption of FePt in this dissertation.
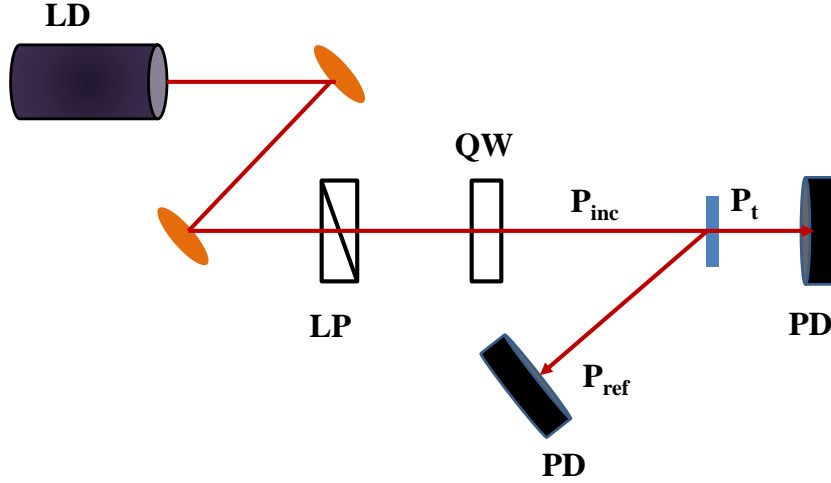
Figure 4.1: Schematic of the optical setup used to measure the absorption of a magnetic medium

Light from a diode laser having a wavelength of 850 nm was incident on an FePt film deposited on a glass substrate. A linear polarizer (LP) and quarter-wave plate (QW) were used to control the polarization of the light signal. The magnetic film was deposited on a glass substrate and was fixed on a sample holder. A set of samples with different medium thicknesses; 2–15 nm was prepared, in order to observe the effect of medium thickness on the power absorption. The magnetic medium had a low coercivity of ~ 500 Oe. The light passed through the LP and QW plate and was incident on the magnetic film. The transmitted (T) and reflected (R) beams were measured using two photo-detectors and the absorption (L) was calculated as

$$L\,(\%) = 100 - \{T\,(\%) + R\,(\%)\} \qquad \text{Eq. 4.1}$$

The absorption was measured for different FePt thickness values and for different polarizations of the incident light; the results are shown in Figure 4.2.
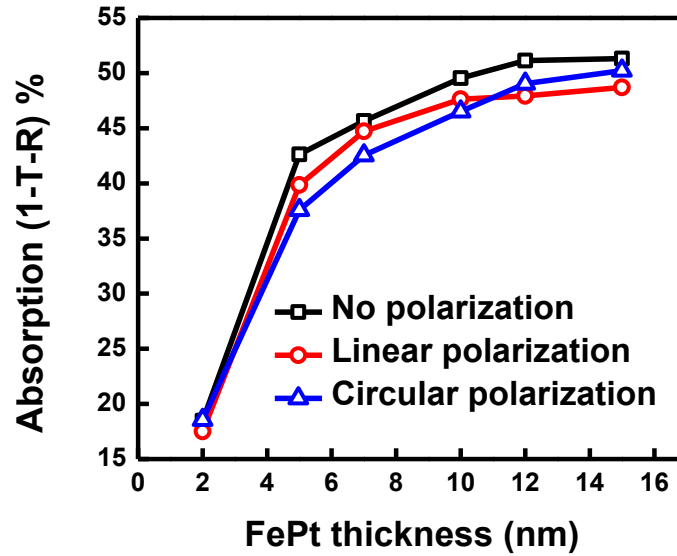
Figure 4.2: Polarization dependent characterization of FePt. Different polarization orientations show the same optical characteristics (experimental).

The results show that absorption in FePt is largely independent of the incident beam polarization; it depends primarily on the thickness of the magnetic medium. The orientation of linear polarization is not specified here because there was no difference in results for different orientations of the polarization of the incident light. Similarly, left-handed and right-handed circular polarizations had the same absorption, so the handedness was not mentioned in the figure. The absorption depends on the thickness of the magnetic medium. The absorption increased drastically as the thickness of the FePt was increased from 2 nm to 5 nm, became more linear from 5 nm to 10 nm, and after that became saturated. For a 10-nm thick magnetic medium, 45 ~ 50 % incident light was dissipated inside the medium.

For HAMR applications, the medium thickness should be as low as possible (to reduce the overall writing field requirements), but at the same time absorption needs to be maximized for efficient heating.

4.2. Effect of FePt on The Transmission Characteristic of The NFT

Being a metal, FePt is expected to affect a nano-aperture's performance by changing its interaction with the incident light beam. FDTD simulations were performed to observe the effect of FePt on the performance of an NFT. The objective of the simulations was to investigate the effect of a nearby storage medium on the near-field intensity distribution. The simulation setup and the C-aperture geometry are shown in Figure 4.3. A C-aperture was formed inside a Au layer with dimensions ℓ = 40 nm, α=10 nm and L= 3α =30 nm. The underlayers in the stack are used to achieve $L1_0$ chemical ordering in order to obtain high coercivity in the FePt magnetic medium. A plane wave with a wavelength of 850 nm linearly polarized in the X direction was incident on the nano-aperture in a Au layer, from a SiO_2 substrate. To avoid reflections from the boundaries, ABC were utilized.
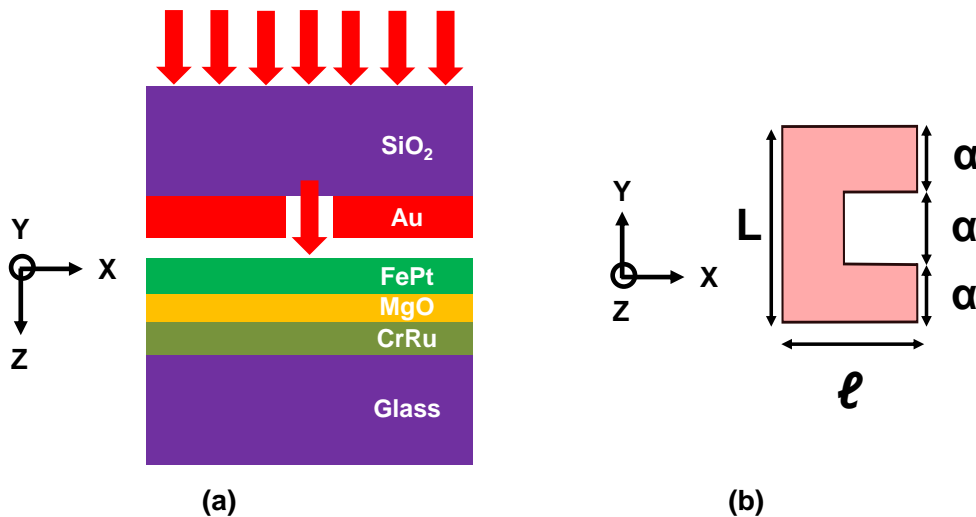
Figure 4.3: (a) Schematic of the simulation setup, and (b) geometry of the C-aperture

The materials, thicknesses and the optical properties [59, 92, 102-104] of the materials at 850 nm wavelength are summarized in Table 4.1.

Table 4.1: Properties of the media stack

Material	Thickness (nm)	n	k
SiO_2	340	1.453	0
Au	100	0.154	4.908
FePt	10	3.3	4.3
MgO	4	1.72	0
CrRu	20	3.15	5.68

4.3. Fly Height Effect

Fly height is distance between an NFT and the magnetic storage medium during the writing and reading process in a magnetic storage system. Transmission efficiency of an NFT is significantly affected by the fly height [105]. As mentioned earlier, the fly height must be reduced to less than 7 nm in order to achieve an areal density of 1 Tb/in^2 However, for areal densities of 10 Tb/in^2 all the dimensions are expected to be approximately three times smaller than at 1 Tb/in^2. This will require a fly height of about 2 nm [106, 107].

Figure 4.4 shows the effect of fly height on the performance of the C-aperture (shown in Figure 4.3). Figure 4.4 (a) shows that the focusing characteristics became worse with increasing fly height and the optical spot size increased in both X and Y dimensions as the fly height increased. The effect was almost linear along both profiles. Considering the X dimension, FWHM was 20 nm at a fly height of 2 nm and the FWHM was 30 nm at an 8 nm fly height.
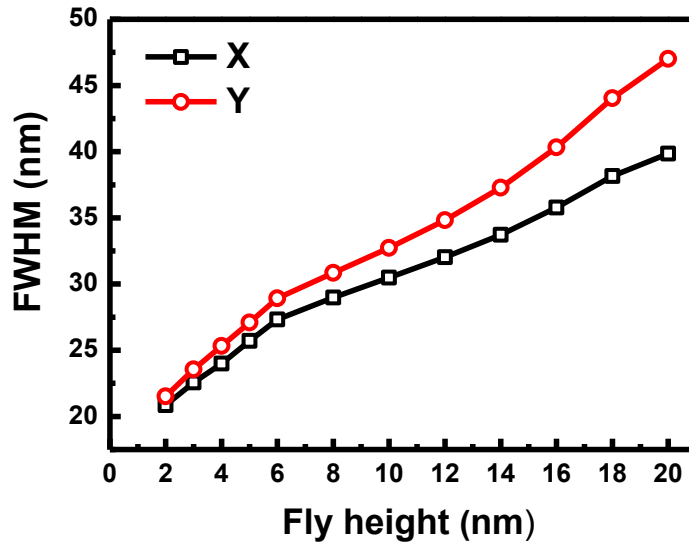
(a)
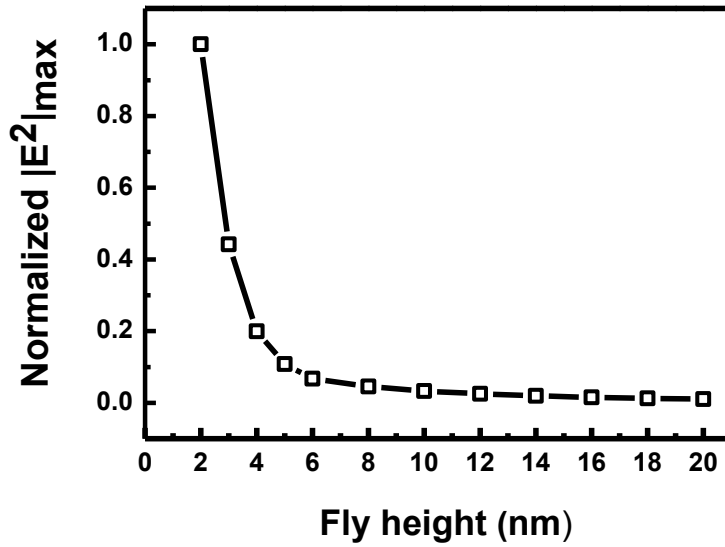
(b)

Figure 4.4: Effect of fly height on (a) optical spot size and (b) normalized near-field peak intensity (simulated)

This showed a 50% increase in spot size when fly height is increased from 2 nm to 8 nm. This was due to the diffraction effect which results in a larger optical spot as the detector is moved away from the NFT. Figure 4.4 (b) shows effect of fly height on the near-field intensity produced by the C-aperture. The results are normalized by the maximum near-field intensity achieved at fly

height equal to 2 nm. From the results, it can be seen that the near-field peak intensity decreased as the fly height increased. The results showed an exponential decay in the near-field intensity with a change in the gap between the storage medium and the NFT. The localized electric field obtained by the NFT is composed of evanescent and propagating fields. The evanescent field is stronger than the propagating field in the near-field of the NFT. It was theoretically shown by Bethe [91] that the evanescent field decays rapidly as the detector moves away from an aperture in a metallic film. When the magnetic medium is placed in the near field of the NFT, the evanescent fields are absorbed by the lossy magnetic medium and thus stronger power dissipation is obtained in the magnetic medium. The peak intensity reduced by 90% as the fly height changed from 2 nm to 10 nm. A lower fly height will help to enhance the NFT performance but reducing fly height induces other challenge in reducing the thickness of the protective and lubricant layers that are normally deposited on a magnetic medium.

4.4. Effect on Resonant Transmission of The NFT

4.4.1. FDTD Simulations

It has been previously described in detail that intensity enhancement in the C-aperture is due to polarization and resonance effects. The resonant wavelength is an important parameter for NFT design. Every transducer has maximum transmission at its resonant wavelength; the resonant point depends primarily on the dimensions of the NFT. The resonant wavelength of the C-aperture is determined by the surface current distribution which can be controlled by its arm length [97, 108]. The resonance of a plasmonic structure is expected to be

affected by interaction with a metallic surface and the resonant wavelength can be shifted strongly depending upon the separation between the plasmonic structure and the metal, as well as on the metal thickness [109, 110]. Similarly, it is expected that the resonant wavelength of a C-aperture is also affected by the presence of the magnetic storage medium (i.e., FePt), as its metallic properties will interact with and reflect/scatter light, causing a change in the resonant behavior of the C-aperture. Transmission spectra were studied using FDTD simulations, with and without the storage medium, in order to observe the effects of the magnetic medium on the resonant wavelength of a C-aperture. A simulation setup, similar to the one shown in Figure 4.3, was used. The dimensions used for C-aperture are as follow: ℓ = 220 nm, α = 100 nm and L = 3α = 300 nm. The transmission spectra were simulated for different values of FePt thickness (T) and the results are shown in Figure 4.5.
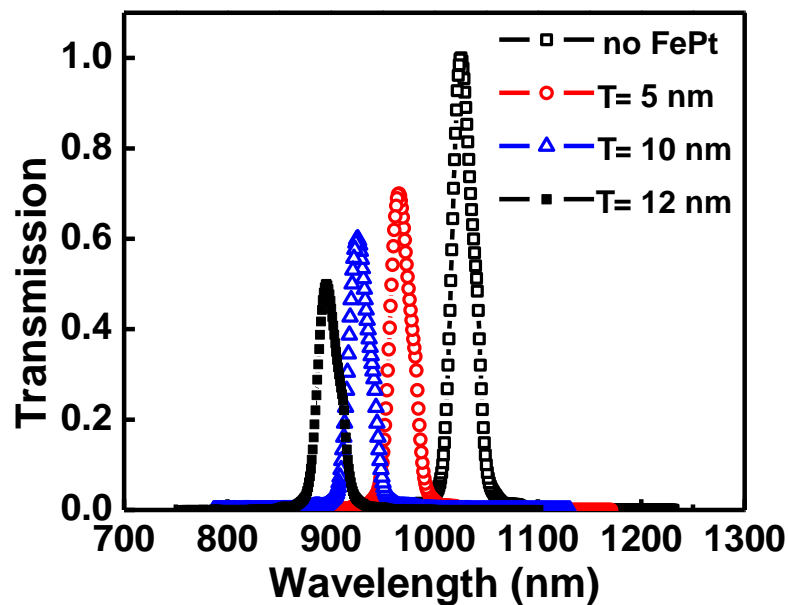
Figure 4.5: Simulated transmission spectra of a C-aperture for four different FePt thicknesses

A blue shift in resonant wavelength with increasing thickness can be seen from these graphs. All the results were normalized to the spectrum obtained without FePt, and in all simulations, wavelength-dependent index values were used.

The storage medium, being a metal, causes the light reflected from it to cause a change in the surface charge distribution which is expressed as a change in the resonant wavelength. The amount of reflection from the storage medium depends upon its thickness which resulted in a variable resonant wavelength shift. The resonant shift will be different for different metals since both reflection and absorption depend on the complex refractive index [111].

4.4.2. Sample Fabrication

The simulation results above were verified by experiment. Samples were prepared in a cleanroom using in-house facilities on thin glass substrates. Borosilicate glass (Borofloat 33, Schott Glass) of size 30 cm^2, 2.2 mm thickness and surface roughness < 2 nm, was used for this experiment. The fabrication steps are described in detail below:

(a) Cleaning The Glass Substrates

A few steps were followed to ensure that the glass surfaces were clean for Au film deposition. These include cleaning in acetone (10 minutes) and isopropanol (10 minutes) in an ultrasonic bath. The samples were rinsed in distilled water for 5 minutes, followed by N$_2$ blow-drying.

(b) Au Deposition

An Au film of 100 nm thickness was deposited using electron beam evaporation. A high vacuum ($\sim 2 \times 10^{-6}$ millibar) was used in order to ensure a smooth and uniform deposition of the metal. A 100-nm thick Au layer can completely block light outside an aperture window in the experiment.

(c) Spin Coating And Lithography

EBL was used to pattern the C-shaped nano-apertures in the Au layer. The maximum beam acceleration voltage available is 25 kV. Positive tone PMMA 950k (from MicroChem USA) in a 1:4 ratio with the thinning agent Anisole, was used as a resist. The spin coater used in this work was a Spin 150-NPP model from SPS-Europe. The thickness of resist was estimated to be 40 nm. The samples were pre-baked at 180 °C for 2 minutes. The EBL dose ($\mu C/cm^2$) for lithography of C-shaped nano-apertures was optimized after few test runs. The samples were developed in a solution of Methyl isobutyl ketone (MIBK): Isopropyl alcohol (IPA) (1:3) for 40 seconds (s).

(d) Dry Etching (ion milling)

An Ar-based ion miller was used for Au etching. In the ion-miller, Ar^+ ions were accelerated and bombarded the sample directly. This etches or removes materials from the surface. Most resists are etch-resistant to Ar^+; the etch selectivity is quite high and only exposed metals are etched. The etching time is optimized for the 100-nm Au layer.

(e) Resist Removal

The substrate was washed in remover PG (a solvent used to remove PMMA 950k). Leftover resist was removed in an ozone striper. Since the deposited film is Au, which is an inert metal, the ozone has no effect on the metal. The resist removal is performed at 100 °C with a 0.5 liter per minute oxygen flow.

(f) SiO_2 and FePt Deposition

A 10-nm layer of SiO_2 was deposited on the Au layer to work as a spacer layer between Au and the magnetic medium. This spacing is provided to take into account the head–media spacing which ranges from 10 nm–15 nm in practical storage systems. The magnetic medium was then deposited in an AJA sputter tool. The coercivity of the medium was ~500 Oe; but it was the reflection which was more important for this analysis, which is independent of the coercivity of the medium.

The fabrication process flow is shown in Figure 4.6. Figure 4.7 shows SEM images of the etched C-apertures (an array and a zoomed in image of a single C-aperture).

4.4.3. Measurement Setup and Results

In order to increase SNR and obtain spectra of the C-apertures, 500 μm × 500 μm arrays of the nano-apertures were fabricated. The spacing between the nano-apertures was 1 μm. This was done to make sure that enough power can pass through the apertures and reach the photo-detector. The optical setup used

is shown in Figure 4.8 (a) and Figure 4.8 (b) shows two configurations for the measurements.

(a) Metal Deposition

(b) Spin Coating

(c) EBL

(d) Dry Etching

(e) SiO₂ Deposition

(f) FePt Deposition
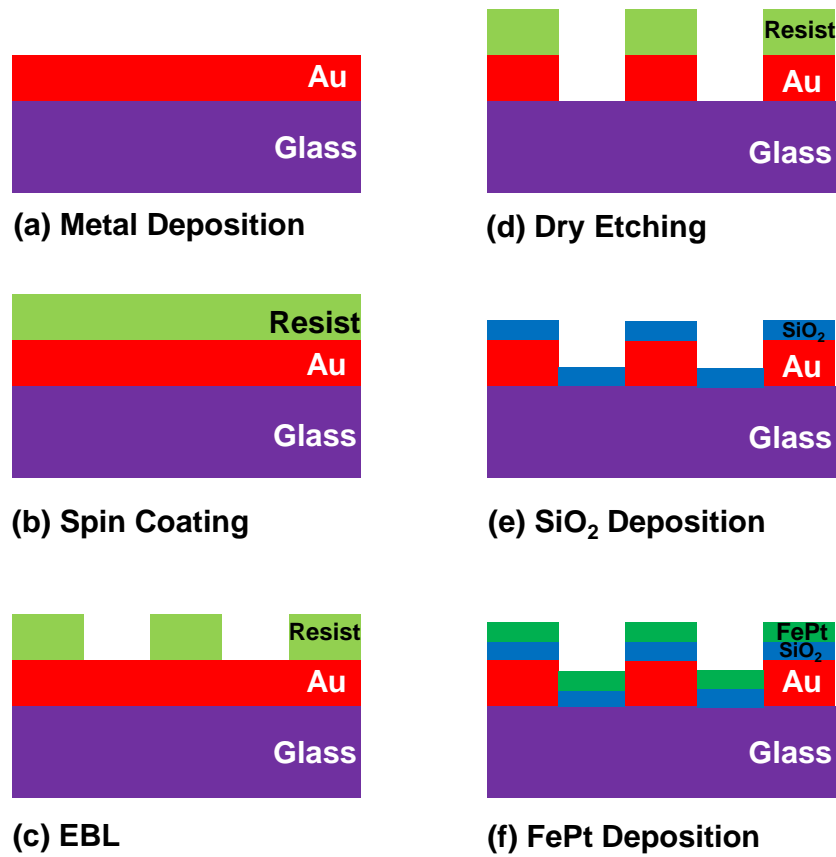
Figure 4.6: Fabrication process for the sample used in these measurements. The process includes steps such as deposition, resist coating, lithography and dry etching.
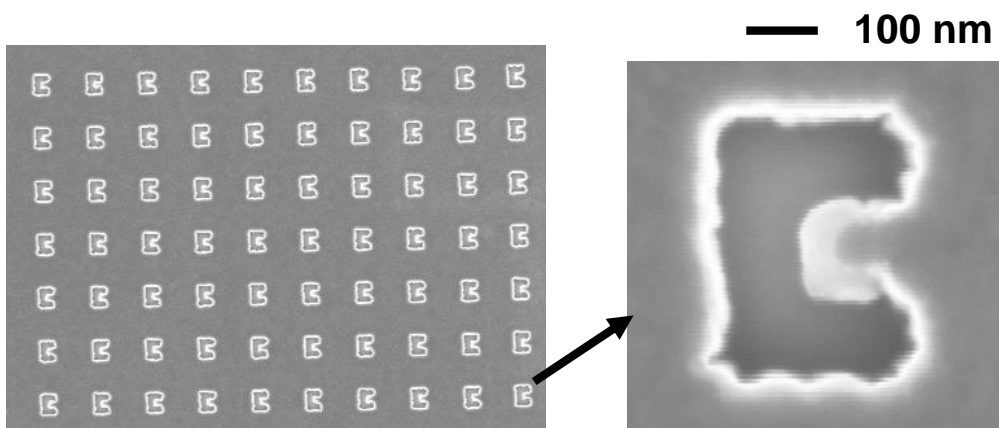
Figure 4.7: SEM image of the fabricated C-shaped nano-apertures

In one configuration, the transmitted light does not pass through FePt and is called the "no FePt" configuration; the other configuration was used to observe the effect of FePt on the transmission spectra. Light from a white light source (NKT Photonics Ltd.) was shone onto the array of nano-apertures with and without magnetic material in the near-field. The output beam of the white light source contained a broad spectrum ranging from 500 nm to 2000 nm with a maximum total average output power more than 100 mW. In order to obtain broadband transmission spectra, the transmitted light was collected in an optical spectrum analyzer (Agilent 8614A) using a lensed fiber.
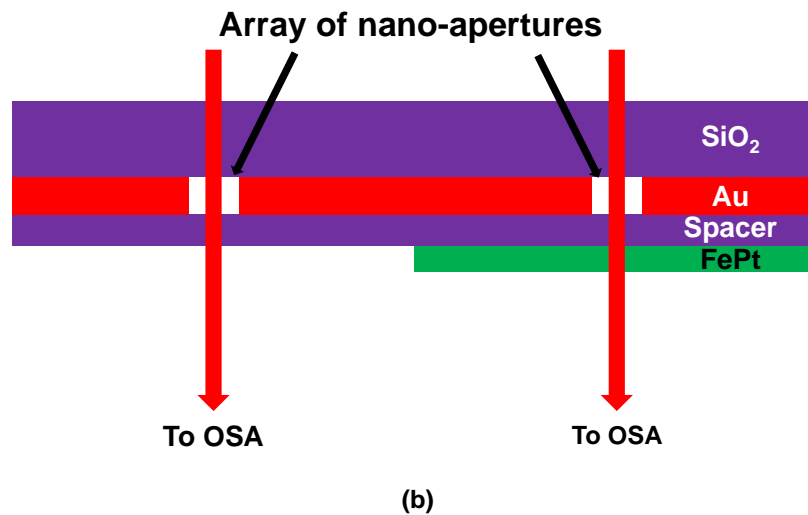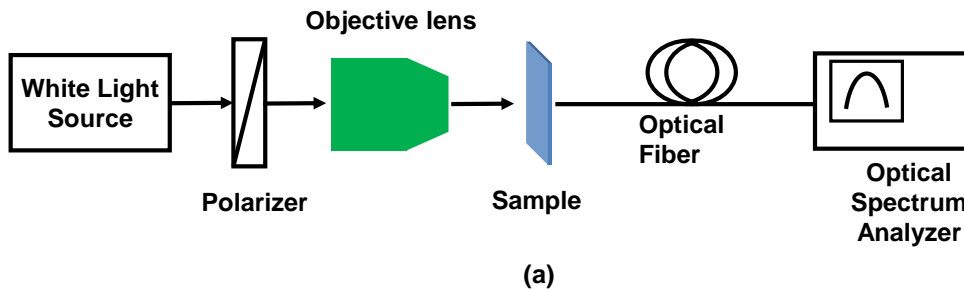
Figure 4.8: The experimental setup including: (a) the free-space optical setup used to measure the transmission spectra (b) different measurement configurations to include and exclude effect of the media

The transmission spectra for both configurations, i.e., with and without the magnetic material, are shown in Figure 4.9. The same type of blue shift in the resonant wavelength can be seen from these results and is correlated with the simulation results shown in section 4.4.1. The shift in the resonant wavelength corresponds to the thickness of the magnetic medium. The C-apertures were designed for a resonant wavelength of 1000 nm and the slight variations in the results result from the variations in the aperture dimensions during the fabrication process. Experimental measurements were taken in the far-field instead of the near-field because when a measurement apparatus is placed in the near field, it may cause the field, which was intended to be measured, to be altered. Because the purpose of these experiments was to study the effect of FePt in the near field, this was observed directly; as the FePt medium disturbs the near-field, the far- field power measured is altered.
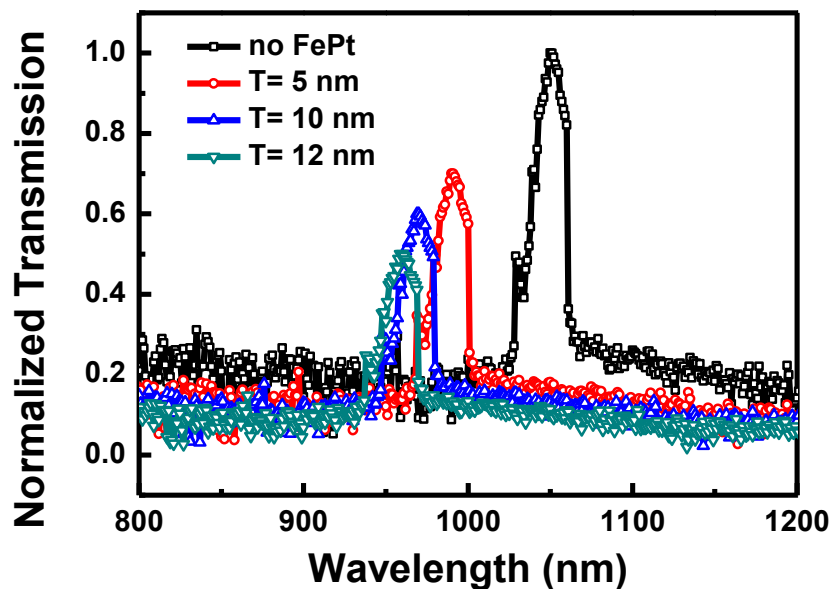
Figure 4.9: Measured transmission spectra through C-apertures for different FePt thicknesses. A significant shift in the resonant wavelength can be seen which validates the simulation results.

76

Thus it was better to study the transmission spectra in the near-field with FDTD simulation, the results of which are shown in Figure 4.5. As previously mentioned, the NFT may not show the same resonance condition when in close proximity to FePt as compared to the resonance it shows in free space or other recording media, and thus may perform poorly in a HAMR application if it is only optimized for free space transmission. This is the most serious implication of the resonance shift for HAMR application.

Figure 4.10 shows results for a re-optimization process for the C-aperture. As mentioned previously, the resonant wavelength of a C-aperture depends upon its arm length; so the arm length dimensions have to be optimized in the presence of a storage medium in order to again operate the C-aperture on resonance. From the simulation results shown in Figure 4.10, it can be seen that the C-aperture arm length is different when optimized with and without the storage medium,
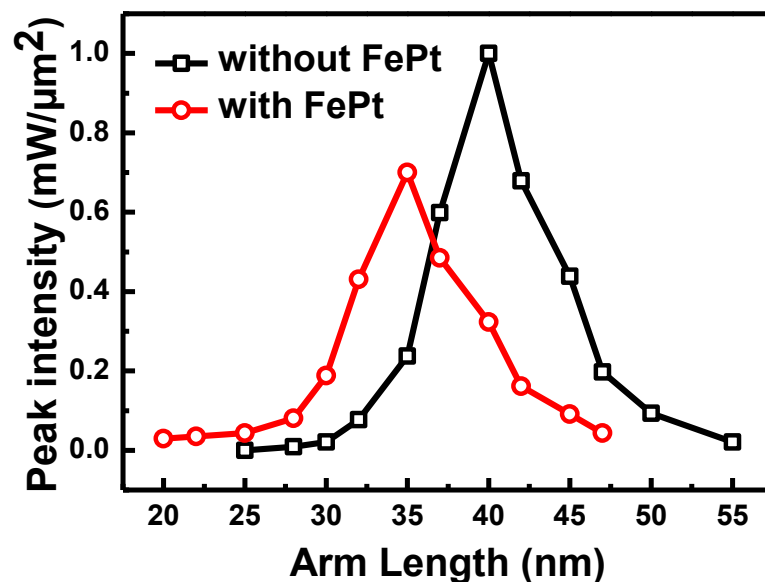
Figure 4.10: Plot of the near-field peak intensity versus the "arm" length (simulated)

showing the effect of the magnetic storage medium on the transmission characteristics in the near-field. The results were normalized by the maximum value achieved without FePt. The resonant wavelength is directly proportional to arm length to achieve maximum near-field intensity and a change in arm length value corresponds to a shift in the resonant wavelength. The coupling of (near-field) electric fields from the NFT to the magnetic medium is different in case of a BPM from a thin-film recording medium [73, 112]. In the case of BPM, the coupling of electric field from an NFT would be better and there will be less reflected field from the magnetic medium back to the NFT which would cause only a small effect on the surface field distribution but greater effect on the plasmonic resonance. Since the resonant transmission of a C-aperture depends on both factors (plasmonic resonance and surface charge distribution), the resonant wavelength is expected to be affected less severely by BPM compared to the thin magnetic film.

4.5. Summary and Conclusions

In summary, a detailed analysis by simulation and experiment was performed in order to observe the effect of a magnetic medium on the performance of the C-aperture, which is a strong candidate as an NFT for HAMR applications. A magnetic medium has a strong effect on the performance of nano-apertures when brought into the near-field of a nano-aperture. FePt is a strong candidate for a storage medium for HAMR application due to its high coercivity and moderate Curie temperature. FePt strongly affects the resonant behavior of nano-apertures and any nano-aperture designed to operate at a particular resonance in isolation will not operate on resonance when it comes in close

proximity to FePt. The NFT is required to operate on its resonant wavelength in order to deliver maximum near-field intensity to the storage medium and a C-aperture not performing on resonance would be a poor near-field transducer for a HAMR system. The resonant wavelength of a C-aperture is controlled mainly by its dimensions. Results have shown that C-apertures have different geometrical dimensions when optimized for maximum near field intensity in isolation and with FePt in close proximity. The optical spot size and the near-field intensity from a nano-aperture also strongly depend on flying height and a flying height less than 5 nm enhances the performance of an NFT significantly. In order to design a light delivery system, it is necessary to have sufficient power density required to heat the magnetic media above Curie temperature. A detailed power requirement analysis is thus required to characterize HAMR with nano-apertures. This is the subject of the next chapter.

Chapter 5

Heat Assisted Magnetic Recording Analysis

This chapter presents HAMR testing and parameters affecting the performance of HAMR. Fabrication of a magnetic storage medium used in HAMR experiments is described first following by analysis of its magnetic and optical properties, which were performed using a VSM and a UV-Visible Spectrophotometer. The analysis of the optical properties is helpful in determining the preferred wavelength for HAMR applications. Next, a pump-probe optical setup is described in detail and is used to measure the power density required for HAMR. The setup measures the B-H loop (hysteresis loop) of the magnetic medium and the reduction in coercivity which depends on the laser power incident on the medium. The performance of HAMR is analyzed under a few varying parameters such as HAMR laser power and polarization orientation of the incident laser beam. As discussed previously, the C-aperture is a strong candidate for an NFT; HAMR is demonstrated using C-apertures at the end of this chapter and the performance of square apertures and C-apertures is compared.

5.1. Optical Characteristics of Thin Film FePt

The absorption characteristics of a magnetic medium are very important for HAMR writing because they determine the power absorption efficiency of the magnetic medium. In this section transmission and reflection characteristics of thin film FePt, deposited on a glass substrate, are measured. A UV-Visible spectrophotometer (Solid 3700, Shimadzu) was used to measure the

transmission and reflection spectra of a thin film FePt film deposited on a glass substrate. The spectrophotometer consists of a monochromator, white light source and reflecting mirrors. The sample is irradiated by a single wavelength light generated by the monochromator. The spectrophotometer can generate wavelengths ranging from 240-1600 nm. Integrating sphere detectors are used to collect the light transmitted through the sample.

Measured transmission and reflection spectra are shown in Figure 5.1. The measurements were performed for different thicknesses of FePt. The transmission decreases as the thickness increases and the reflection increases with the thickness. The results show that there was no peak found for transmission and reflection characteristics. This shows the absorption of the thin film FePt is unchanged for a wide range of wavelengths and there was no peak or dip observed in the results. This shows that the wavelength choice for HAMR application mainly depends upon the availability and cost of the laser source. For these experiments a wavelength of 850 nm was chosen because 850-nm VCSELs are easy to fabricate and characterize compared to shorter or longer wavelength VCSELs.

(a)   (b)
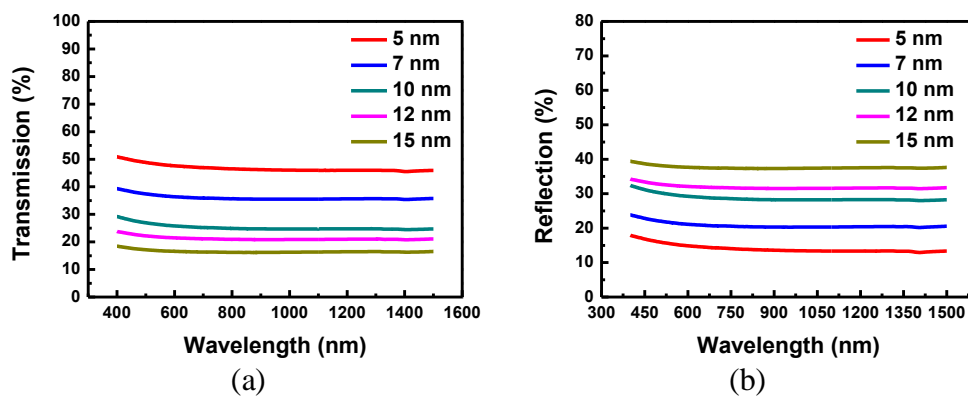
Figure 5.1: Transmission characteristics of FePt thin film, deposited on a glass substrate. (a) Transmission spectra and, (b) reflection spectra

5.2. Magnetic Storage Stack

$L1_0$ FePt was used as the storage medium in this thesis because of its ability to exhibit high coercivity and moderate Curie temperature. The structure of the storage medium stack used in all the experiments performed in this thesis is shown in Figure 5.2. The storage stack was prepared in a sputtering system having a chamber pressure of $\sim 5 \times 10^{-9}$ Torr. The thicknesses of the CrRu and MgO layers were 24 nm and 3 nm respectively, and were deposited on a 0.5-mm thick glass substrate. A 10-nm thick FePt film was deposited on these pre-deposited underlayers. The CrRu layer was deposited at 400 °C; it was used to provide a (002) texture for the heteroepitaxial growth of (001) FePt. Following CrRu deposition, a MgO layer was deposited at the same temperature. The MgO layer was used as a buffer layer between the CrRu and FePt to prevent diffusion of Cr into the magnetic recording layer. The final step was deposition of the FePt layer at a higher temperature of 600 °C. The sputtering conditions used for magnetic samples fabrication were based on previous work [113, 114].

FePt	10 nm
MgO	3 nm
CrRu	24 nm
Glass Substrate	0.5 mm

Figure 5.2: The magnetic media structure, showing all the underlayers

82

The storage medium stack was prepared in a mixture of Ar-He (0.5% He by volume) gases at elevated temperatures. The coercivity of the media was controlled by varying the process parameters. Media samples with different coercivities were hence prepared for these experiments; this same storage stack shown in Figure 5.2, however, applies to all the experiments performed in this chapter. Magnetic samples prepared for the experiments to be performed in Sections 5.3 and 5.4 have the same structure with a coercivity of ~ 3 kOe, whereas the samples prepared for Sections 5.5, 5.6 and 5.7 have a coercivity of ~ 8 kOe, with the same structure mentioned in this section. All storage samples used 10-nm thick FePt as magnetic layer.

5.3. Curie Temperature Measurements

The Curie temperature is an important parameter for a magnetic medium because it determines the power required for HAMR. The Curie temperature of the magnetic medium (used in the following experiments with having different room temperature coercivities) is measured in this section. A storage sample with ~ 3 kOe coercivity was prepared for this experiment. The magnetic medium was FePt with a 10-nm thickness. High temperature VSM measurements were performed to study the Curie temperature of the magnetic medium. In-plane B-H loops were measured instead of out-of plane loops due to restrictions of the sample holder in the VSM. The temperature range used was 30 ^{o}C to 450 ^{o}C (300 K to 723 K). The results are shown in Figure 5.3. It can be seen from the results that magnetic medium coercivity, shown by the span of the B-H loops, is reduced with increasing temperature of the medium and at a particular temperature, the B-H loops no longer show hysteresis.
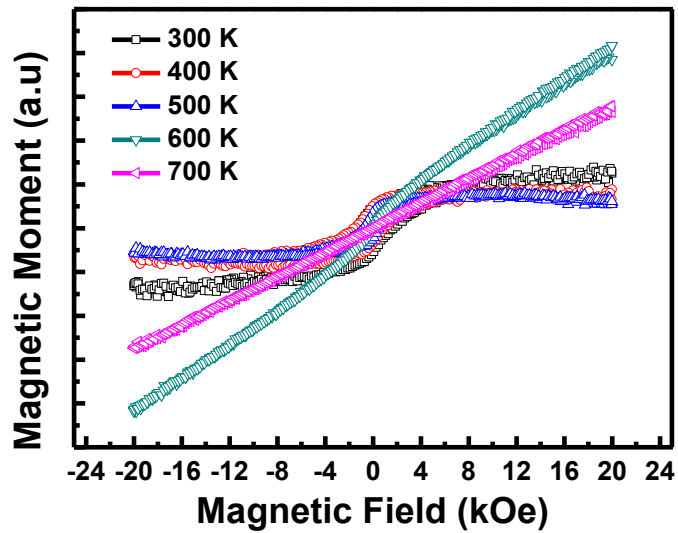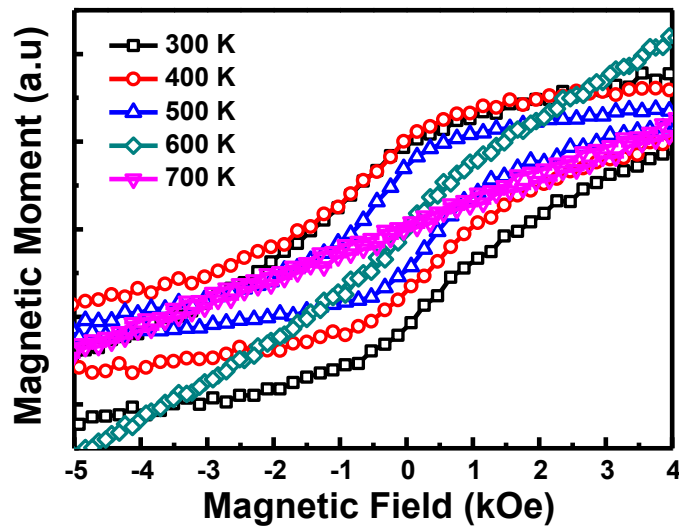
Figure 5.3: (a) Temperature dependent B-H loops of FePt and (b) is a magnified view of the central region of (a).

This is the point where the ferromagnetic material behaves like a paramagnetic material and that temperature is called the Curie temperature. Figure 5.4 shows the variation of the coercivity (Hc) of the medium as the temperature is increased. The approximate value of the Curie temperature is ~ 425 $^{\circ}$C or 700 K.
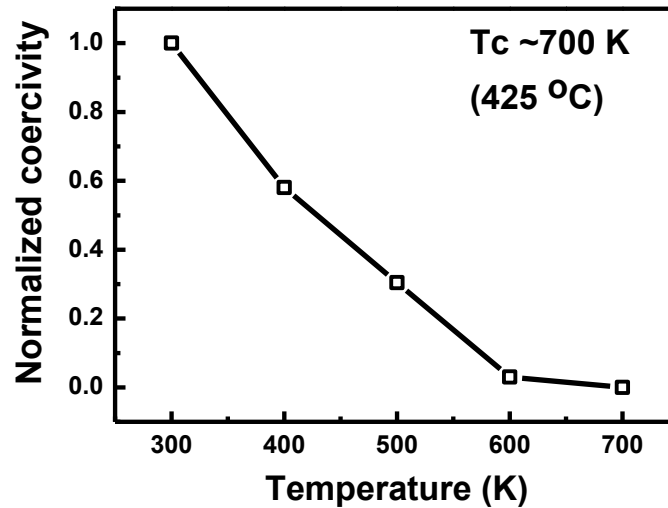
Figure 5.4: Coercivity reduction with increasing temperature

5.4. HAMR Experimental Setup and Methodology

It is required to know the power density required for HAMR before fabricating nano-aperture VCSELs. A pump-probe setup using a high power 850-nm laser, also called the "HAMR laser", was designed to observe the variations in the coercivity of the magnetic medium in order to measure the required power density for HAMR. This section thoroughly describes the setup and methods followed to demonstrate HAMR experimentally. Firstly, the components and functionality of a far-field pump-probe system is discussed. Secondly, the techniques to align the high power laser, probe laser and magnetic field are explained. The power density is calculated as the ratio of the total power over the area of the optical spot. B-H loops of the magnetic medium were measured and then the coercivity was calculated for each value of the incident power density. The section ends with an experiment which involves HAMR testing for different polarization orientations of the HAMR laser.

5.4.1. Pump-Probe Optical Setup

A pump-probe optical setup, shown in Figure 5.5, was designed in order to measure B-H loops of the magnetic media, dependent on the incident power from a high power laser and the results were later used to characterize the power density required to achieve the Curie temperature of the media. A brief description of the components used in this setup is given here, following the working principle of the setup. The list of optical components with their properties, used in the setup, is summarized in Table 5.1.

Table 5.1: Description of the components used in the pump-probe setup

Diode Laser (Pump Beam)	Output Power @ 25°C: 0 ~ 885 mW adjustable Wavelength: 850 nm Operation Mode: Continuous Wave Beam Divergence (1/e^2, Full Angle): <1.5 mrad Beam Diameter at the Aperture : ~ 3.5 mm × 3.5 mm Beam Spot Outline: Nearly Rectangular
Diode Laser (Probe Beam)	Output Power @ 25°C: 0~30 mW adjustable Wavelength: 405 nm LD Mode: Multi Mode Operation Mode: Continuous Wave Beam Spot Outline: Nearly Round
Objective Lens	Magnification: 80 X N.A: 0.5 Focal Length: 4.5 mm Working Distance: 25 mm
Linear Polarizer	Wavelength range: 550 nm – 1.5 μm Extinction ratio: >100,000:1 Wavelength range: 550 nm – 1.5 μm Extinction ratio: >100,000:1 Laser Damage Threshold: 25 W/cm² Continuous Pass Clear Aperture: Ø10.9 mm (Ø0.43")
Beam Splitter	Wavelength Range: 400 – 700 nm Split Ratio: 50:50 Non polarizing 10 mm cube
Electromagnet	Maximum current rating for safe operation: 3 A Maximum magnetic field with minimum enough spacing for the sample holder; using solid pole: 1.5 T Maximum magnetic field with hollow pole: 0.4 T
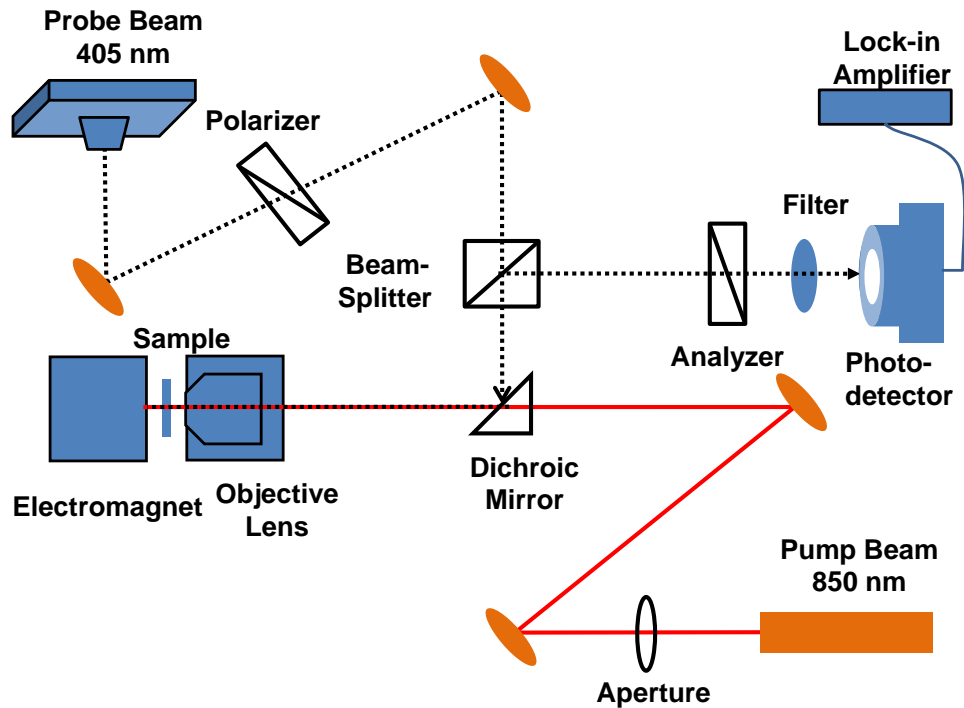
Figure 5.5: The pump-probe optical setup used to measure the irradiance dependent B-H loops of FePt

Other optical components are mirrors, a translation stage, a photo-detector and a lock-in amplifier. The optical setup consists of two configurations; one uses the probe laser to measure a BH curve by measuring the reflective signal from the sample and the other one mainly consists of the pump laser which was aligned with the probe laser and was used to heat the media to elevated temperatures. A laser beam from the probe laser passes through the linear polarizer and is focused on the sample; the sample can be placed on a sample holder, between the two magnetic poles. The electromagnet is then used to apply a magnetic field to achieve magnetic rotation in the media. The polarization of the reflected beam is rotated because of magnetic rotation in the sample, also called Kerr rotation. Kerr rotation was measured by the photo-detector and the signal is sent to a lock-in amplifier which can be used
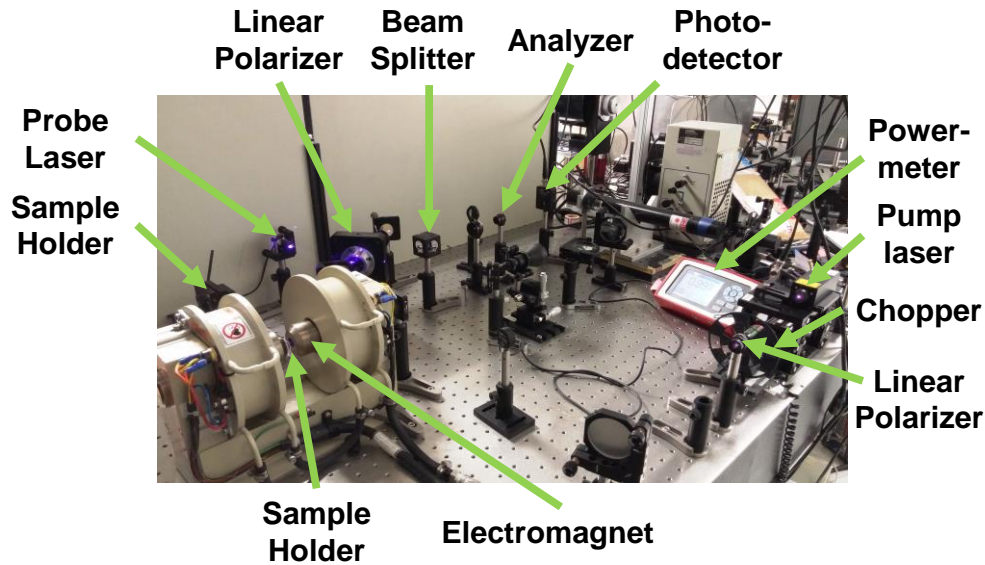
Figure 5.6: Pump-probe setup

to plot the B-H loop of the medium. The main challenge in this setup is alignment of the pump and probe lasers. The optical spot of the probe laser was much smaller than the pump laser. This was necessary in order to observe the heating effect on the Kerr rotation. Figure 5.6 shows images of the probe-pump optical setup. A commercial media (CoCrPt) magnetic disk sample with a coercivity of 5 kOe was used as a reference in order to calibrate the magnetic field produced by the electromagnet.

An example of measured B-H loops of FePt and commercial media samples is shown in Figure 5.7. Since the coercivity of commercial media was known, it was used to calibrate the coercivity of any other medium whose coercivity was not known. For HAMR experiments, pump and probe lasers are required to be aligned in a way that probe laser can read the Kerr rotation of the magnetic media, assisted by the pump laser. Figure 5.8 shows alignment of the two lasers.
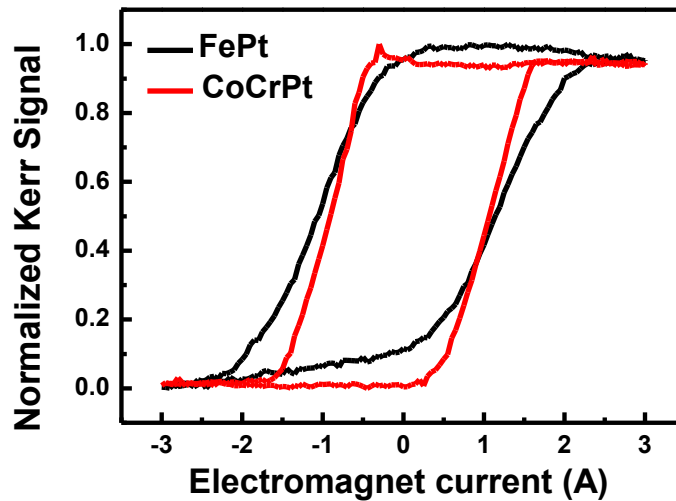
Figure 5.7: B-H loops of FePt and commercial media sample using pump-probe optical setup
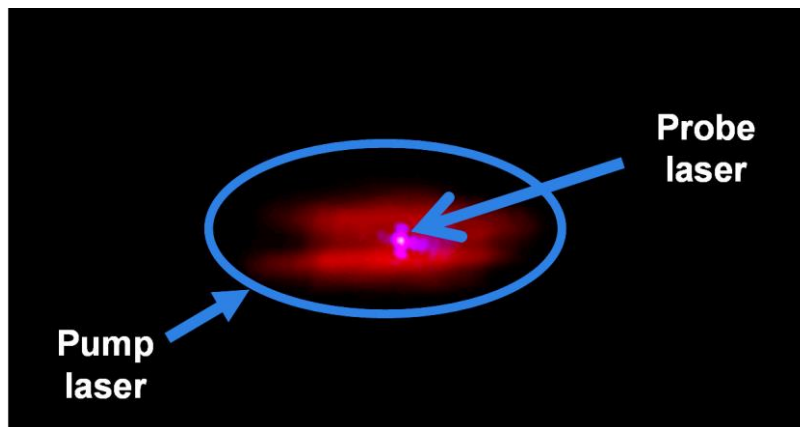
Figure 5.8: The alignment of the pump and probe lasers.

5.4.2. Temperature Dependent Change in Coercivity of The Magnetic Medium

This section describes the analysis performed to find the power density required to heat the magnetic medium (i.e., 10-nm FePt) to its Curie temperature. A storage sample (described in Section 5.2) with a coercivity of 3 kOe was prepared for this experiment. The coercivity value was chosen due to the limitations of the magnetic field provided by the electromagnet used in this

setup. HAMR experiments were performed with the HAMR laser described in Section 5.4.1. A Si photo-detector equipped with a power meter was used to measure the power incident onto the magnetic material. The power was measured after the objective lens (incident power on the sample was focused by the objective lens). The diameter of the optical spot size on the magnetic medium was measured to be 5 μm. This was done to make sure that all the optical losses of the optical components could be taken into consideration. A set of B-H loops for different values of pump power was measured and is shown in Figure 5.9. It can be seen from the results that the B-H loop of the medium strongly depends on the pump laser power. The rate of change in coercivity reduces as the coercivity approaches zero. The power required to raise the temperature of the medium above its Curie temperature was estimated to be 27 mW. However, it is the power density which is more important than the absolute power. The power density is calculated as the total incident power divided by the total exposed area and the results are shown in
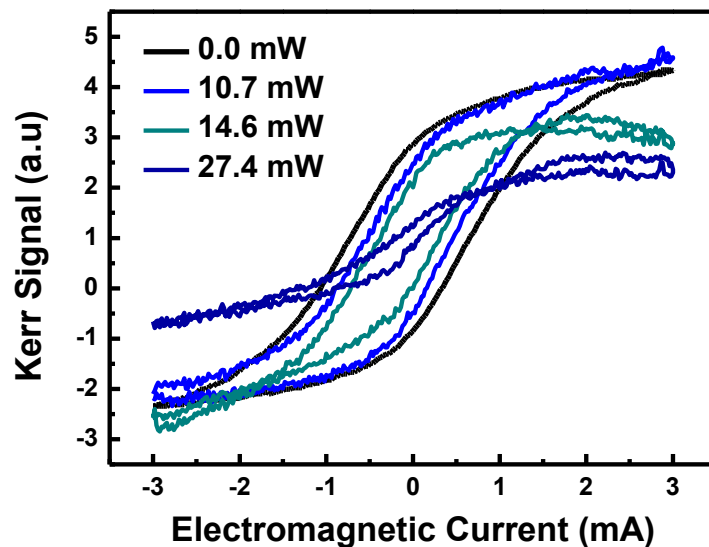
Figure 5.9: The dependence of B-H loops of FePt on the incident laser power
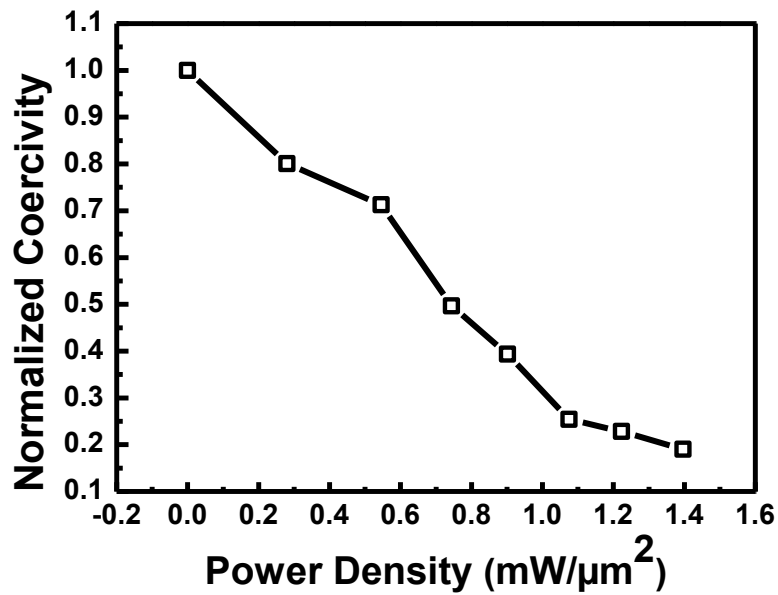
Figure 5.10: The curve shows the reduction of the FePt coercivity with the incident power density

Figure 5.10. The results show that a power density of 1.4 mW/µm^2 was enough to heat the magnetic medium above its Curie temperature. For this power density, the coercivity was ~ 15 – 20% of its value at room temperature, and magnetization rotation could be achieved by applying a magnetic field equal to the field available from the conventional write head.

5.4.3. Effect of Polarization Orientation

Polarization orientation of the incident light is very important for the performance of an NFT [97]. This section describes experiments performed to investigate any benefit from the polarization orientation in the magnetic reversal during the HAMR process.

A continuous wave 850-nm laser signal, with different polarization orientations was used to observe the change in coercivity and the results are shown in Figure 5.11. Results for linear polarization (LP), right handed circular polarization (RCP) and left handed circular polarization (LCP) were

investigated. A linear polarizer was used to get linearly polarization beam and the orientation of the axis of polarization was controlled by the polarizer. The axis was rotated against the sample position and readings were taken for a fixed incident HAMR power and results showed that the all orientations produced same change in the coercivity of the magnetic medium. That helped to choose one fixed orientation angle to perform measurements for circularly polarized beam. A quarter wave plate was used to convert linear polarization to circular polarization. RCP is the circular polarization when the quarter wave plate was at +45 with respect to the linear polarizer and -45 referres to LCP polarization. The quarter wave plate was rotated 90° from +45 position to achieve -45 position. And the results were same for both positions. This shows there is no difference in the results regardless of the polarization orientation of the HAMR laser. It can be seen from the results that coercivity of the magnetic medium had the same dependence on the power of the incident laser regardless of the polarization orientation.
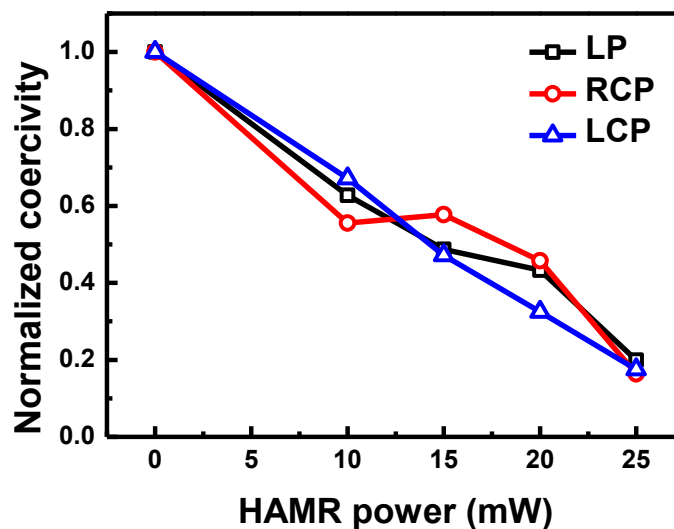
Figure 5.11: Dependence of coercivity of the media on laser power having different polarization orientations.

5.5. HAMR using High Coercivity Medium

A low coercivity FePt magnetic medium was used in the last section due to the electromagnet limits described, and the power density required for HAMR was found. In this section the magnetic medium had a coercivity of ~ 8 kOe, which is higher than the magnetic medium used earlier. However, both media have the same Curie temperature and it is expected that the same power density be required to heat the medium to its Curie temperature. This section demonstrates HAMR in a high coercivity medium using a power density of 1.4 mW/μm^2, which was calculated in Section 5.4.2.

Figure 5.12 shows the experimental setup used for HAMR demonstration in this section. The HAMR laser was focused on the magnetic medium through an objective lens. The incident power density was 1.4 mW/μm^2, which, according to the earlier results would be enough to heat the magnetic medium to its Curie temperature. A high magnetic field was applied on the sample to saturate the magnetic domains in one direction before the HAMR writing. The laser light transmitted through the objective lens was focused on the magnetic medium and the magnetic medium was heated above its Curie temperature to reduce its coercivity. A magnetic field of ~ 3 kOe and oriented opposite to that of the existing magnetic domains in the sample was applied by an electromagnet to obtain magnetic reversal at the elevated temperatures. The Kerr microscope and MFM were used for magnetic imaging and the results are shown in Figure 5.13. The laser beam was linearly scanned on the magnetic sample which formed magnetic lines and were visible in the Kerr microscopic image. The black lines in Figure 5.13 (a) show the area which was illuminated
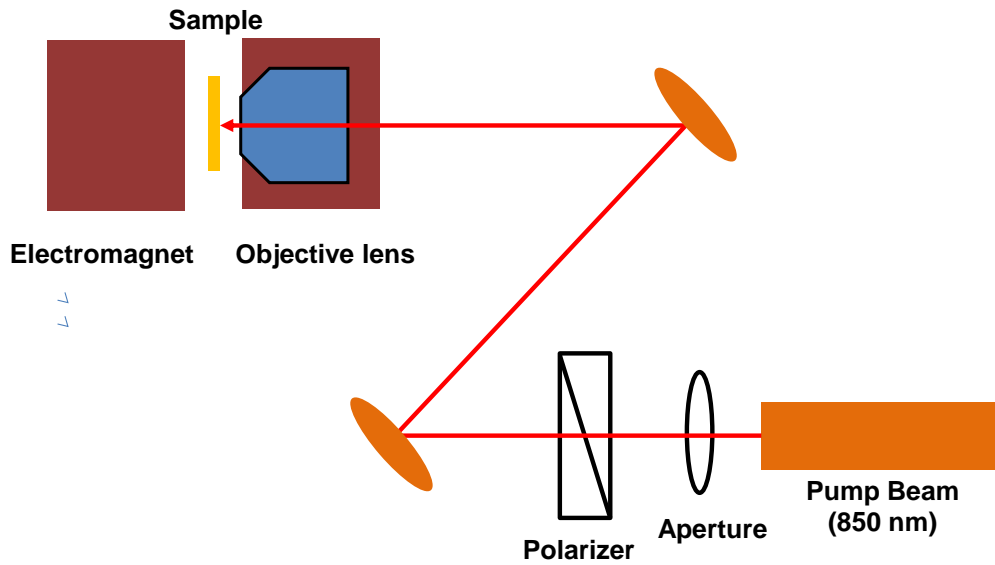
Figure 5.12: The optical setup used for HAMR demonstration
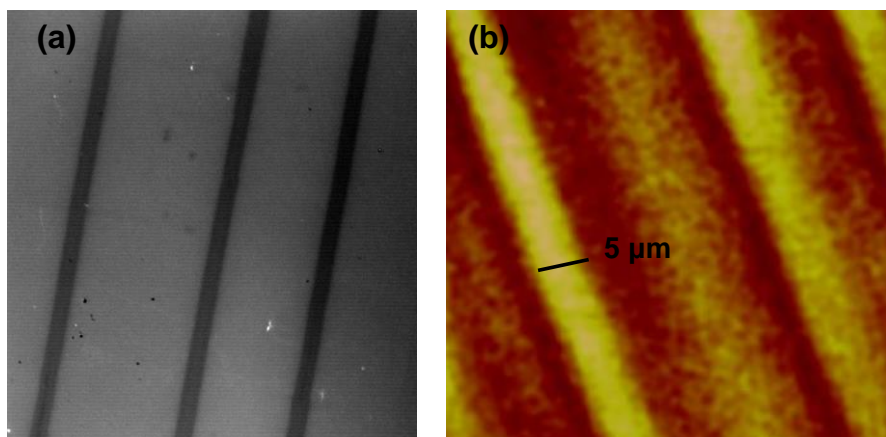
Figure 5.13: (a) A Kerr-microscopic image showing the area illuminated by the HAMR laser. The domains in the black lines have a magnetic orientation opposite to that of the other areas on the sample (b) MFM image of the same lines

by the laser and their contrast shows the achieved magnetic reversal under HAMR conditions. The width of the line is equal to the optical spot of the laser beam. These experiments confirmed that the same power density (i.e., 1.4 mW/µm^2) can be used for the high coercivity magnetic media. The next section describes HAMR demonstration for high coercivity magnetic medium (~ 8 kOe) through square and C apertures using near-field focusing.

5.6. HAMR Through Apertures

High areal density storage HAMR writing requires the laser light to be focused on a very small area. Simulations were performed in Chapter 3 to compare transmission characteristics of square apertures and C-apertures for HAMR. This section compares the performance of square apertures and C-apertures as an NFT for HAMR, by demonstrating HAMR using square and C-apertures. Magnetic storage samples using 10-nm FePt with a coercivity of ~ 8 kOe, having the stack structure described in Section 5.2, were prepared for these experiments and were saturated using a high magnetic field before HAMR. A schematic is shown in Figure 5.14.

A 500 µm × 500 µm array of square apertures was fabricated in 100-nm thick Au, shown by white spaces in the figure, deposited on a glass substrate. The sample with square apertures was pasted over the magnetic sample and placed on the sample holder in a direction shown in Figure 5.14. The HAMR laser (with a power density of ~ 1.4 mW/µm^2) was focused on the square apertures. The laser light transmitted through the square apertures was focused on the magnetic medium and raised its temperature above its Curie temperature to
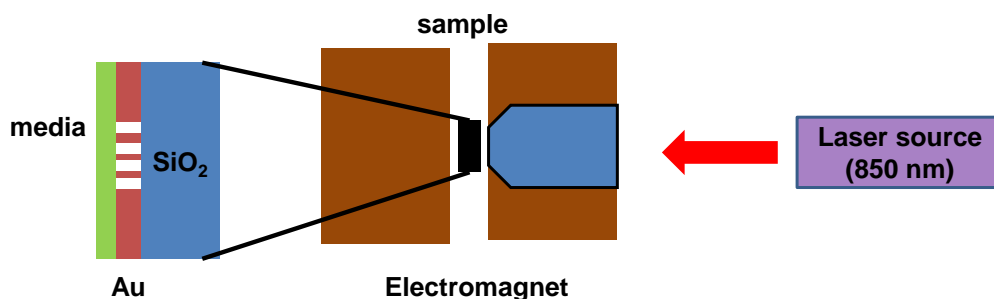
Figure 5.14: The experimental setup for HAMR through apertures.

reduce its coercivity. A magnetic field, with magnitude ~ 3 kOe was applied by an electromagnet to obtain the magnetic reversal at the elevated temperatures. Figure 5.15 shows Kerr microscopic and MFM images. The width of the square apertures was reduced gradually in order to achieve a smaller optical spot while keeping the incident power density constant. Transmitted power density remained unchanged as the aperture width was reduced and sufficient power was transmitted through the apertures to achieve magnetic reversal, till the width was equal or less than 1 µm. The transmitted power density through square apertures decreased greatly for a square aperture of size 1 μm^2 or less because the size is comparable to the wavelength of the incident laser beam. The apertures equal to and less than 1 μm^2 were not able to achieve magnetic reversal for the same incident power density.

(a)

(b)
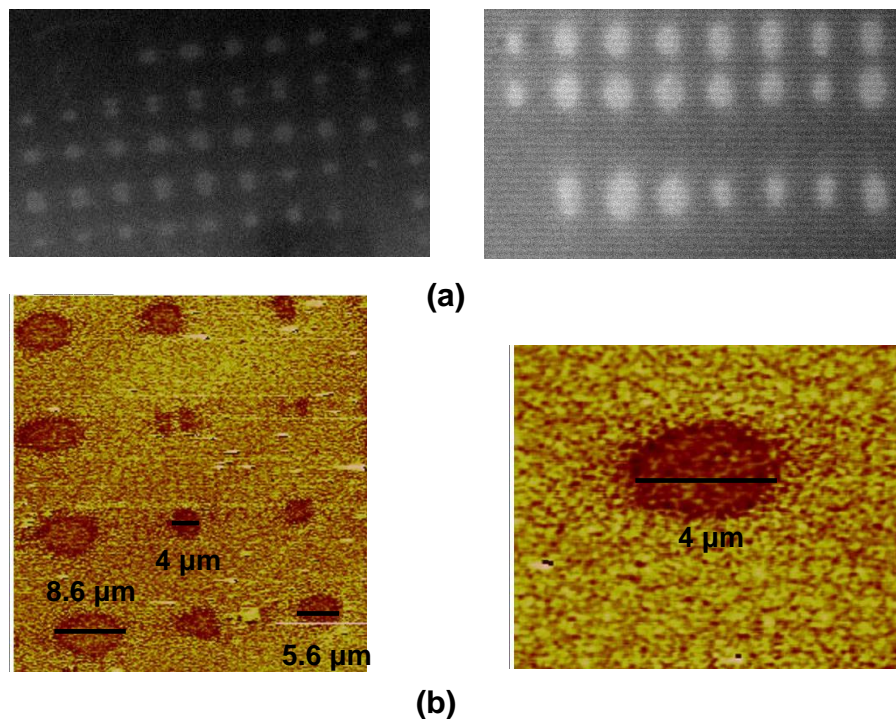
Figure 5.15: Magnetic bits achieved using square apertures of different size using HAMR. (a) Kerr microscopic and (b) MFM images of the magnetic bits achieved.

96

The results show that square apertures are very poor NFTs to be used in HAMR. As mentioned in chapter 3, a C-aperture provides higher near-field intensity compared to a square aperture and is a strong candidate for an NFT; the next section demonstrates HAMR using C-apertures.

5.6.1. HAMR using C-apertures

This section compares the performance of square apertures and C-apertures to achieve magnetic bits of size on the order of 1 µm. The same magnetic sample and experimental setup from last Section was used for this experiment. A schematic of the C-apertures is shown in Figure 5.16 with dimensions $\ell = 1.6$ µm, $\alpha = 1$ µm and $L = 3\alpha = 3$ µm. The circle shows the region where the transmitted signal through the C-aperture is focused on the magnetic medium. Alternating arrays of square and C-apertures were fabricated over a 700 µm × 700 µm area. The pattern design is shown in Figure 5.17. The vertical lines were used as markers to facilitate MFM imaging. The incident laser beam was linearly polarized in the X direction with a power density of 1.4 mW/µm^2.
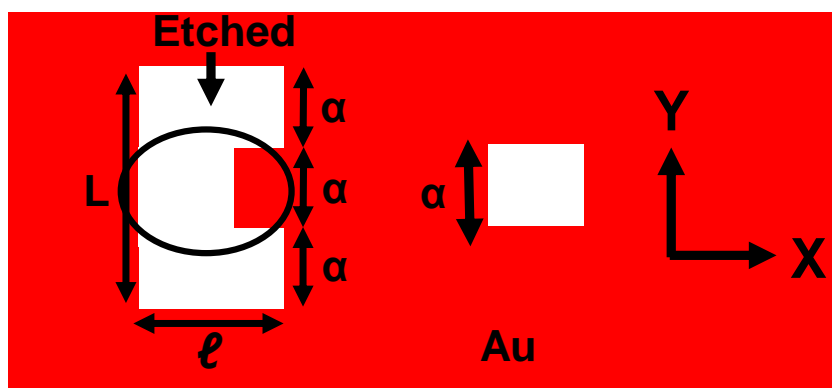
Figure 5.16: C-aperture and square aperture used for HAMR demonstration
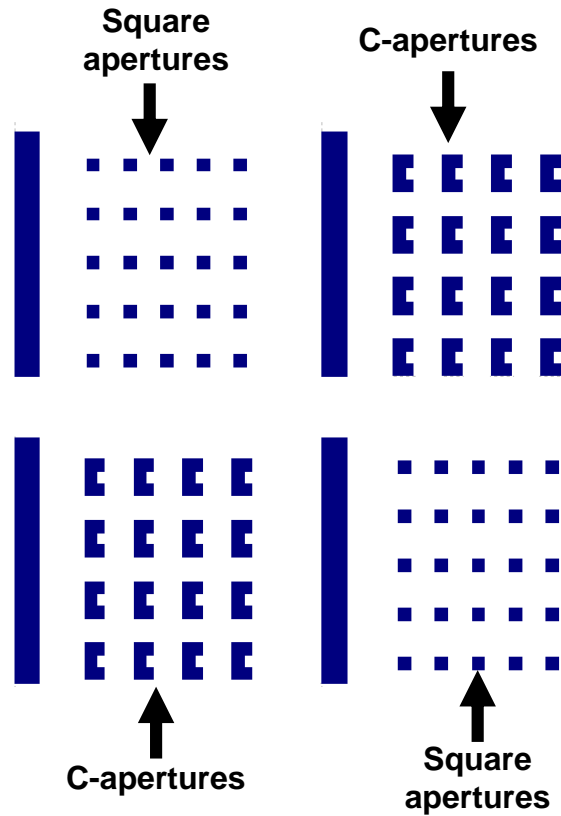
Figure 5.17: Mask design showing alternating arrays of square and C-apertures

The power is transmitted through the apertures and is focused on the magnetic medium which is heated to its Curie temperature and a magnetic field ~ 3 kOe is used to achieve magnetic reversal. Magnetic imaging was performed using a Kerr microscope and the results are shown in Figure 5.18. The black circles in the image are the magnetic bits achieved. It can be seen that the C-apertures were able to obtain magnetic reversal whereas square apertures were not. The reason is the enhanced transmitted power density through C-apertures compared to that of the square apertures. The reason for the enhanced power density through C-apertures is the localized plasmonic effect produced along the Au part of the C-aperture, also shown by a circle in Figure 5.16.
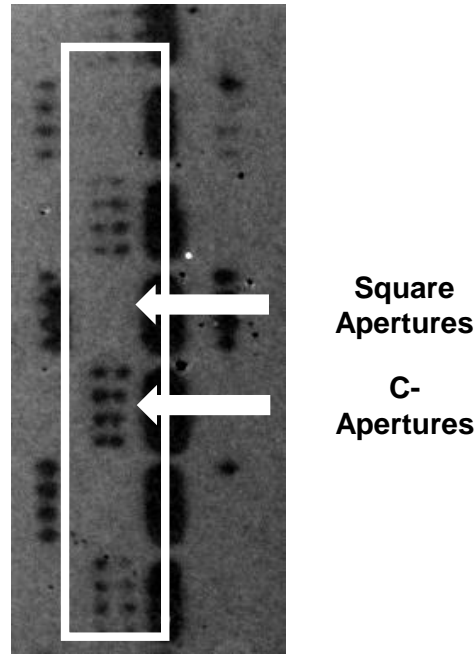
Figure 5.18: Kerr microscopic image shown the magnetic reversal obtained by C-apertures

MFM was used to measure the size of the magnetic bits produced by the C-apertures. It can be seen in Figure 5.19, that a single elliptical magnetic bit was produced in the magnetic medium. The transmitted power is localized in the center of a C-aperture resulting in a single magnetic bit. The size of the magnetic bit is ~ 1 μm in the Y direction and ~ 1.2 μm in the X direction with an area of ~ 3.76 μm^2. The results strongly suggest that a C-aperture can be used as an NFT in HAMR. The size of the magnetic area switched depends upon the size of the aperture. Since the optical spot produced by the incident beam was controlled manually, that can result in variation in the incident power density and thus would result in higher or lower transmitted power densities, demonstrated by the different sized bits produced. It is required to produce even smaller bits for higher areal density requirements.
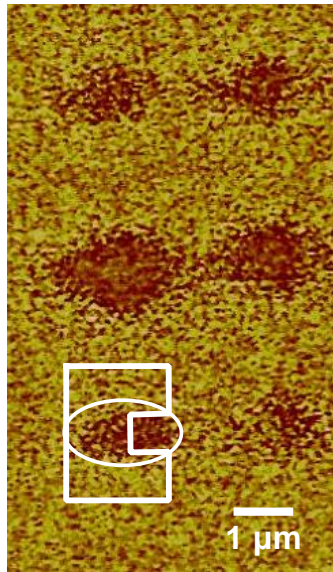
Figure 5.19: MFM image shows the magnetic spot produced by the C-apertures

The bit size can be controlled by reducing the aperture size. Differently sized C-apertures were used to achieve magnetic bits of different sizes. C1 and C2 both are C-apertures with aperture sizes of 1 µm and 500 nm, respectively.

(a)   **(b)**
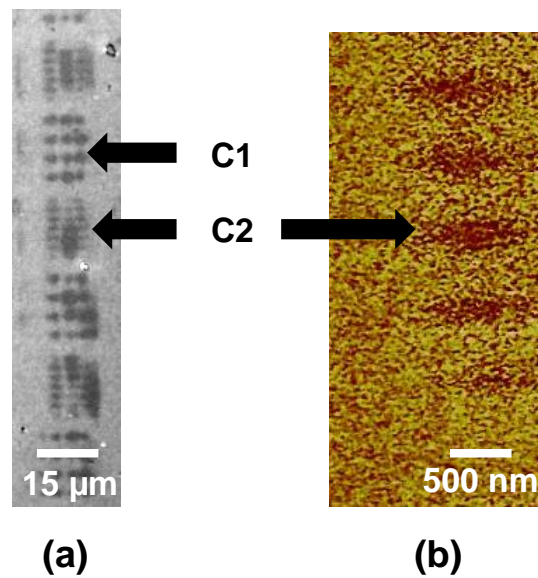
Figure 5.20: Different sized bits can be achieved using C-apertures with different aperture sizes. Magnetic bits achieved by two differently sized C-apertures can be seen by (a) Kerr microscopic image, and (b) MFM image

It can be seen from Kerr microscopic and MFM images, shown in Figure 5.20, that smaller bits can be achieved using smaller apertures. Both C1 and C2 apertures produced magnetic bits of different sizes. The magnetic bits produced are, again, elliptical.

The power transmitted through square apertures reduces quadrically as the size of the aperture is reduced, as can be seen by the following equation:

$$\text{Power Throughput (PT)} = \frac{\text{Power}_{transmitted}}{\text{Power}_{incident}} \propto \left(\frac{\alpha}{\lambda}\right)^4 \qquad \text{Eq. 5.1}$$

where α is diameter of the square aperture. Whereas the area of the square aperture changes quadrically with the diameter:

$$\text{Area of a square aperture} \propto (\alpha)^2 \qquad \text{Eq. 5.2}$$

Thus the power density transmitted through a square aperture changes quadrically. This suggests that in order to achieve smaller bits using a square aperture, the required incident power density would also change exponentially.

Whereas in the case of C-apertures, experimental results show that when the aperture size is reduced from 1 µm to 500 nm, the required power density increases by only a factor of ~ 1.33. To achieve 500 nm bits, the required incident power density is only 33% higher than that which is needed to achieve 1-µm bits, using C-apertures.

5.7. Summary and Conclusions

In this chapter, a pump-probe optical setup was designed to characterize power requirements for HAMR using an FePt magnetic medium. An optical analysis of thin film FePt showed that the transmission and reflection characteristics of

FePt are independent of the wavelength of the incident laser beam. An 850-nm high power laser was used to measure the power density required to heat the magnetic medium above its Curie temperature. Coercivity calculations showed that the required power density for HAMR is 1.4 mW/μm^2. Results showed that the polarization orientation of the pump laser does not assist in reduction of coercivity of the magnetic medium.

HAMR was demonstrated using square apertures and C-apertures and it was found that a square aperture with a width equal to or less than the HAMR laser wavelength (i.e., < 1 μm) has very low power transmission and was unable to heat the magnetic medium to a temperature at which magnetic reversal can be achieved, whereas the C-apertures demonstrated HAMR successfully at sizes even smaller than 1 μm. The C-apertures showed a higher transmitted power density due to the larger total area and a surface plasmon effect. The transmitted power was localized in the center of the C-apertures which results in a single optical spot and an elliptical magnetic bit.

The direct light delivery system requires the fabrication of a high power laser and integration of an NFT which can produce a localized optical spot using light from the laser source. The following chapter discusses nano-aperture VCSEL fabrication and characterization for HAMR.

Chapter 6

Nano-aperture Vertical Cavity Surface

Emitting Lasers (VCSELs)

Semiconductor lasers are potential candidates to be used as a laser source in the direct light delivery system, proposed in this thesis. VCSELs have become a more attractive choice for systems that require semiconductor lasers since they offer many advantages over edge-emitting lasers. The biggest advantage of VCSELs over edge-emitting lasers is the ability to perform simple testing, although their fabrication includes difficult epitaxial growth processes. The advantages of on-wafer testing prior to dicing and packaging result in much lower cost. Also, more devices can be yielded per wafer due to the compact size of VCSELs (typically $400 \times 400 \ \mu m^2$) [115].

Other advantages that VCSELs offer include narrow beam divergence, low power consumption, high modulation bandwidth, easy polarization control and low threshold current. VCSELs are smaller, less expensive, and easier to fabricate then edge-emitting lasers. In addition, dense two-dimensional VCSEL arrays can be fabricated on a single wafer. One-dimensional edge-emitting laser arrays are readily fabricated, but two-dimensional edge-emitting laser arrays require extensive processing and assembly. Therefore VCSELs are ideal candidates for many applications such as optical fiber communication networks, printer heads, optical sensors, barcode scanners, digital displays, spatial light modulators, backplanes and smart pixel, microscopes and optical storage [116-118].

The intention of this chapter is to discuss about the working principles of the VCSEL and at the same time give an overview of nano-aperture VCSELs. It starts with fabrication of conventional VCSELs, describes the measurement results of VCSELs fabricated in this work, and moves on to the characterization of these VCSELs. The nano-aperture VCSELs are then introduced and the near-field power densities are calculated based on the measured far-field powers, in order to compare the results with power density requirements for HAMR.

6.1. VCSEL Introduction

VCSELs were first proposed and experimentally demonstrated by Japanese scientists in late 1970s at the Tokyo Institute of Technology, Japan [119]. VCSELs contain a light emitting layer (i.e., thin semiconductor layer such as quantum wells (QWs)), called the active layer, sandwiched between two highly reflective mirrors. The mirrors are composed of dielectric layers or epitaxially grown distributed Bragg reflectors (DBRs) with a reflectivity of more than 99.9%. Light is emitted from the active layer and is ultimately normally emitted from the surface of the top mirror. A VCSEL should have (1) an extremely small cavity volume, (2) high optical gain, and (3) mirrors with extremely high reflectivity (>95%), in order to realize low threshold current. At that time it was a challenge to obtain high optical gain materials and such high reflectivity mirrors. In 1979 [119], the first electrically pumped InGaAs/InP VCSEL, under pulsed operation, was successfully demonstrated at 77 K. Room temperature pulsed operation from an electrically pumped GaAs/AlGaAs VCSEL was obtained several years later. In 1988, the first

room-temperature continuous-wave (CW) device using GaAs was demonstrated. In early VCSEL structures, an Au layer was used as a p-side reflector, and the n-side mirror was a dielectric multilayered structure consisting of SiO$_2$/Si layers. In 1989, Jewell demonstrated a GaInAs VCSEL exhibiting a 1–2 mA threshold current [120].

Progress in the development of GaAs-based VCSELs continued due to the promising optical properties of GaAs-based materials and the possibility of obtaining DBR structures using epitaxial growth. DBRs successfully replaced metal-based mirrors in a very short time and was demonstrated in GaAs/AlGaAs Fabry-Perot micro-cavities. The advantages associated with GaAs-based DBRs are the following: (1) adjacent layers have wide variation in refractive index so that high reflectivity can be achieved by using fewer layers [121] and (2) low electrical resistance can be easily achieved in DBRs by using an appropriate doping profile [122]. In addition to low loss highly reflective mirrors, VCSELs need a high optical gain active region.

High gain GaAs/AlGaAs-based QW materials were developed in the 1980s for edge-emitting lasers and they solved the problem for VCSELs too. Some researchers used GaAs/AlGaAs QWs as an active region for GaAs-based VCSELs [123, 124], while some have demonstrated that GaAs/AlGaAs QWs incorporated with epitaxial DBRs give sub-milliampere threshold current as well as CW room temperature operation [125, 126]. As mentioned before, conventional VCSELs have a top DBR, a bottom DBR and an active QW region. The top and bottom DBRs consist of many pairs of alternating semiconductor layers (of alternating refractive index) and a thickness of $\lambda/4$, with λ being the emission wavelength. For example, AlGaAs-based DBRs

have many pairs consisting one layer with high Al concentration and other with low Al concentration, which gives a small contrast between refractive indices. Figure 6.1 shows a schematic of a conventional VCSEL structure. Due to having a short cavity length, VCSEL mirrors must have high reflectivity (more than 99%). The reflectivity is typically over 99.9% for the bottom mirror and 99.5% for the top mirror.

An oxidation layer formed from an epitaxial layer of with high Aluminum concentration is buried inside the VCSEL in order to provide current and optical confinement. An oxide aperture is formed through wet oxidation of the layer in a steam environment. The layer is exposed to steam and annealed at a temperature of 350 ^{o}C to 500 ^{o}C to convert the semiconductor into a mechanically robust, chemically inert, insulating and low refractive index oxide.
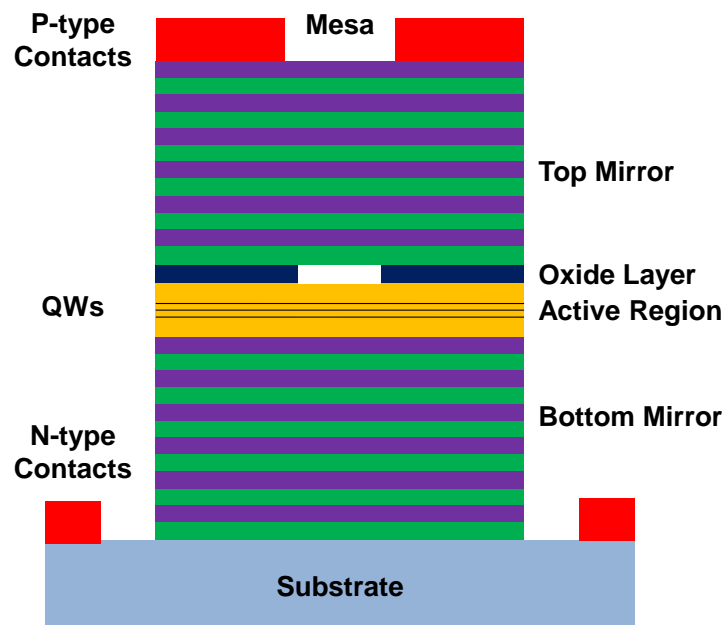
Figure 6.1: Structure of a conventional oxide aperture VCSEL

This insulating oxide aperture confines the current injected into the active region and thereby confines the optical mode around the aperture region due to the low refractive index of the oxide layer. If there were no oxidation layer, the optical mode would directly see the roughness of the etched mesa and result in a large optical loss.

The VCSELs used in this thesis are 850-nm top-emitting variety, consisting of a semi-insulating GaAs substrate, AlGaAs DBRs, each period comprising alternating composition of Al and Ga, and 3 GaAs QWs. The numbers of DBR periods are 26 and 30, each of $\lambda/4$ thickness, for the top and bottom mirrors, respectively. The top DBR is with p-type and the bottom DBR is n-type. The bottom DBR layers contain high Al content, and there is a highly Al doped layer just above the active region which is oxidized for electrical and optical confinement.

6.2. Fabrication of VCSELs

The fabrication of VCSELs was carried out in a cleanroom equipped with many fabrication tools. The fabrication steps are described in detail below:

(a) Cleaning the VCSEL Substrates

A few steps were followed to ensure that the VCSEL wafer surface was clean before starting the device fabrication. These include cleaning in acetone (10 minutes) and isopropanol (10 minutes) in an ultrasonic bath. The samples were rinsed in distilled water for 5 minutes, followed by N_2 blow-drying.

(b) P-type contact Deposition and Photolithography

Multilayered P-type contacts were deposited using electron beam evaporation. The layers contain Au/Ti layers with 300/15 nm thicknesses, respectively. A high vacuum (~ 2×10^{-6} millibar) was used in order to ensure a smooth and uniform deposition of the metal. Photolithography was used to define VCSEL mesas of various sizes. Negative tone ma-N 2405 was used as a resist. The samples were pre-baked at 90 °C for 95 s. The exposure time was optimized after few test runs. The samples were developed in ma-D 525 for 120 s.

(c) Mesa Etching

Wet etching was used to form VCSEL mesas by etching Au, Ti, top DBR and the active region. An Au etchant and 10% HF was used to etch Au and Ti. VCSEL wafers in this thesis were obtained from Avago Technologies Singapore Pte. Ltd. These wafers contained highly doped Al layers in bottom DBR which had a very high oxidation rate. These layers are advantageous for obtaining high power output from VCSELs. Thus, in this thesis, it was necessary to control the wet etching such that it stops exactly at the first layer in bottom DBR. The mesa etching was performed in an etching solution of H_3PO_4–H_2O_2–H_2O with a volume ratio of H_3PO_4–H_2O_2–H_2O ~ 1:1:10. The etching rate was measured and optimized in order to stop mesa etching at the required layer. An SEM image of an etched mesa is shown in Figure 6.2. It shows a few layers of the top DBR, the oxide layer, the active region and the top layer of lower DBR.

108
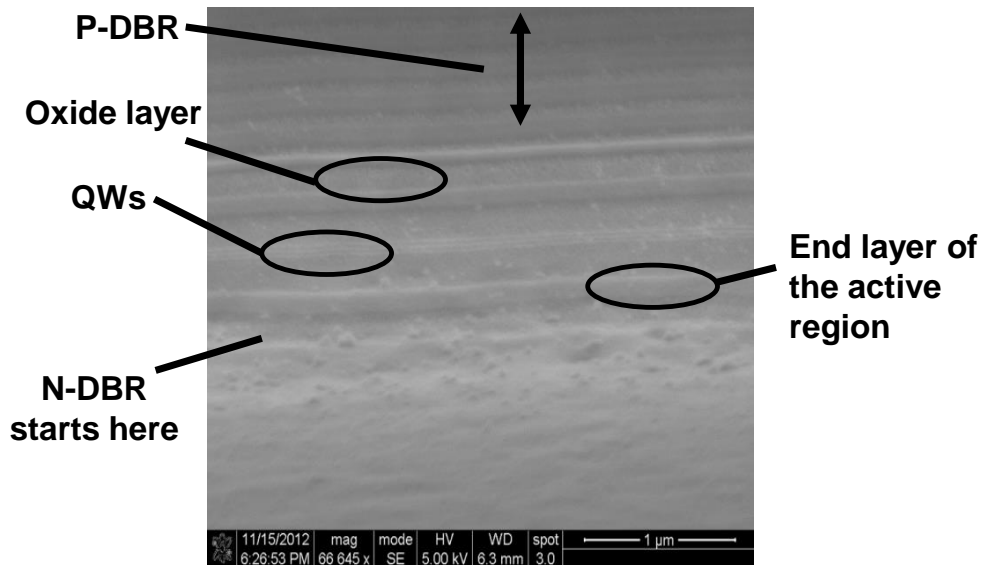
Figure 6.2: SEM image of an etched mesa in a VCSEL epitaxial wafer. It can be seen that the etching was stopped exactly at the top of the bottom DBR

As the etching rate was known, the etching time was optimized so that the lower DBR did not get etched. This was necessary in order to avoid oxidation in the lower DBR which had a high Al content.

(d) Oxide Formation

The sample was washed in PG remover (a solvent used to remove negative tone resists) to remove the resist. An oxide was formed using wet oxidation. A wet oxidation setup was developed for this work. A tube furnace was equipped by the author with additional required components to achieve a functional wet oxidation setup. As shown in Figure 6.3, water vapor was brought into the furnace with N_2 and the temperature of the furnace was set at 450 ^{o}C by a temperature controller. The temperature of the water bubbler was set at 90 ^{o}C. The oxidation rate depended on the amount of N_2 flowing into the furnace through the water bubbler, that was controlled by a flow meter.

Figure 6.3: The wet oxidation setup showing the furnace, the water bubbler, and the N_2 inlet

The oxidation rate was optimized in order to achieve differently sized oxide apertures. The optimized oxidation rate was 1 μm/min.

(e) Aperture Formation and N-type Contacts Deposition

Another step of photolithography followed by dry etching was used to form apertures in the contact layers. An ion miller was used to etch Au/Ti layers after the photolithography step. The photolithography facilitated to form apertures with different diameters. The last step was N-type contact deposition. A combination of AuGe/Ti/Au with thicknesses 50 nm/15 nm/150 nm was used as a N-type contacts.
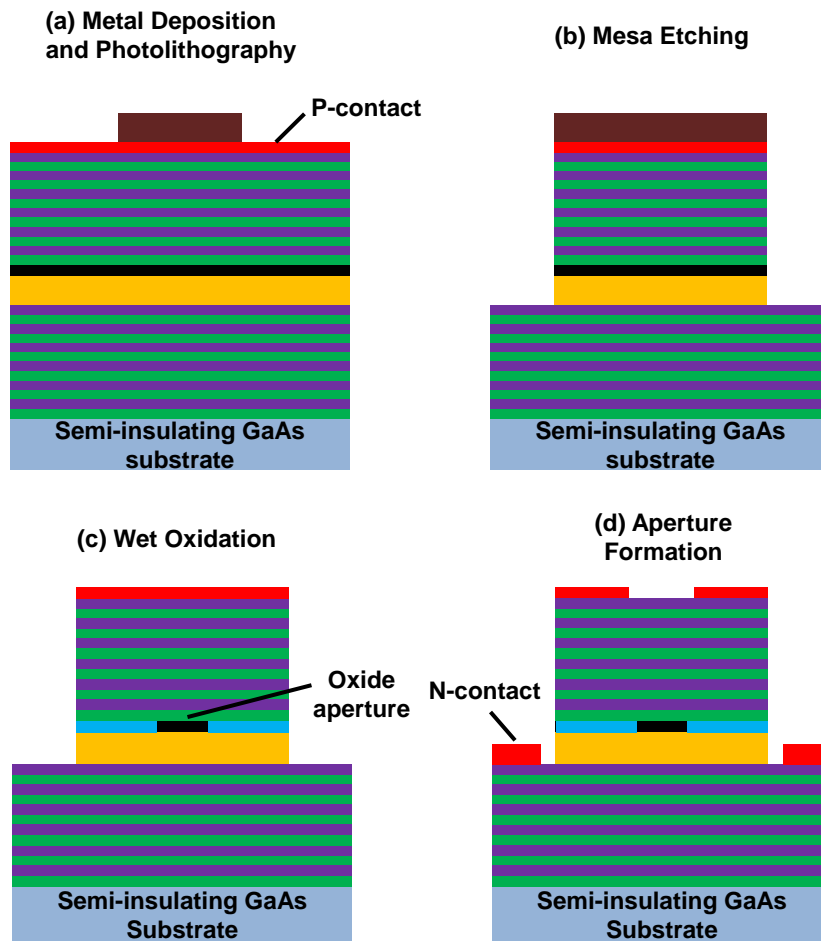
Figure 6.4: Fabrication process of a nano-aperture VCSEL, showing all the steps

A set of mesa sizes including 40, 45, 50, 55, and 60 µm were fabricated. The contacts were 10 µm wide rings on top of each mesa. The oxide aperture was optimized in order to achieve maximum power from the mesas. Mesas and emitting apertures both were circular in shape. Figure 6.4 shows the fabrication process flow for VCSELs. Figure 6.5 shows microscopic images of a fabricated and a lasing VCSEL. The top mesa emitting surface of the VCSEL and positive contacts can be seen in Figure 6.5 (a) and light coming from a lasing VCSEL can be seen in Figure 6.5 (b).
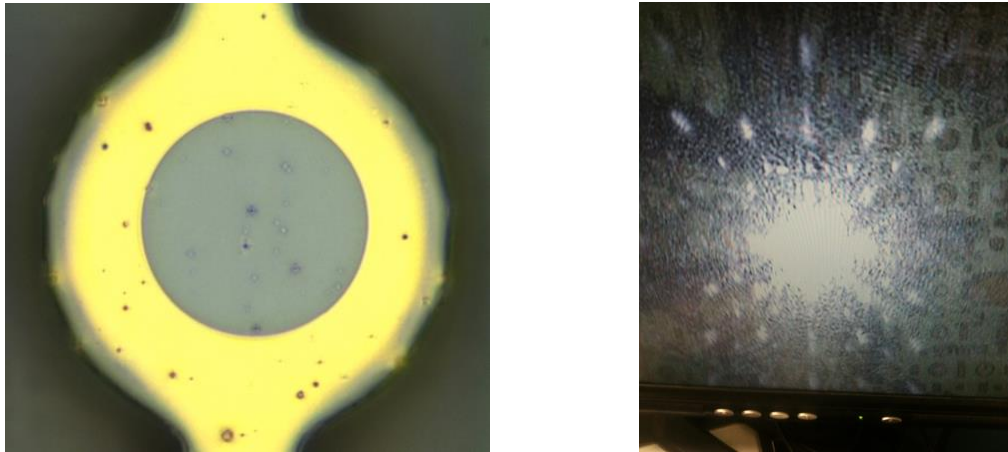
Figure 6.5: Microscopic images of (a) a fabricated VCSEL, and (b) a lasing VCSEL

6.3. Measurement Setup

Far-field powers (PI curves) were measured in order to characterize the nano-aperture VCSELs. Figure 6.6 shows pictures of the experimental setup for power measurements. The VCSEL sample was placed on an XY translation stage which allows moving of a sample in two dimensions. Two contact probes were used to provide electrical contacts for p-type and n-type contacts and an optical microscope was used to align the probe tips.
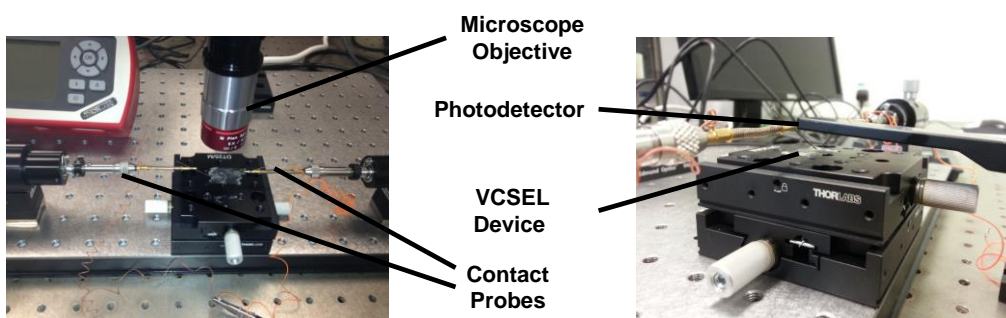
Figure 6.6: The measurement setup used to characterize VCSELs. The probes are used to inject the current into the VCSELs and the photo-detector is used to measure the output power of the VCSELs

The top-emitting power from the VCSEL was collected with a 8 mm-diameter circular Si detector directly above the laser at a distance of 5 mm. These variations are due to the mesa size and aperture size variations which can occur due to small non-uniformities during the lithography and wet oxidation processes. The threshold current and roll off current were ~ 5 mA and ~ 40 mA respectively. The threshold current is the value of the current where the VCSEL starts lasing. The maximum power obtained was ~ 11 mW which is equal to that of most commercially available 850-nm VCSELs. The roll-off point is the value beyond which the output power of the VCSEL starts decreasing and reaches zero again when increasing the current.
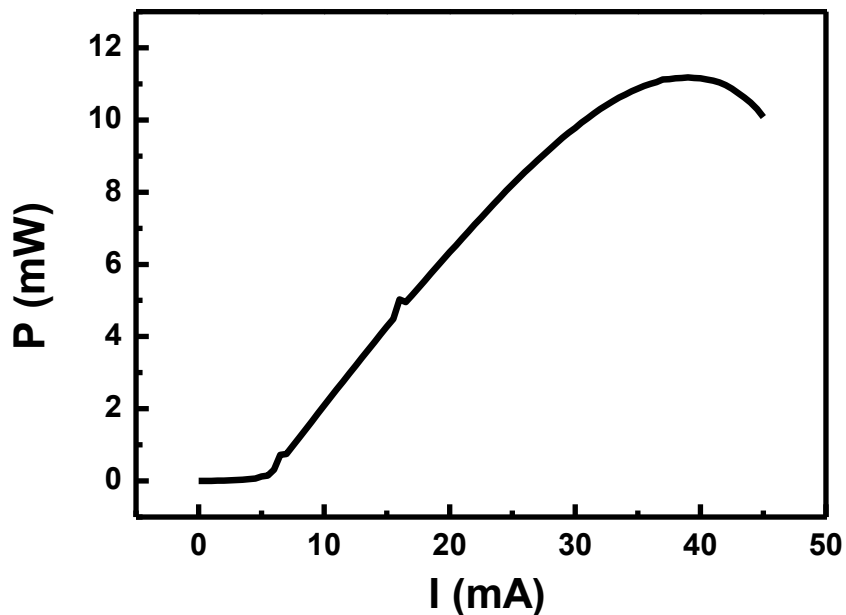
Figure 6.7: A set of PI curves obtained from various VCSELs fabricated on the same wafer

6.4. Nano-aperture VCSELs

A nano-aperture VCSEL design was based on a conventional VCSEL design. A nano-aperture VCSEL was obtained by depositing an Au film on top of a conventional VCSEL and by opening a nano-aperture in the Au layer. Figure 6.8 shows a schematic of a nano-aperture VCSEL based on a conventional VCSEL coated with an Au film. The external quantum efficiency, η, of a nano-aperture VCSEL is defined as the ratio of the emitted optical power over applied electrical power. For a nano-aperture VCSEL, η can be determined by

$$\eta = \eta_i \times \frac{T_{aperture}}{T_{aperture} + \alpha} \qquad \text{Eq. 6.1}$$

where η_i is the injection current efficiency, which represents the percentage of injected carriers contributing to the emission process (some of the carriers are lost due to recombination), α is the total loss during one round trip (i.e. absorption and scattering loss, etc.) and $T_{aperture}$ is the fraction of power
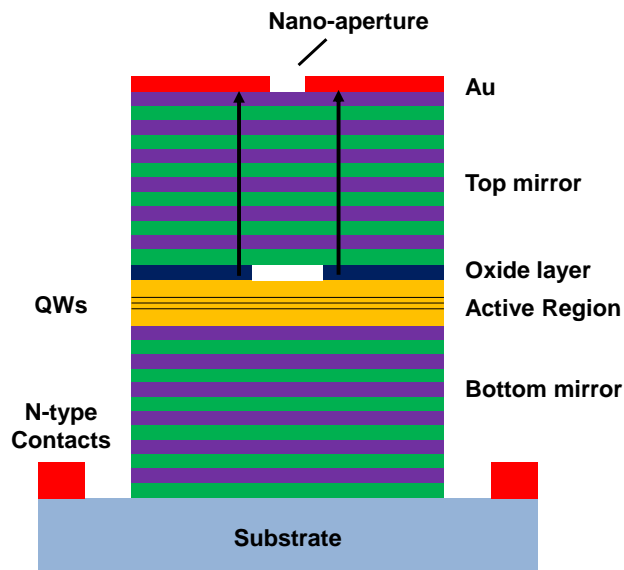
Figure 6.8: Schematic of a nano-aperture VCSEL based on a conventional VCSEL

transmitted to the nano-aperture per round trip. $T_{aperture}$ is given by

$$T_{aperture} = T_{n-DBR} \frac{PT \times A_{aperture}}{A_{mode}} \qquad \text{Eq. 6.2}$$

where T_{n-DBR} is the incident light onto the nano-aperture from the top DBR mirror. PT is the power throughput of the nano-aperture, which is defined as the ratio of the power transmitted through the nano-aperture to the power incident on the nano-aperture. $A_{aperture}$ is the area of the nano-aperture and A_{mode} is the effective area of the optical mode. Equation 6.2 shows that quantum efficiency of a nano-aperture VCSEL can be increased by (1) increasing the intensity incident on the nano-aperture, T_{n-DBR}, (2) decreasing the optical mode area, A_{mode}, or (3) reducing the total loss, α. T_{n-DBR} can be increased by reducing the number of DBR pairs in the top mirror; its reflectivity can be increased by the use of Au coating [127]. The optical mode area, A_{mode}, can be decreased by using a smaller oxide aperture which will reduce the total loss also by reducing the scattering losses. The output power from the nano-aperture VCSEL can then be given by

$$P_{out} = \frac{\hbar\omega}{q} \eta. (I - I_{th}) \qquad \text{Eq. 6.3}$$

where ω is the angular lasing frequency, q is the electron charge, η is the quantum efficiency, I is the injection current and I_{th} is the lasing threshold current. (This explanation is adapted from [89]).

6.5. Fabrication of Differently Shaped Nano-aperture VCSELs

The power density from a VCSEL is more important compared to the peak power because the power throughput of the nano-aperture depends on the incident power density. Thus it was required to increase the quantum efficiency of the nano-aperture VCSELs. As mentioned earlier in Section 6.4, the quantum efficiency of a nano-aperture VCSEL can be enhanced by controlling a set of parameters including the oxide aperture and the number of n-DBR layers. Since the number of layers in the n-DBR stack was designed by the VCSEL epitaxial material provider, it was decided to optimize the oxide aperture and mesa size in order to obtain the maximum power density from a VCSEL before forming the nano-apertures on its lasing facet.

Mesas with a radius between 1 µm and 10 µm were fabricated on the same sample in order to optimize the maximum power density. Mesa size was defined by its radius and it did not include the p-contacts which were 10 µm, in addition to the defined mesa size. The oxide apertures were optimized for all different sized VCSELs, in order to obtain maximum power output. The results are shown in Table 6.1.

Table 6.1: Power densities available for different sizes of active apertures

Mesa Size	Maximum Far-Field Power (mW)	Maximum Power Density $(mW/\mu m^2)$
1 µm	0.150 mW	0.047
2 µm	0.5 mW	0.04
5 µm	3 mW	0.038
10 µm	10 mW	0.031

It can be seen from the results that the smaller oxide apertures show very small power output, because the roll-off current decreases significantly for small oxide apertures due to excessive heating. This limits the maximum power output from a VCSEL, shown by Equation 6.4.

$$P_{out,max} = \frac{\hbar\omega}{q}\eta.(I_{rollover} - I_{th}) \qquad \text{Eq. 6.4}$$

Here η is the quantum efficiency, $I_{rollover}$ is the roll-over current and I_{th} is the threshold current. Thus although smaller oxide aperture can increase the power density, it also reduces the $I_{rollover}$ and in results $P_{out,max}$ is also reduced. The oxide aperture size of 2 µm-radius was chosen as a balance between two factors. Finally, differently shaped nano-apertures were fabricated on the VCSELs with an oxide aperture of 2 µm-radius. Differently shaped nano-apertures were fabricated on the VCSELs' lasing facet using metal deposition, EBL and ion milling. The fabrication process flow is shown in Figure 6.9.
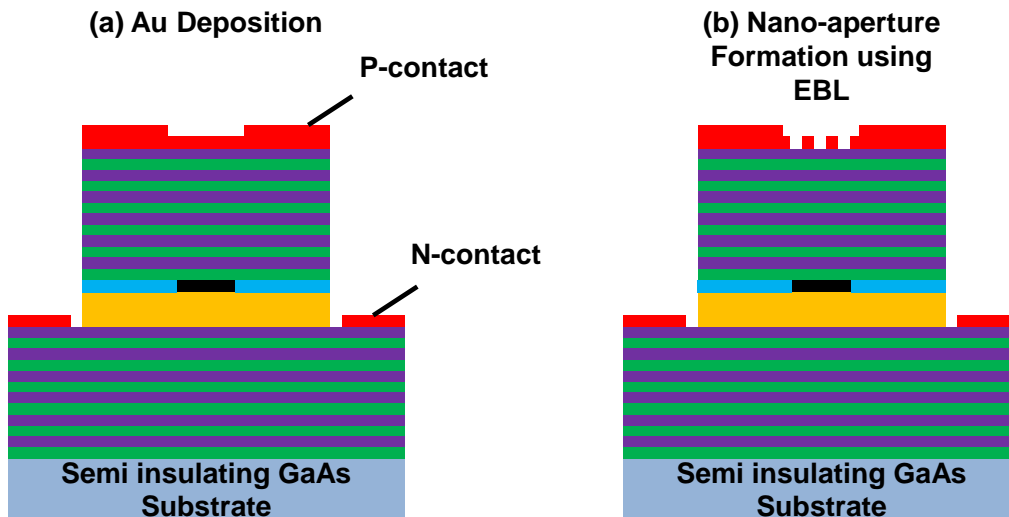
Figure 6.9: Fabrication of nano-aperture VCSELs; (a) Au deposition, (b) nano-aperture formation

A 100-nm thick Au layer was deposited on the VCSEL devices. Nano-apertures were patterned on the Au layer after coating a positive resist (PMMA 950k). The nano-apertures were required to be placed in the center of the top mesa. This was achieved by using a precise alignment procedure during EBL. This is far easier for the VCSELs compared to the edge-emitting lasers where the nano-aperture has to be aligned with the QW region. Ion milling was used to transfer the patterned nano-apertures to the Au layer by etching the nano-apertures. Resist was removed after the etching. Figure 6.10 shows SEM images of differently shaped nano-apertures. A fully fabricated nano-aperture VCSEL can be seen in Figure 6.11. 7×7 arrays of 100 nm apertures were fabricated on VCSELs to increase the power output from the VCSELs, in order to facilitate power measurements.
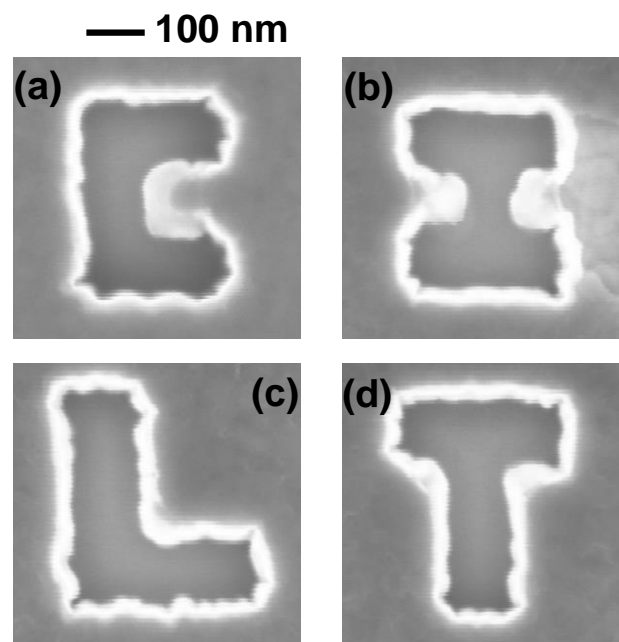
Figure 6.10: SEM images of differently shaped nano-apertures: (a) C-aperture, (b) I-aperture, (c) L-aperture and (d) T-aperture
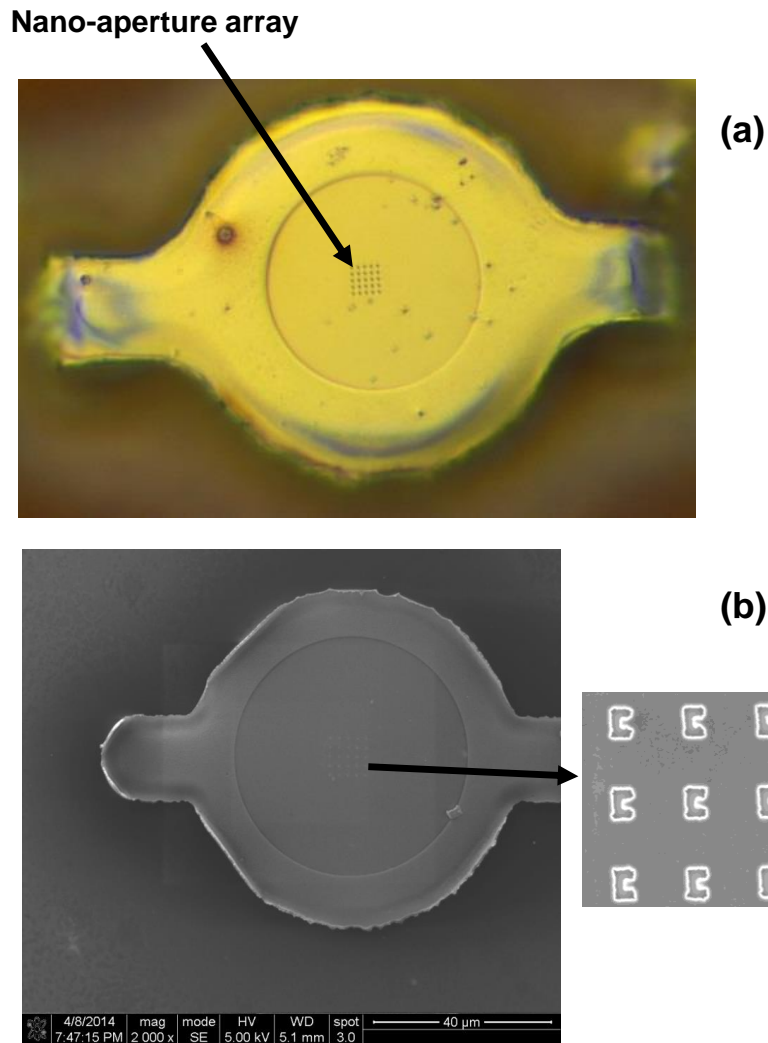
Figure 6.11: (a) Microscopic and (b) SEM image of a fully fabricated nano-aperture VCSEL

The top-emitting power of the VCSELs was measured again and the results are shown in Figure 6.12. A 220-nm square aperture with about the same area as other apertures was also studied for comparison. In comparison among different apertures, the C-aperture VCSEL showed the highest power output. The total far-field maximum power from a single C-aperture was calculated statistically by dividing the total power by number of apertures and was 22 µW which was 7 times higher than that from a square aperture.
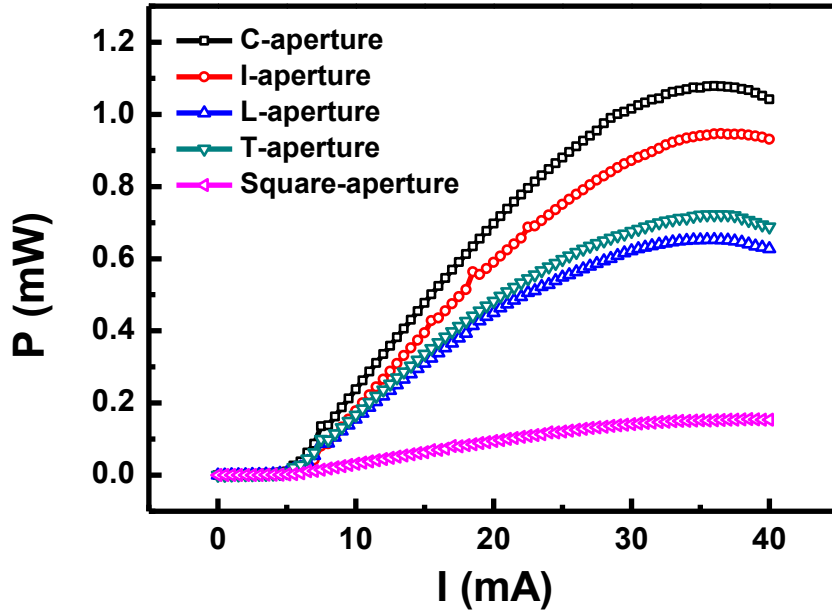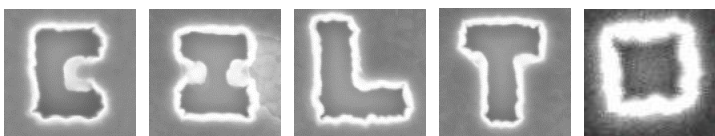
Figure 6.12: The far-field power measured from differently shaped nano-aperture VCSELs

All the power measurements for nano-aperture VCSELs were performed at room temperature without any cooling facility. The performance of the nano-aperture VCSELs, e.g. maximum output power, can be further improved with controlled cooling.

Table 6.2: Comparison of nano-aperture VCSELs using differently shaped nano-apertures

	C-aperture	I-aperture	L-aperture	T-aperture	Square-aperture
Aperture area (nm^2)	4.9×10^4 (nm^2)	4.9×10^4 (nm^2)	4.9×10^4 (nm^2)	4.9×10^4 (nm^2)	4.9×10^4 (nm^2)
Maximum far-field power–array of apertures	1.1 (mW)	0.931 (mW)	0.627 (mW)	0.688 (mW)	0.154 (mW)
Maximum far-field power–single aperture	22 (μW)	19 (μW)	12.7 (μW)	14.4 (μW)	3.14 (μW)

It was shown in previous chapter (Section 5.5) that a C-aperture can exhibit a SP effect in order to obtain HAMR using lower power densities, unlike the square aperture which was unable achieve HAMR because of low power transmission efficiency. C-aperture VCSEL with the same geometrical parameters was fabricated in order to compare the power density available from the VCSELs. The oxide aperture was 2-µm radius in size with 10 µm contacts. A single C-aperture was fabricated on top of the mesa and the measured far-field power is shown in Figure 6.13. The HAMR results in Section 5.7 showed that an optical spot with ~ 1.2-µm diameter was produced by the 1 µm C-aperture. From far-field power out measured from C-aperture VCSEL, the estimated near-field intensity was ~ 0.52 mW/µm^2. This power density is almost half of the power density required to heat the magnetic media above its Curie temperature.
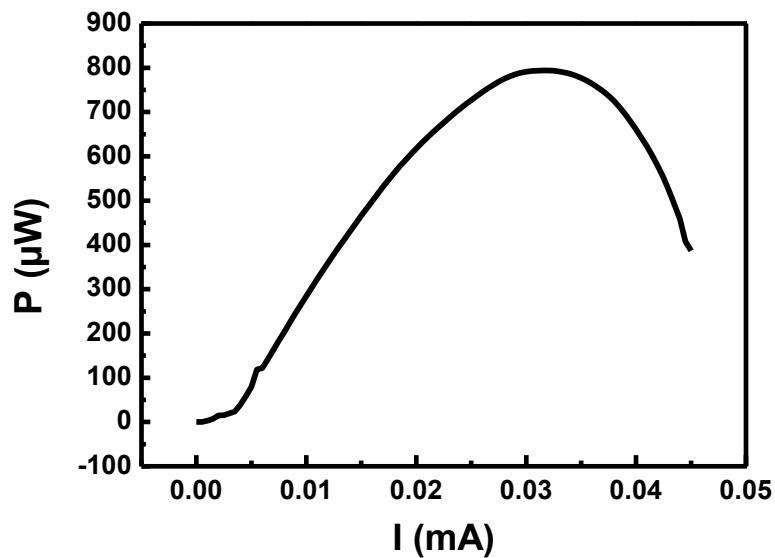
Figure 6.13: Far-field power measured from C-aperture VCSEL

6.6. Summary and Conclusions

The fabrication process for conventional VCSELs has been demonstrated successfully including controlled etching and a wet oxidation process. Far-field power from VCSELs with different sized mesas was measured and it was found that the power density from a VCSEL can be enhanced by optimizing the mesa size and the oxide aperture. The power density from a VCSEL has more importance compared to the peak output power. The VCSEL design was optimized for the maximum peak power and fabricated differently shaped nano-apertures on the facet of these VCSELs. The far-field power was measured and results showed that the C-shaped nano-apertures show the maximum far-field power as anticipated by the simulation in Chapter 3. The near-field intensity can be estimated using the optical spot size and the far-field power.

Chapter 7

Summary and Conclusions

7.1. Summary

This thesis presents a novel light delivery system for HAMR applications. It includes two main parts; a laser source and an NFT. A nano-aperture VCSELs can produce a highly localized optical spot on a magnetic medium to heat it above its Curie temperature to perform HAMR.

Detailed FDTD simulations were performed in order to characterize a suitable NFT comparing the conventional square aperture to unconventional apertures such as C, Bowtie, I, L, and T-shaped apertures. The designs for these apertures were optimized in order to maximize transmission through the apertures at a wavelength of 850 nm. The transmission window area for all the apertures was held constant to have an accurate comparison of the characteristics of the differently shaped nano-apertures. Near-field intensity measurements show that the unconventional apertures demonstrate transmission significantly higher than a square aperture. In comparison to other nano-aperture shapes the C-shaped nano-aperture shows the maximum near-field intensity and the smallest optical spot size; the intensity is ~ 10 times higher than that of the square aperture. These characteristics imply that the C-aperture is the best candidate as an NFT for HAMR applications.

In order to apply the C-aperture in a HAMR system, it is necessary to study the effect of magnetic storage on C-aperture performance. Since the storage

medium is a metal, it is expected to affect the transmission characteristics of the C-aperture by changing the interaction of the C-aperture with the incident light. A detailed simulation and experimental analysis was performed to observe the effect of the magnetic storage media stack on the transmission and focusing characteristics of the C-aperture. The near-field intensity delivered to a magnetic medium reduces drastically as the distance between the medium and the C-aperture increases whereas the optical spot produced increases linearly. The separation between the NFT and the magnetic medium is highly important for the NFT performance.

The resonant transmission through a C-aperture is an important parameter for HAMR applications. A comprehensive study was performed in order to study the effects of the magnetic medium on the resonance of the C-aperture. The resonant wavelength is strongly affected by a magnetic medium placed in the near-field of the C-aperture. The experimental results have a strong correlation with the simulated results. An NFT designed to operate in isolation would not show the same resonance when brought to close proximity of a magnetic medium and thus would perform poorly as an NFT for HAMR applications. Thus re-optimization is required for a C-aperture which is designed to operate in free space.

A detailed experimental analysis is performed to observe the optical characteristics of thin film FePt. Transmission spectra measured for different thicknesses of FePt show that transmission and reflection through the metal is independent of the wavelength of the incident beam. No resonance is observed in the spectra which dictate that the wavelength choice for HAMR is mainly

dependent upon the cost and fabrication of the laser source, which motivates the choice of 850 nm for this thesis.

Coercivity measurements at elevated temperatures show that the Curie temperature of the storage medium (i.e., FePt and underlayers) is 700 K or 425 $^{\circ}$C. A free space far-field optical HAMR setup was designed to characterize HAMR under different parameters like laser power and polarization orientations of the incident laser beam. The required power density for an 850-nm laser to achieve HAMR was found to be 1.4 mW/μm^2. It was found that the polarization orientation of the incident laser beam has no significant difference in HAMR process.

A square aperture is a simple design to focus the laser beam for HAMR but the power transmission through a square aperture reduces significantly when the width of a square aperture is < 1 μm, which is almost equal to the wavelength of the incident laser beam. Thus, a square aperture is not a good choice as an NFT for HAMR applications. A C-aperture was developed and successful HAMR demonstration was achieved, showing the potential of the C-shaped aperture to be used as an NFT for HAMR. The main advantage of the C-aperture is the increased total transmitted power due to the larger total transmission area. At the same time, the plasmonic effect helped to achieve an optical spot which is close to 1 μm in diameter.

A fabrication process for conventional VCSELs was designed and successfully executed. A Au layer was deposited on a conventional VCSEL and a nano-aperture was opened in the layer to achieve a nano-aperture VCSEL. In order to achieve maximum output power from a nano-aperture, a

small oxide aperture is required; however, a small aperture results in a low roll-over current and thus less output power. The optimized oxide aperture is approximately 2 µm in radius. Arrays of differently shaped 100-nm nano-apertures including square, C, I, L, T-shaped nano-apertures were fabricated in the Au layer deposited on the top facet of the VCSELs. The C-shaped VCSELs provided the maximum far-field power in comparison to the other apertures. VCSELs with a 1-µm C-aperture showed a far-field power of ~ 700 µW – 900 µW. Since the magnetic spot produced in the magnetic medium is 1.4 µm in diameter, the estimated near-field intensity is ~ 0.38 – 0.52 mW/µm^2.

The power density achieved from the C-aperture VCSELs is nearly half of the experimentally-confirmed power density required for HAMR. Thus it can achieve a ~ 50% reduction in coercivity of the magnetic medium. It can facilitate HAMR using a magnetic field which is half the room temperature coercivity of the media. This is the main finding of this thesis.

7.2. Future Work

The main challenges faced for the approach proposed in this thesis are the relatively low power output from a nano-aperture VCSEL and the complete integration of a nano-aperture VCSEL with existing write head designs. This section discusses the challenges and their possible solutions as future work recommendations.

7.2.1. Optimization of Output Power from Nano-aperture VCSELs

The main challenge in the direct light delivery approach is to achieve sufficient power density from VCSELs required for HAMR. The results in this thesis showed that VCSELs show promising power output and further optimization can likely make it possible to achieve adequate power output from the nano-aperture VCSELs. Figure 7.1 shows a schematic of a typical nano-aperture VCSEL. As discussed before in Section 6.4, the external quantum efficiency of a nano-aperture VCSEL depends upon the fraction of power transmitted to the nano-aperture from the active region i.e., $T_{aperture}$, which is given as below:

$$T_{aperture} = T_{n-DBR} \frac{PT \times A_{aperture}}{A_{mode}} \qquad \text{Eq. 7.1}$$

where T_{n-DBR} is the incident light onto the nano-aperture from the top DBR mirror. PT is the power throughput of the nano-aperture, which is defined as
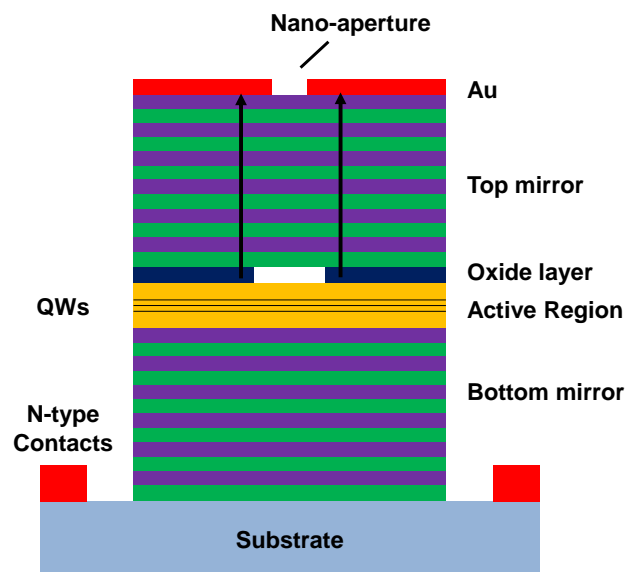
Figure 7.1: Schematic structure of a nano-aperture VCSEL

the ratio of the power transmitted through the nano-aperture to the power incident on the nano-aperture. $A_{aperture}$ is the area of the nano-aperture and A_{mode} is the effective area of the optical mode. Equation 7.1 shows that the quantum efficiency of a nano-aperture VCSEL can be increased by (1) increasing the intensity incident on the nano-aperture, T_{n-DBR}, (2) decreasing the optical mode area, A_{mode}, or (3) reducing the total loss, α. In this thesis, method (2) was utilized in order to optimize the power output from the nano-aperture VCSEL, by optimizing the oxide aperture size of the VCSELs. Another method of increasing output power is to increase T_{n-DBR} by reducing the number of top-DBR pairs; its reflectivity can be increased by the use of a Au coating [127]. This requires re-growth of the VCSEL wafer or etching of the VCSEL wafer in the top-DBR to reduce the top-DBR layers. Epitaxial growth optimization can likely supply the necessary improvements in output power.

7.2.2. Integration of VCSEL with Magnetic Write-Head

The integration of a nano-aperture VCSEL with the existing magnetic write-head is another major challenge involved in the proposed light delivery system. Although this challenge is beyond the scope of this thesis, a few possible solutions can still be proposed for this problem. A typical write head consists of a writer and reader. The writer contains two magnetic poles: (1) the main pole and, (2) the return pole. The return pole is shared by the reader also as a shield. The integration requires re-designing of the write head such that the writer and reader are no longer together. The write poles can be potentially

separated from the reader and grown on the VCSEL wafer such that it can be placed along the nano-aperture. Figure 7.2 shows a top, side and 3D view of the proposed schematic. The return pole is typically bigger than the main pole. The main pole can be placed beside the nano-aperture so that the magnetic field is applied while the magnetic medium is heated by the NFT. Since the disk is rotating at a high speed and the media cooling time is very small, it is necessary to put the NFT and main magnetic write pole close, so that the heating and magnetic reversal can be achieved simultaneously.

Figure 7.2: Schematic showing integration of the write head and nano-aperture VCSEL. (a) Side view, (b) top view, and (c) 3D view

Re-designing of a write-head, though, involves many optimization challenges, which can be a difficult task to accomplish, yet possible.
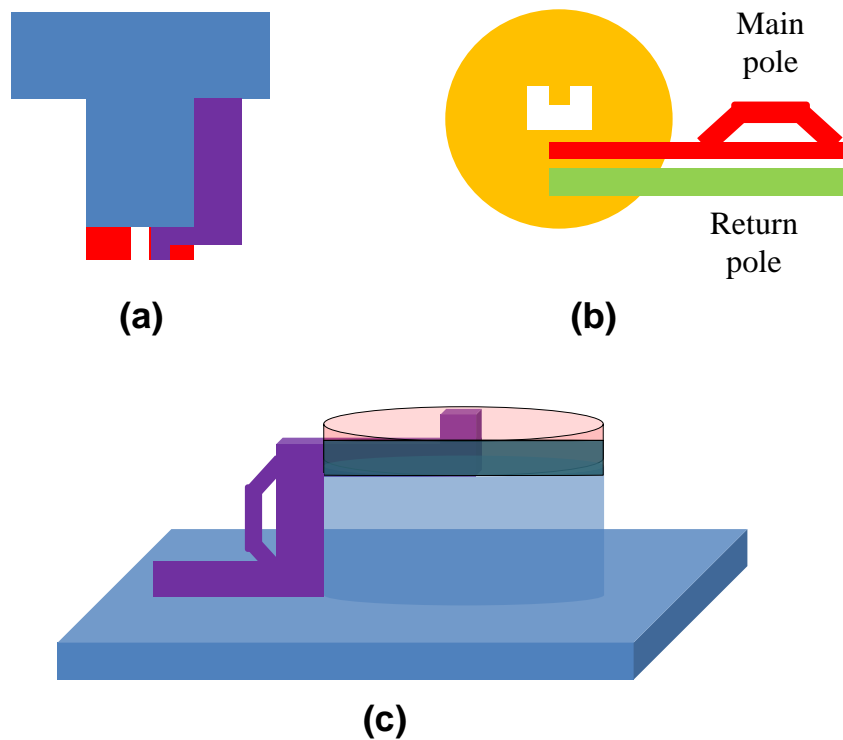
References

1.   H. Saga, H. Nemoto, H. Sukeda, and M. Takahashi, "New recording method combining thermo-magnetic writing and flux detection," Jpn. J. Appl. Phys. **38**, 1839 (1999).

2.   H. Katayama, S. Sawamura, Y. Ogimoto, J. Nakajima, K. Kojima, and K. Ohta, "New magnetic recording method using laser assisted read/write technologies," J. Magn. Soc. Jpn. **23**, 233 (1999).

3.   P. r. t. "http://www.extremetech.com/computing/122921-seagate-hits-1-terabit-per-square-inch-60tb-drives-on-their-way.

4.   D. C. Mee, and E. D. Daniel, *Magnetic Storage Handbook* (McGraw-Hill, 1990).

5.   E. d. T. d. Lacheisserie, D. Gignoux, and M. Schlenker, *Magnetism: Fundamentals* (Springer, 2004).

6.   S. N. Piramanayagam, and T. C. Chong, *Developments in Data Storage: Materials Perspective* (Wiley-IEEE Press, 2011).

7.   E. D. Daniel, C. D. Mee, and M. H. Clark, *Magnetic Recording: The First 100 Years* (Wiley-IEEE Press, 1999).

8.   S. Schoenherr, "The History of Magnetic Recording."

9.   A. Moser, K. Takano, D. T. Margulies, M. Albrecht, Y. Sonobe, Y. Ikeda, S. Sun, and E. E. Fullerton, "Magnetic recording: Advancing into the future," Phys. D: Appl. Phys. **35**, R157 (2002).

10.   Y. Shiroishi, K. Fukuda, I. Tagawa, H. Iwasaki, S. Takenoiri, H. Tanaka, H. Mutoh, and N. Yoshikawa, "Future options for HDD storage," IEEE Trans. Magn. **45**, 3816 (2009).

11.   N. Inaba, and M. Futamoto, "Effects of Pt and Ta addition on compositional microstructure of CoCr-alloy thin film media," J. Appl. Phys **87**, 6863 (2000).

12.   C. R. Paik, I. Suzuki, N. Tani, M. Ishikawa, Y. Ota, and K. Nakamura, "Magnetic properties and noise characteristics of high coercivity CoCrPtB/Cr Media," IEEE Trans. Magn. **28**, 3084 (1992).

13.   D. E. Laughlin, Y. C. Feng, D. N. Lambeth, L. L. Lee, and L. Tang, "Design and crystallography of multilayered media," J. Magn. Magn. Mater. **155**, 146 (1996).

14.   L. L. Lee, D. E. Laughlin, L. Fang, and D. N. Lambeth, "Effects of Cr intermediate layers on CoCrPt thin film media on NiAl underlayers," IEEE Trans. Magn. **31**, 2728 (1995).

15.   B. B. Lal, M. Tobise, and T. Shinohara, "Effect of very thin Cr-underlayer on the magnetic and recording properties of CoCrTa thin-film media," IEEE Trans. Magn. **30**, 3954 (1994).

16.   G. Choe, J. N. Zhou, B. Demczyk, M. Yu, M. Zheng, R. Weng, A. Chekanov, K. E. Johnson, F. Liu, and K. Stoev, "Highly in-plane oriented CoCrPtB longitudinal media for 130-Gb/in2 recording," IEEE Trans. Magn. **39**, 633 (2003).

17.   http://www.toshiba.co.jp/about/press/2004_12/pr1401.htm.

18.   J. Eisenmenger, and I. K. Scheller, "Magnetic nanostructures: Overcoming thermal fluctuations," Nat. Mater. **2** (2003).

19.   S. H. Charap, P.-L. Lu, and Y. He, "Thermal stability of recorded information at high densities," IEEE Trans. Magn. **33**, 978 (1997).

20. S. N. Piramanayagam, "Perpendicular recording media for hard disk drives," J. Appl. Phys. **102**, 011301 (2007).

21. H. J. Richter, "The transition from longitudinal to perpendicular recording," J. Phys. D. Appl. Phys. **40**, R149 (2007).

22. S. Iwasaki, and K. Takemura, "An analysis for the circular mode of magnetization in short wavelength recording," IEEE Trans. Magn. **11**, 1173 (1975).

23. S. Iwasaki, and Y. Nakamura, "The magnetic field distribution of a perpendicular recording head," IEEE Trans. Magn. **14**, 436 (1978).

24. S. Iwasaki, Y. Nakamura, and K. Ouchi, "Perpendicular magnetic recording with a composite anisotropy film," IEEE Trans. Magn. **61**, 1456 (1979).

25. S. Khizroev, and D. Litvinov, "Perpendicular magnetic recording: Writing process," J. Appl. Phys. **95**, 4521 (2004).

26. L. Wu, T. Kita, N. Honda, and K. Ouchi, "Medium noise properties of Co/Pd multilayer films for perpendicular magnetic recording.," J. Magn. Magn. Mater. **193**, 89 (1999).

27. H. Uwazumi, T. Shimatsu, Y. Sakai, Y. A. Otsuki, I. Watanabe, H. Muraoka, and Y. Nakamura, "Recording performance of CoCrPt-(Ta, B)/TiCr perpendicular recording media," IEEE Trans. Magn. **37**, 1595 (2001).

28. T. Oikawa, M. Nakamura, H. Uwazumi, T. Shimatsu, H. Muraoka, and Y. Nakamura, "Microstructure and magnetic properties of CoPtCr–SiO$_2$ perpendicular recording media," IEEE Trans. Magn. **38**, 1976 (2002).

29. I. Tamai, R. Araki, and K. Tanahashi, "Magnetic and recording characteristics of CoCrPt-oxide media with a mixture of SiO$_2$ and TiO$_2$," IEEE Trans. Magn. **44**, 3492 (2008).

30. T. Chiba, J. Ariake, and N. Honda, "Structure and magnetic properties of Co-Pt-Ta2O5 film for perpendicular magnetic recording media," J. Magn. Magn. Mater. **287**, 167 (2005).

31. R. Araki, Y. Takahashi, I. Takekuma, and S. Narishige, "High-resolution TEM analysis of perpendicular CoCrPt-SiO$_2$ media," IEEE Trans. Magn. **44**, 3496 (2008).

32. "Hitachi shows technical feasibility of perpendicular magnetic recording at 610 Gbit/in^2 [online] (2008, July 28). Available at: http://www.hitachi.com/New/cnews/080728b.pdf."

33. R. H. Victora, and X. Shen, "Composite media for perpendicular magnetic recording," IEEE Trans. Magn. **41**, 537 (2005).

34. J.-P. Wang, W. Shen, and J. Bai, "Exchange coupled composite media for perpendicular magnetic recording," IEEE Trans. Magn. **41**, 3181 (2005).

35. A. Berger, N. Supper, Y. Ikeda, B. Lengsfield, A. Moser, and E. E. Fullerton, " Improved media performance in optimally coupled exchange spring layer media," Appl. Phys. Lett. **93**, 122502 (2008).

36. C. A. Ross, "Patterned magnetic recording media," Rev. Mater. Res. **31**, 203 (2001).

37. B. D. Terris, and T. Thomson, "Nanofabricated and self-assembled magnetic structures as data storage media," J. Phys. D: Appl. Phys. **38**, R199 (2005).

38. B. D. Terris, T. Thomson, and G. Hu, "Patterned media for future magnetic data storage," Microsyst. Technol. **13** (2007).

39. H. J. Richter, A. Y. Dobin, O. Heinonen, K. Z. Gao, R. J. M. Veerdonk, R. T. Lynch, J. Xue, D. Weller, P. Asselin, M. F. Erden, and R. M. Brockie, "Recording on bit-patterned media at densities of 1 Tb/in^2 and beyond," IEEE Trans. Magn. **42**, 2255 (2006).

40. "Chris Mellor, Toshiba gets bit-patterning between its teeth; HAMR may come too, [online] (July 14, 2011). Available at: http://www.theregister.co.uk/2011/07/14/toshiba_yamamoto_san/."

41. J.-G. Zhu, X. Zhu, and Y. Tang, " Microwave assisted magnetic recording," IEEE Trans. Magn. **44**, 125 (2008).

42. L. Lu, M. Wu, M. Mallary, G. Bertero, K. Srinivasan, R.Acharya, H. Schultheiß, and A. Hoffmann, "Observation of microwave-assisted magnetization reversal in perpendicular recording media," Appl. Phys. Lett. **103**, 042413 (2013).

43. Y. Wang, (Carnegie Mellon University, 2011).

44. H. Katayama, S. Sawamura, Y. Ogimoto, J. Nakajima, K. Kojima, and K. Ohta, " New magnetic recording method using laser assisted read/write technologies," J. Magn. Soc. Jpn. **23**, 233 (1999).

45. J.-U. Thiele, K. R. Coffey, M. F. Toney, J. A. Hedstrom, and A. J. Kellock, "Temperature dependent magnetic properties of highly chemically ordered $Fe_{55-x} Ni_x Pt_{45}$ $L1_0$ films " J. Appl. Phys. **91**, 6595 (2002).

46. M. A. Seigler, W. A. Challener, E. Gage, N. Gokemeijer, B. Lu, K. Pelhos, C. Peng, R. E. Rottmayer, X. Yang, H. Zhou, X. Zhu, and T. Rausch, "Heat assisted magnetic recording with a fully integrated recording head , in ODS " (2007).

47. T. Rausch, C. D. Mihalcea, K. Pelhos, C. Peng, E. C. Gage, K. M. eld, M. A. Seigler, and W. A. Challener, "Spin stand characterization of dielectric optical waveguides fabricated on AlTiC sliders for heat assisted magnetic recording," Proc. SPIE — Optical Data Storage, 40 (2004).

48. D. Weller, and A. Moser, "Thermal effect limits in ultrahigh - density magnetic recording " IEEE Trans. Magn **35**, 4423 (1999).

49. Y. Peng, J.-G. Zhu, and D. E. Laughlin, "$L1_0$ FePt – MgO perpendicular thin fi lm deposited by alternating sputtering at elevated temperature " J. Appl. Phys. **99**, 08F907 (2006).

50. J. S. Chen, B. C. Lim, J. F. Hu, B. Liu, and G. M. Chow, "High coercivity $L1_0$ FePt films with perpendicular anisotropy deposited on glass substrate at reduced temperature," Appl. Phys. Lett **90**, 042508 (2007).

51. J. S. Chen, B. C. Lim, J. F. Hu, B. Liu, G. M. Chow, and G. Ju, "Low temperature deposited $L1_0$ FePt - C (001) films with high coercivity and small grain size " Appl. Phys. Lett. **91**, 132506 (2007).

52. S. H. Vemuri, P. S. Chung, R. L. Smith, N. E. Lee, L. T. Biegler, and M. S. Jhon, "Head-disk interface design in magnetic data storage," J. Appl. Phys **111**, 07B721 (2012).

53. H. Bethe, "Theory of diffraction by small holes " Phys. Rev. **66**, 163 (1944).

54. M. Ohtsu, and H. Hori, *Near-Field Nano-Optics* (Kluwer, 1999).

55. E. Betzig, J. K. Trautman, T. D. Harris, J. S. Weiner, and R. L. Kostelak, "Breaking the diffraction barrier: Optical microscopy on a nanometric scale," Science **251**, 1468 (1991).

56. E. X. Jin, and X. Xu, "Finite-Difference Time-Domain studies on optical transmission through planar nano apertures in a metal film," Jpn. J. Appl. Phys. **43**, 407 (2004).

57. L. Wang, S. M. Uppuluri, E. X. Jin, and X. Xu, "Nanolithography Using High Transmission Nanoscale Bowtie Apertures," Nano Lett. **6**, 361 (2006).

58. J. Xu, T. Xu, J. Wang, and Q.Tian, "Design tips of nanoapertures with strong field enhancement and proposal of novel L-shaped aperture," Opt. Eng. **44** 018001 (2005).

59. N. Zhou, E. C. Kinzel, and X. Xu, "Nanoscale ridge aperture as near-field transducer for heat-assisted magnetic recording " Appl. Opt. **50** G42 (2011).

60. X. Shi, R. L. Thornton, and L. Hesselink, "A Nano-aperture with 1000x Power Throughput Enhancement for Very Small Aperture Laser System (VSAL)," Proc. of SPIE **4342**, 320 (2002).

61. K. Nakagawa, "Confined circularly polarized light generated by nano-size aperture for high density all-optical magnetic recording," J. Appl. Phys. **109**, 07B735 (2011).

62. S. Omodani, T. Saiki, and M. Obara, "Metallic slit aperture as a near-field optical head for heat-assisted magnetic Recording," J. Appl. Phys. **105,** , 013101 (2009).

63. R. D. Grober, R. J. Schoelkop, and D. E. Prober, "Optical antenna: Towards a unity efficiency near-field optical probe," Appl. Phys. Lett. **70**, 1354 (1997).

64. R. M. Bakker, A. Boltasseva, Z. Liu, R. H. Pedersen, S. Gresillon, A. V. Kildishev, V. P. Drachev, V. M. Shalaev, B. B. Lal, and M. Tobise, "Near-field excitation of nanoantenna resonance," Opt. Expr. **15**, 13682 (2007).

65. E. Cubukcu, E. A. Kort, K. B. Crozier, and F. Capasso, "Plasmonic laser antenna," Appl. Phys. Lett. **89**, 093120 (2006).

66. N. Yu, E. Cubukcu, L. Diehl, M. A. Belkin, K. B. Crozier, F. Capasso, D. Bour, S. Corzine, and G. Ho¨flere, "Plasmonic quantum cascade laser antenna," Appl. Phys. Lett. **91**, 173113 (2007).

67. T. Matsumoto, Y. Anzai, T. Shintani, K. Nakamura, and T. Nishida, "Writing 40-nm marks using a beaked metallic plate near-field optical probe," in *ISOM/ODS Conf.*(2005).

68. T. Matsumoto, T. Shimano, H. Saga, H. Sukeda, and M. Kiguchi, "Highly efficient probe with a wedge-shaped metallic plate for high density near-field optical recording," J. Appl. Phys. **95**, 3901 (2004).

69. T. Matsumoto, Y. Anzai, T. Shintani, K. Nakamura, and T. Nishida, "Writing 40 nm marks by using a beaked metallic plate near-field optical probe," Opt. Lett. **31**, 259 (2006).

70. T. Matsumoto, K. Nakamura, T. Nishida, H. Hieda, A. Kikitsu, K. Naito, T. Koda, B. B. Lal, and M. Tobise, "Thermally assisted magnetic recording on bit-patterned magnetic medium using near-field optical head with beaked metallic plate," presented at the MORIS 2007 Tech. Dig.2007.

71. M. H. Kryder, E. C. Gage, T. W. McDaniel, W. A. Challener, R. E. Rottmayer, G. Ju, Y.-T. Hsia, and M. F. Erden, "Heat assisted magnetic recording," Proc. IEEE **96**, 1810 (2008).

72. W. A. Challener, C. Peng, A. V. Itagi, D. Karns, W. Peng, Y. Peng, X. Yang, X. Zhu, N. J. Gokemeijer, G. J. Y.-T. Hsia, R. E. Rottmayer, M. A.

Seigler, and E. C. Gage, "Heat-assisted magnetic recording by a near-field transducer with efficient optical energy transfer," Nature Photon. **3**, 220 (2009).

73.   B. C. Stipe, T. C. Strand, C. C. Poon, H. Balamane, T. D. Boone, J. A. Katine, J.-L. Li, V. Rawat, H. Nemoto, A. Hirotsune, O. Hellwig, R. Ruiz, E. Dobisz, D. S. Kercher1, N. Robertson, T. R. Albrecht, and B. D. Terris, "Magnetic recording at 1.5 Pb m^{-2} using an integrated plasmonic antenna," Nature Photon. **4**, 484 (2010).

74.   P. Rai-Choudhary, *Handbook of Microlithography, Micromachining, and Microfabrication: Microlithography* (SPIE Press 1997).

75.   N. W. Parker, A. D. Brodie, and J. H. McCoy, "High-throughput NGL electron-beam direct-write lithography system," Proc. SPIE **3997**, 713 (2000).

76.   R. F. Egerton, *Physical Principles of Electron Microscopy: An Introduction to TEM, SEM, and AEM* (Springer 2005).

77.   S. Foner, "Versatile and Sensitive Vibrating-Sample Magnetometer," Rev. Sci. Instrum. **30**, 548 (1959).

78.   "D. Speliotis, Getting the Most From Your Vibrating Sample Magnetometer, ADE Technologies, Inc., Newton MA.."

79.   Y. Martin, and H. K. Wickramasinghe, " Magnetic imaging by "force microscopy" with 1000 Å resolution," Appl. Phys. Lett. **50**, 1455 (1987).

80.   D. Rugar, H. J. Mamin, P. Guethner, S. E.Lambert, J. E. Stern, I. McFadyen, and T.Yogi, "Magnetic force microscopy: General principles and application to longitudinal recording media," J. Appl. Phys. **68**, 1169 (1990).

81.   I. V. Yaminsky, and A. M. Tishin, "Magnetic force microscopy," Russ. Chem. Rev. **68**, 165 (1999).

82.   L. Abelmann, S. Porthun, M. Haast, C. Lodder, A. Moser, M. E. Best, P. J. A. v. Schebdel, B. Stiefel, H. J. Hug, G. P. Heydon, A. Farely, S. R. Hoon, T. Pfaffelhuber, R. Proksh, and K. Babcock, "Comparing the resolution of magnetic force microscopes using the CAMST reference sample," J. Magn. Magn. Mater. **190**, 135 (1998).

83.   W. A. Challener, E. Gage, A. Itagi, and C. Peng, "Optical transducers for near fi eld recording," Jpn. J. Appl. Phys. **45** 6632 (2006).

84.   L. Novotny, and B. Hecht, *Principles o f Nano-Optics* (Cambridge University Press, , 2007).

85.   Y. Kong, "Fabrication and Optical Investigation of Heat-Assisted Magnetic Recording Devices," in *Electrical and Com puter Engineering*(Carnegie Mellon University, 2013).

86.   T. W. Ebbesen, C. Genet, and S. I. Bozhevolnyi, "Surface-plasmon circuitry," Physics Today **61**, 44 (2008).

87.   A. V. Zayatsa, I. I. S. olyaninovb, and A. A. M. aradudin, "Nano-optics of surface plasmon polaritons," Physics Reports **408**, 131 (2005).

88.   K. S. Yee, "Numerical solution of initial boundary value problems involving Maxwell's equations in isotropic media," IEEE Transactions On Antennas and Propagation **AP14**, 302 (1966).

89.   Z. Rao, "High-Intensity Nano-Aperture Lasers For Near-Field Optics," in *The Department of Physics*(Stanford University, 2007).

90.   J. P. Berenger, "A perfectly matched layer for the absorption of electromagnetic waves," J. Comput. Phys. **114**, 185 (1994).

91.   H. A. Bethe, "Theory of diffraction by small holes," Phys. Rev. **66**, 163 (1944).

92.   E. D. Palik, *Handbook of Optical Constants of Solids* (Academic, 1998).

93.   K. Tanaka, and M. Tanaka, "Simulation of an aperture in the thick metallic screen that gives high intensity and small spot size using surface plasmon polaritons," J. Micro. **210**, 294 (2003).

94.   L. Wang, S. M. Uppuluri, E. X. Jin, and X. Xu, "Nanolithography using high transmission nanoscale bowtie apertures", ," Nano Lett. **6**, 361 (2006).

95.   J. Xu, T. Xu, J. Wang, and Q. Tian, "Design tips of nanoapertures with strong field enhancement and proposal of novel L-shaped aperture," Opt. Eng. **44**, 018001/018001 (2005).

96.   N. Zhou, E. C. Kinzel, and X. Xu, "Nanoscale ridge aperture as near-field transducer for heat-assisted magnetic recording," Appl. Opt. **50**, G42 (2011).

97.   X. Shi, R. L. Thornton, and L. Hesselink, "A Nano-aperture with $1000\times$ Power Throughput Enhancement for Very Small Aperture Laser System (VSAL)," in *Optical Data Storage* (Proceedings of SPIE, Terril Hurst, 2002), p. 320.

98.   K. Nakagawa, "Confined circularly polarized light generated by nano-size aperture for high density all-optical magnetic recording," J. Appl. Phys. **109**, 07b735 (2011).

99.   S. Omodani, T. Saiki, and M. Obaraa, "Metallic slit aperture as a near-field optical head for heat-assisted magnetic Recording," J. Appl. Phys. **105**, 013101/013101 (2009).

100.   W. A. Challener, and A. V. Itagi, "Near-Field Optics for Heat-Assisted Magnetic Recording (Experiment, Theory, and Modeling)," M. Schlesinger (ed.), Modelling and Numerical Simulations II, Modern Aspects of Electrochemistry **44** (2009).

101.   M. H. Kryder, E. C. Gage, T. W. McDaniel, W. A. Challener, R. E. Rottmaye, G. Ju, Y.-T. Hsia, and M. F. Erden, "Heat Assisted Magnetic Recording," Proc. IEEE **96**, 1810 (2008).

102.   K. Sato, A. Mizusawa, K. Ishida, T. Seki, T. Shima, and K. Takanashi, "Magneto-Optical Spectra of Ordered and Disordered FePt Films Prepared at Reduced Temperatures," Trans. Magn. Soc. Jpn. **4** 297 (2004).

103.   P. B. Johnson, and R. W. Christy, "Optical Constants of the Noble Metals," Phys. Rev. B **6**, 4370 (1972).

104.   J. Bass, J. S. Dugdale, C. L. Foiles, and A. Myers, *Metals: Electronic Transport Phenomena: Electrical Resistivity, Thermoelectrical Power and Optical Properties* (Springer 1985).

105.   K. Sendur, and P. Jones, "Effect of fly height and refractive index on the transmission efficiency of near-field optical transducers," Appl. Phys. Lett. **88**, 091110 (2006).

106.   J. Gui, "Tribology challenges for head-disk interface toward 1 Tb/in^2," IEEE Trans. Magn. **39**, 716 (2003).

107.   R. Wood, "The feasibility of magnetic recording at 1 Terabit per square inch," IEEE Trans. Magn. **36**, 36 (2000).

108.   L. Sun, R. K. Batra, X. Shi, and L. Hesselink, "Topology Visualization of the Optical Power Flow through a Novel C-Shaped Nano-Aperture," IEEE Visualization, 337 (2004).

109. P. Nordlander, and E. Prodan, "Plasmon Hybridization in Nanoparticles near Metallic Surfaces," Nano Lett. **4**, 2209 (2004).

110. F. Le, N. Z. Lwin, J. M. Steele, M. Kall, N. J. Halas, and P. Nordlander, "Plasmons in the Metallic Nanoparticle−Film System as a Tunable Impurity Problem," Nano Lett. **5**, 2009 (2005).

111. S. P. Powell, E. J. Black, T. E. Schlesinger, and J. A. Bain, "The influence of media optical properties on the efficiency of optical power delivery for heat assisted magnetic recording," J. Appl. Phys. **109**, 07B775 (2011).

112. K. Sendur, and W. Challener, "Patterned medium for heat assisted magnetic recording," Appl. Phys. Lett. **94**, 032503 (2009).

113. K. K. M. Pandey, N. Gaur, and C. S. Bhatia, "Interface mediated control of microstructure and magnetic properties of FePt-C thin films," J. Magn. Magn. Mater. **323**, 2658 (2011).

114. N. Gaur, "Investigations on ion implantation in advanced magnetic recording media " (National University of Singapore, 2013).

115. G. J. Fokken, W. L. Walters, L. F. Mattson, and B. K. Gilbert, "Low-cost, multi-Ghz electrical packaging for serial optoelectronic links utilizing vertical cavity surface emitting lasers," IEEE Trans. Adv. Packag. **23**, 42 (2000).

116. J. Geske, V. Jayaraman, T. Goodwin, M. Culick, M. MacDougal, T.Goodnough, D. Welch, and J. E. Bowers, "2.5-Gb/s transmission over 50 km with a 1.3-nm vertical-cavity surface-emitting laser," IEEE Photon.Technol. Lett. **12**, 1707 (2000).

117. H. Kosaka, "Smart integration and packaging of 2D VCSEL's for high-speed parallel links," IEEE Select. Topics Quantum Electron. **5**, 184 (1999).

118. K. Kasahara, "VSTEP-based smart pixels," IEEE J. Quantum Electron **29**, 757 (1993).

119. H. Soda, K. Iga, C. Kitahara, and Y. Suematsu, "GaInAsP/InP surface emitting injection lasers," Jpn. J. Appl. Phys. D: Appl. Phys. **18**, 2329 (1979).

120. J. L. Jewell, S. L. McCall, A. Scherer, H. H. Houh, N. A. Whitaker, A. C. Gossard, and J. H. English, "Transverse modes, waveguide dispersion and 30-ps recovery in submicron GaAs/AlAs microresonators," Appl. Phys. Lett. **55**, 22 (1989).

121. A. Chailervanitkul, S. Kinoshita, and K. Iga, "GaInAsP-InP surface emitting laser (λ = 1.2 μm, 77 K) with hetromultilayer bragg reflector " Electron Lett. **21**, 303 (1985).

122. S. A. Chalmers, K. L. Lear, and K. P. Killeen, "Low resistance wavelength-reproducible p-type (AlGa)As distributed Bragg reflectors grown by molecular beam epitaxy," Appl. Phys. Lett. **62**, 1585 (1993).

123. Y.H. Lee, J.L. Jewell, A. Scherer, and S. L. McCall, "Room-temperature continuous-wave vertical-cavity single-quantum-well microlaser diodes," Electron. Lett. **25**, 1377 (1989).

124. J. L. Jewell, A. Scherer, S. L. McCall, and Y. H. Lee, "Low-threshold electrically pumped vertical-cavity surface-emitting microlasers," Elec-tron. Lett. **25**, 1123 (1989).

125. R. S. Geels, S. W. Corzine, J. W. Scott, and D. B. Young, "Low threshold planarized vertical-cavity surface-emitting lasers," IEEE Photon. Technol. Lett. **2**, 234 (1990).

126. R. S. Geels, and L. A. Coldren, "Submilliamp threshold vertical-cavity laser diodes," Appl. Phys. Lett. **57**, 1605 (1990).

127. R. L. Thronton, and L. Hesselink, "Near-Field Laser And Detector Apparatus And Method," U. S. Patent, ed. (2003).